BALLOON-BORNE INVESTIGATION OF COSMIC GAMMA RAYS AT ENERGIES ABOVE 200 MeV

A thesis submitted

by

KEVIN BENNETT

for the degree of

DOCTOR OF PHILOSOPHY

in the University of London

Department of Physics

Imperial College of Science and Technology

London S.W.7

March 1973

ABSTRACT

Gamma-rays, photons of energy $\geq$ 50 MeV, are copious secondary products of high energy cosmic ray interactions. As they travel undeflected from their source region they provide an important tool for probing the galaxy and metagalaxy.

The possible gamma-ray production mechanisms are discussed and it is seen that they can be differentiated by means of the observed gamma-ray spectrum. Several experiments have been carried out to detect galactic sources of radiation at ~100 MeV and their results conflict. An experiment comprising two balloon borne detectors was carried out in an attempt to resolve this argument, the results of which indicate a gamma-ray flux of energy greater than 200 MeV in the galactic centre region.

The flux, interpreted as a line intensity, is discussed in comparison with other observations. The decay of π^0 mesons produced in the interactions between cosmic ray nuclei and interstellar gas is deduced to be the likely gamma-ray source mechanism.

ACKNOWLEDGEMENTS

I am grateful to Professor H. Elliot for the opportunity of studying in his group and I would like to thank Dr. G. K. Rochester for his keen interest and guidance throughout this project.

My sincere thanks go to Dr. R. K. Sood, Dr. P. Penengo and Dr. T. R. Sanderson for their invaluable contributions to the project.

I am indebted to Professor C. J. Ball and his staff at the University of Zambia for providing ground facilities and the students of the University for their help with the balloon launches.

I should like to thank Peter Clayton for his comments and Clare Clayton for typing this thesis so quickly.

I am grateful to the Science Research Council for a Post Graduate Studentship.

Finally, I thank my wife, Stephanie, for her unfailing support and encouragement, to whom I dedicate this thesis.

CONTENTS

Abstract ii

Acknowledgements iii

CHAPTER I INTRODUCTION

1.1 Introduction 1

1.2 Gamma-Ray Production Mechanisms 2

1.2.1 Gamma-Rays from Nuclear Interactions 3

1.2.1.1 π^0 Meson Decay 3

1.2.1.2 Matter - Antimatter Annihilation . . . 7

1.2.2 Gamma-Rays from Electromagnetic Interactions 8

1.2.2.1 Bremsstrahlung 8

1.2.2.2 The Inverse Compton Effect 10

1.2.2.3 Magnetic Bremsstrahlung, Synchrotron Gamma-Rays 11

1.2.2.4 The Combined Inverse Compton and Synchrotron Effect 13

1.2.3 Photon Pion Production 13

1.3 Gamma-Ray Absorption 14

1.4 Gamma-Ray Astronomy 16

CHAPTER II THE GAMMA-RAY DETECTOR

2.1 Introduction and Design Requirements 21

2.2 Coincidence Telescope and Logic Elements . . . 24

2.2.1 The Scintillator Coincidence Elements 24

2.2.2 The Cerenkov Element 24

2.2.3 The Anticoincidence Detector 28

2.3 Lead Converter 30

2.4 The Spark Chamber 30
2.4.1 Spatial and Angular Resolution 37
2.4.2 Spark Chamber Efficiency 38
2.5 The Cerenkov Energy Calorimeter 41
2.6 The Aspect Sensors 48
2.6.1 Detector Tracking 48
2.6.2 The Magnetometer 49
2.6.3 Event Timing 49
2.6.4 Solar Sensor 50
2.7 Electronics and On-Board Data Handling 50
2.8 Environmental Stability of the Detector 53
2.9 Contamination of the Gamma-Ray Event Channel by Spurious Events 53

CHAPTER III GROUND EQUIPMENT AND BALLOON FLIGHTS

3.1 Ground Equipment 56
3.2 The Balloon Flights 56
3.3 Preliminary Data Analysis 58
3.3.1 Charged Particle Events 58
3.3.2 Gamma-Ray Events 63
3.4 Detailed Gamma-Ray Event Analysis 68
3.5 In Flight Detector Calibration and Orientation Accuracy 69
3.6 Atmospheric Gamma-Rays 72
3.6.1 Comparison of Gamma-Ray Rates Observed in Flight 1 and Flight 2 72
3.6.2 The Secondary Gamma-Ray Energy Spectrum 75
3.6.3 Comparison of the Measured Spectrum with Other Results 77

CHAPTER IV SEARCH FOR GAMMA-RAY SOURCES

4.1 Determination of the Gamma-Ray Arrival Direction 84

4.2 Angular Resolution of the Detector 87

4.3 Detector Sensitivity to Point Sources 94

4.4 Point Sources 101

4.5 Galactic Line Emission 103

4.5.1 Treatment of Data 103

4.5.2 Galactic Line Source Intensity 112

4.5.3 Flight 2 Results 114

CHAPTER V DISCUSSION 117

References 129

CHAPTER I

INTRODUCTION

1.1 Introduction

It is difficult to overstate the importance of successful exploration and measurement of cosmic gamma-rays in the unravelling of the complex, interwoven questions of Cosmic-Ray Physics, Cosmology and Astronomy.

Morrison (1958) was one of the first to recognize the worth of gamma-ray astronomy as a means of investigating primary protons, possibly in their source regions, as gamma-rays are the copious secondary products of their interactions with matter.

Protons, unlike electrons, do not radiate owing to their relatively large mass and they are scattered by the tenuous fields in the universe. However, secondary gamma-rays result from proton interactions and as they retain their source information and initial momenta, they provide direct evidence of the presence of protons.

Whether the cosmic-rays originate in the galaxy or are a Universal phenomenon is a dilemma which lends itself to resolution by studying the gamma radiation produced in interactions with the dilute diffuse galactic and intergalactic gas (Ginzburg, 1972). The distribution of the target gas (neutral hydrogen) in the galaxy has been well studied (e.g., Oort, Kerr and Westerhout, 1958, Garmire and Kraushaar, 1965) and it is such that in a uniform cosmic-ray intensity, the resulting gamma-ray flux will appear anisotropic at the earth, the intensity being greatest along the galactic disc (Pollack and Fazio, 1963). The first significant measurement of a primary gamma-ray flux was announced in 1968 by

Clark, Garmire and Kraushaar, who observed the galactic anisotropy of the form predicted.

Cosmological models which involve either continuous production of matter ('steady state' cosmology) or the instantaneous creation of matter ('big-bang' cosmology) have found it difficult to account for the production of anti-matter. By studying the annhilation gamma-ray fluxes emanating from regions containing matter and anti-matter in close proximity direct tests of hypotheses are provided. Furthermore, gamma-radiation provides a means of probing the Universe to large red shifts thereby giving clues to its evolution (Stecker, 1971).

The significance of gamma-ray observations is matched by the degree of difficulty in detecting the photons. At sea level the atmosphere obscures the primary photon flux as the interaction length of 100 MeV gamma-rays is about 40 gm cm^{-2}, so satellites and high altitude balloons carry detectors above the atmospheric screen. Until recently the size of payloads has been strictly limited and have therefore been rendered rather insensitive to the gamma-radiation, whose flux amounts to only 1/1000 that of the nucleonic component of the cosmic ray beam. However, during the last decade, gamma-ray astronomy techniques have been developed to overcome these limitations and new and exciting results have begun to appear.

1.2 Gamma-Ray Production Mechanisms

The processes which lead to the production of cosmic gamma-rays have been reviewed by many authors: Fazio (1967), Garmire and Kraushaar (1965), Ginzburg and Syrovatskii (1964), Boldt (1969) and Stecker (1971). Those mechanisms giving rise to gamma-radiation of energy greater than 50 MeV are discussed below

paying particular attention to the characteristic gamma-ray spectrum of each. It is also shown how measured fluxes may be interpreted in terms of the present known astrophysical parameters.

1.2.1. Gamma-Rays from Nuclear Interactions

1.2.1.1 π^0 Meson Decay

In interstellar space, the cosmic-ray nuclei interact with the interstellar matter existing in the form of gas and dust, producing energetic mesons in the inelastic p-p collisions:

$$p + p \rightarrow p + p + a(\pi^+ + \pi^-) + b\pi^0$$

$$p + p \rightarrow p + n + \pi^+ + c(\pi^+ + \pi^-) + d\pi^0$$

Since about 90% of the cool interstellar gas exists as neutral hydrogen and the cosmic-ray flux is made up of about 90% protons, the p-p interaction dominates. However, the interactions involving alpha-particles are not inconsiderable, since they comprise about 40% of the nucleonic matter in the cosmic-ray beam and interstellar matter.

The charged mesons decay into electrons or positrons in $\sim 10^{-6}$ seconds.

$$\pi^{\pm} \rightarrow \mu^{\pm} + \nu_{\mu}$$
$$\hookrightarrow e^{\pm} + \nu_e + \nu_{\mu}$$

The electrons subsequently lose energy in electromagnetic interactions until eventually leaking from the galaxy or annihilating with their anti-particles to produce two low energy gammas,

$$e^+ + e^- \rightarrow \gamma + \gamma$$

This interaction takes place predominantly near rest since the cross-section is small at high c.m.s. energies so the resulting gamma-rays have a narrow energy spectrum which peaks sharply near 0.5 MeV (Stecker, 1969a).

Although this process can be neglected as a source of 50 MeV gamma-rays, the charged pions provide an important injection mechanism for energetic electrons which radiate high energy photons by the electromagnetic interactions discussed later.

The threshold proton energy for meson production is 280 MeV, so below ~1 GeV, single meson production dominates, but at higher energies, pions are produced with a multiplicity which increases as $\sim E_p^{\frac{1}{4}}$ and the interaction cross-section is about 27 mb.

Gamma-rays are directly produced in the decay of a π^o meson, which has a lifetime in the rest frame of $\sim 10^{-16}$ sec, resulting in equal sharing of the rest mass energy.

$$\pi^o \longrightarrow \gamma + \gamma$$

In the lab. frame, the gamma-ray energies have a spread in values ranging from $(1 - \beta_\pi)\frac{E_\pi}{2}$ to $(1 + \beta_\pi)\frac{E_\pi}{2}$, so that the distribution of energies is symmetrical about 67.5 MeV on a log-log plot (67.5 MeV is half the π^o rest mass energy).

The rate at which pions of energy E_π in the energy interval dE_π are produced in a region containing n hydrogen atoms per c.c. is given by

$$q_\pi(E_\pi)dE_\pi = dE_\pi n\sigma \int_{E_\pi}^{\infty} m_\pi(E,E_\pi)I_p(E)dE \qquad cm^{-3}\ sec^{-1}\ str.^{-1}$$

$m_\pi(E,E_\pi)dE_\pi$ is the mean number of pions in dE_π produced in a collision with a cosmic ray proton of energy E in dE, the intensity of which is described by the power law

$$I_p(E) = I_{po}\, E^{-\Gamma_p}$$

Two gammas result from the decay of the neutral meson which number about 1/3 of the total number of mesons produced, so from the kinematics of the decay,

$$q(E_\gamma) = \frac{2}{3}\int_{E_\gamma + \frac{(m_\pi c^2)^2}{4E_\gamma}}^{\infty} \frac{q_\pi(E_\pi)dE_\pi}{(E_\pi^2 - m_\pi c^2)^{\frac{1}{2}}} \qquad \text{(Stecker, 1971)}$$

The resulting gamma-ray source function has been evaluated in detail by Stecker (1971), who has included the contribution to the total gamma-ray flux from the p -α, α- p and α-α interactions. The integral production spectrum which resulted is illustrated in Figure 1.1.

At>1 GeV, it can be shown that the spectrum is described by a power law. Using the delta-function approximation (Gould and Burbidge, 1967)

$$m(E,E_\pi) \simeq K' E^{\frac{1}{4}} \delta(E_\pi - K'' E^{\frac{3}{4}})$$

and integrating the pion source function, we have

$$q_\pi(E_\pi)dE_\pi \propto n\sigma I_{po} E^{-4/3(\Gamma_p - \frac{1}{2})} dE_\pi$$

putting $\Gamma_\pi = 4(\Gamma_p - \frac{1}{2})/3$

$$q_\gamma(E_\gamma)dE_\gamma \simeq \frac{2}{3} \cdot \frac{q_\pi(E_\gamma)dE_\gamma}{\Gamma_\pi} \qquad (cm^3 sec\ str)^{-1}$$

The total intensity of gamma-rays produced by nuclear interactions along a path length L can be expressed by

$$I_\gamma(>E_\gamma) = N(L).f(>E_\gamma) S(I_p, \sigma, m_\pi) \qquad (cm^2 sec\ str)^{-1}$$

where N(L) is the line of sight density of target nuclei

$f(>E_\gamma)$ is the fraction of gamma-rays produced whose energy exceeds E and S is the total production rate of gamma-rays depending upon the cosmic ray spectrum I_p, the interaction cross-section, and the pion multiplicity m_π.

Several authors have evaluated the quantities S and $f(>E_\gamma)$, the latter describing the spectral form of the gamma-ray intensity distribution. Table 1.1 lists the results of these workers, a notable discrepancy arising between these and that of Cavallo and Gould, which imply a production rate of at least a factor of two greater than any of the other estimates.

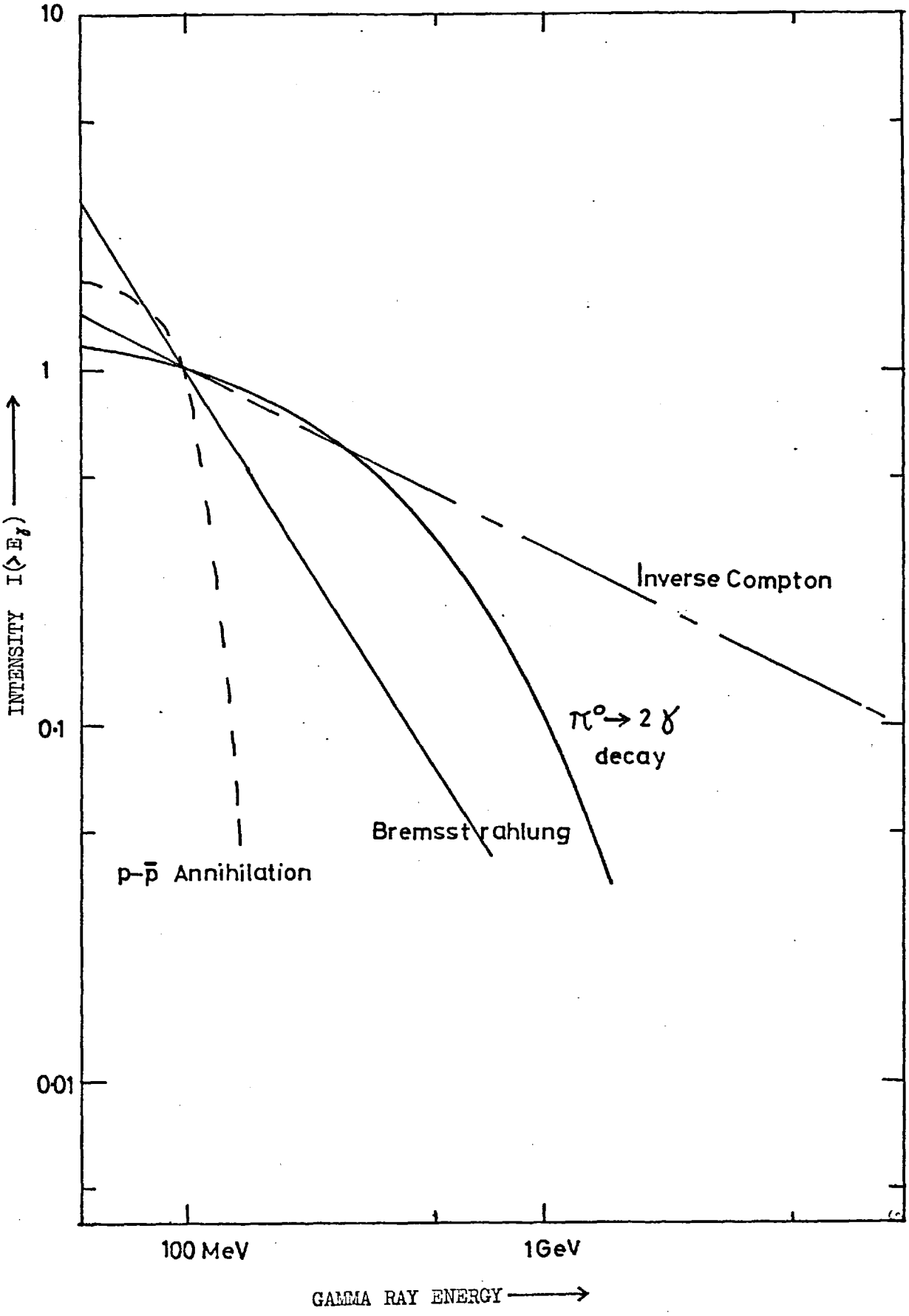


Figure 1.1 Gamma-ray spectra from bremsstrahlung, inverse Compton, $p - \bar{p}$ annihilation and π^o decay production mechanisms, curves normalized to 100 MeV.

Reference	f >100 MeV (approx.)	f >200 MeV	Assumed Proton Spectrum	Gamma-Ray Production Rate, S, $(cm^3 sec\ str)^{-1}$ $\times 10^{-26}$
Pollack & Fazio (1963)	0.7	-	$E^{-2.2}$	0.97
Ginzburg & Syrovatskii (1964)	0.7	-	$E_p^{-2.6}$	0.8
Stecker (1971)	0.73	0.54	graphical form	1.3
Cavallo & Gould (1971)	0.7	0.48	as for Stecker	1.8

TABLE 1.1

1.2.1.2 Matter - Antimatter Annihilation

Protons and antiprotons can interact in an inelastic collision in two ways, either a strong meson producing interaction occurs, or, particularly when the relative velocity of the protons is small, they can annihilate.

i.e. $p + \bar{p} \longrightarrow p + \bar{p} + \pi^0$ or, $p + n + \pi^+$

or $p + \bar{p} \longrightarrow a\pi^+ + b\pi^- + c\pi^0$

Gamma-rays result from the decay of the π^0 meson in contrast to the $e^+ - e^-$ annihilation in which the gamma-rays are directly produced.

Stecker (1971) has dealt at length with the production of annihilation gamma-rays in the metagalaxy considering that rest-

gas interacting with rest-gas would provide the primary source since the annihilation cross-section is greatest at low c.m.s. velocities. Two points arise directly from this assumption, firstly, the resultant gamma-ray spectrum is not likely to be very different from the decay spectrum of slow pions, being narrow and peaking sharply at 67.5 MeV/c^2 and, secondly, the process is unlikely to occur in the galaxy. Stecker has taken into consideration Coulomb interaction between the antiparticles in deriving a spectrum and the modified cross-section σ_A gives the approximate production rate

$$q_A(E_\gamma) \simeq n_p\, n_{\bar{p}}\, c\, \sigma_A\, m_\gamma\, f(E_\gamma) \left(\frac{2mc^2}{\pi kT}\right)^{\frac{1}{2}} \quad cm^{-3}sec^{-1}$$

n_p and $n_{\bar{p}}$ are the densities of matter and anti-matter in gaseous form at 10^6 °K temperature, σ_A is the cross-section and m_γ the gamma-ray multiplicity

$$q_A(E_\gamma) \simeq n_p\, n_{\bar{p}} \times 4 \times 10^{-14} \quad (cm^3 sec\ str)^{-1} \text{(Stecker, 1971)}$$

The integral gamma-ray spectrum $f(E_\gamma)$ shown in Figure 1.1 is that of Stecker, which is in good agreement with that of Frye and Smith (1966).

The integral gamma-ray flux due to annihilation is given by

$$I_A(> 50\ MeV) = 4 \times 10^{-14}\, R \int n_p(r)\, n_p(r)\, dr \quad (cm^2\ sec\ str)^{-1}$$

when $R = \frac{n_{\bar{p}}}{n_p}$.

1.2.2 Gamma-Rays from Electromagnetic Interactions

1.2.2.1 Bremsstrahlung

Electrons lose energy from their collisions with nuclear

matter by the bremsstrahlung process and the differential cross-section for an electron of energy E to emit a bremsstrahlung photon of energy E_γ in dE_γ in the field of a nucleus is

$$\sigma_B(E,E_\gamma)dE_\gamma \approx \left(\frac{m}{X_o}\right)\frac{dE_\gamma}{E_\gamma} \text{ cm}^2, \qquad E > 137\, m_e c^2 Z^{1/3}$$

(Fazio, 1967), where m is the mass of the target atom in gm, Z is atomic number and X_o is the radiation length of target gas.

For interstellar gas, the radiation length is about 55 gm cm^{-2} and as the intergalactic gas composition is assumed similar the same value obtains.

The production rate of gamma-rays is dependent upon the electron spectrum as well as the distribution and density of matter as follows:

$$q_\gamma = \int_{E_\gamma}^{\infty} n\,\sigma_B\,(E,E_\gamma)\; I_e(E)\; dE \qquad (\text{cm}^3 \text{sec str})^{-1}$$

where n is the density of the target atoms

Thus $$q_\gamma = \frac{n\,m}{X_o}\int_{E_\gamma}^{\infty}\frac{dE_\gamma I_e(E)dE}{E_\gamma}$$

The electron differential energy spectrum is of the form

$$I_e(E) = K_e E^{-\Gamma_e} \qquad (\text{cm}^2 \text{sec str GeV})^{-1}$$

$$q_\gamma = \frac{n(r)\,m}{X_o}\int_{E_\gamma}^{\infty}\frac{dE_\gamma}{E_\gamma}\; I_e(E)\; dE$$

$$= \frac{n(r)\,m\,K_e}{X_o\,(\Gamma_e - 1)}\; E_\gamma^{-\Gamma_e}\, dE_\gamma \qquad (\text{cm}^3 \text{sec str})^{-1}$$

Therefore the bremsstrahlung flux is a function of the line-of-sight density of matter in the electron beam where the spectral exponent is that of the cosmic-ray electron spectrum.

Assuming that the electron energy spectrum is the same for all r,

$$q_\gamma(>E_\gamma) = n(r) \times 3 \times 10^{-26} \times K_e E_\gamma^{-(\Gamma_e - 1)} \frac{}{(\Gamma_e + 1)^2} \quad (cm^3 sec\ str)^{-1}$$

1.2.2.2 The Inverse Compton Effect

When a high energy electron interacts with a low energy photon, e.g., a starlight photon, then in the electron's rest frame, the low energy photon appears as a high energy gamma-ray. The normal Compton effect in the electron's frame transforms to the Inverse Compton effect in the laboratory or cosmic frame of reference.

The cross-section for the process is most accurately given by the Klein Nishina formula,

$$\sigma_c = \sigma_T \left(1 - \frac{2\gamma_e \varepsilon}{m_e c^2}\right) \quad cm^2 \quad (\gamma\varepsilon > m c^2)$$

where $\sigma_T = \frac{8\pi r_e^2}{3}$ (the Thompson cross-section),

γ_e is the Lorentz factor for the electron and ε is the photon's initial energy (~few eV).

For the scattered photon of energy below several GeV the cross-section is not significantly different from the Thompson cross-section. As has been described by Felton and Morrison (1963 and 1966) the scattered photon energy is related to the incident electron's energy through its Lorentz factor γ_e.

$$E_\gamma \simeq \bar{\varepsilon} \gamma_e^2$$

$\bar{\varepsilon}$ is the mean energy of the photon field.

The gamma-ray production rate is therefore

$$q_{\gamma c}(E_\gamma) = \frac{\rho \sigma_T}{\bar{\varepsilon}} I_e(E)\, dE \quad (cm^3 sec\ str)^{-1}$$

where ρ is the photon energy density

or the integral gamma flux is given by

$$q_{\gamma c}(>E_\gamma) = \frac{\rho \sigma_T}{\bar{\varepsilon}} \int_{mc^2\sqrt{\frac{E_\gamma}{\bar{\varepsilon}}}}^{\infty} I_e(E)\,dE$$

Now $I_e(E) = K_e E^{-\Gamma_e}$

thus $q_{\gamma c}(>E_\gamma) = K_e \frac{\rho \sigma_T}{\bar{\varepsilon}} \left[\frac{E^{-\Gamma_e + 1}}{-(\Gamma_e + 1)}\right]_{mc^2\sqrt{\frac{E_\gamma}{\bar{\varepsilon}}}}^{\infty} = \frac{K_e \rho \sigma_T (mc^2)^{(1-\Gamma_e)} E^{-(\Gamma_e - 1)/2}}{(\Gamma_e - 1)\ \bar{\varepsilon}^{-(\Gamma_e - 3)/2}}$ $(cm^3 sec\ str)^{-1}$

$\sigma_T = 6.651 \times 10^{-25}\ cm^2$

The inverse Compton gamma-ray spectrum is therefore related to the electron spectrum by $\Gamma_{\gamma c} = \frac{1}{2}(\Gamma_e + 1)$ so the inverse Compton exponent is half that of the bremsstrahlung spectrum, given the same electron energy spectrum.

1.2.2.3 Synchrotron Radiation

Evidence that the synchrotron process is taking place is given by the non-thermal radio emission of our own and radio galaxies. This important electron energy loss process in tenuous magnetic fields is seen in the Crab and in the galaxy Virgo A to generate photons into the visible. However, no measurable gamma-ray flux is expected from this process alone since for an electron of energy E eV in a field H gauss, the frequency spectrum of synchrotron gamma-rays peaks at

$$\nu_{max} = 4.6 \times 10^{-6}\ H\ (E)^2 \qquad Hz$$

and neither electrons of sufficient intensity nor fields of sufficient strength exist to satisfy this relation for quanta ~few MeV (10^{22} Hz).

The rate of loss of energy of an electron of energy E by the synchrotron process

$$-\left(\frac{dE}{dt}\right)_s \simeq \sigma_T\, c\rho_H \left(\frac{E}{m_e c^2}\right)^2 \qquad \text{eV sec}^{-1}$$

where $\rho_H = \frac{H^2}{8\pi}$, the magnetic field energy density and σ_T is the Thompson cross-section.

This expression is analagous to the rate of energy loss of electrons by the Inverse Compton effect where,

$$-\left(\frac{dE}{dt}\right)_c \simeq \sigma_T c\rho \left(\frac{E}{m_e c^2}\right)^2 \qquad \text{eV sec}^{-1}$$

where $\sigma_T c\rho/\varepsilon$ is the rate of collisions between the electron and the photon field and $\varepsilon(E/m_e c^2)^2$, or $\gamma_e^2 \varepsilon$, is the energy lost per collision.

The ratio of the energy losses is about unity, since fields of the order 10^{-5} gauss occur in interstellar space whilst the photon energy density of the 2.7 ^{o}K Universal microwave radiation is about 1 eV / cc

$$\frac{\left(\frac{dE}{dt}\right)_c}{\left(\frac{dE}{dt}\right)_s} \approx 1$$

More important is the fact that the spectral exponents for the processes are the same for the same electron spectrum, whilst the product photons are widely separated on the energy scale. The possibility is therefore afforded of checking the electron spectral index by measuring both radio and X-ray radiation from the same electrons.

At present the high energy electron data indicate that the spectral exponent $\Gamma_e \simeq 2.6$ at energies greater than 5 GeV.

Solar modulation complicates the interpretation of the spectrum at lower energies. The radio spectral index α is related to Γ_e by

$$2\alpha + 1 = \Gamma_e$$

and the galactic radio measurements give $\alpha \hat{=} 0.8$ which is in agreement with $\Gamma_e = 2.6$ (Ginzburg and Syrovatkii, 1964) though the electron injection spectrum is thought to be of the form E^{-2}, the steepening induced by the various loss mechanisms - leakage, ionization, Compton etc., in the galaxy (Felton and Morrison, 1966).

1.2.2.4 The Combined Inverse Compton and Synchrotron Effect

A possible source mechanism was proposed for discrete gamma-ray sources by Gould (1965) whose model supposes that electrons which radiate energy in the radio frequency range by the synchrotron process, in the confines of a gaseous nebula, say, interact with these radio photons producing gamma-rays by inverse Compton effect. Measurement of such gamma-rays provides a simultaneous measurement of the electron density in such a way that an upper limit to the gamma-ray source strength implies a lower limit to the magnetic field. (Weekes et al. 1972)

1.2.3 Photo-Pion Production

A proton flux of $> 10^{17}$ eV would not be bound to the galaxy (Larmor radius of a 10^{18} eV proton $\simeq$ 1 kpc). When such a proton encounters a low energy photon $\sim$1 eV, then the centre of mass energy is sufficient for pion production. The produced pions have almost the same velocity as the proton and decay in flight giving photons of $\sim 10^{16}$ eV.

This important process renders the universe opaque to this high energy radiation and provides a method, of probing the universe to early epochs by investigating the high energy quanta and their spectrum.

Such a process is not restricted to intergalactic space because if cosmic-rays originate either in supernovae or the associated pulsars and if the large density of electrons is assumed to imply an even larger (non-radiating) proton flux then photo-pion gamma-rays may be observable.

1.3 Gamma-Ray Absorption

Gamma-rays are absorbed by matter by the photo-electron effect, Compton effect and pair production. In the galaxy the interstellar gas is the prime absorber and for 50 MeV gamma-rays the total mass absorption coefficient for these three processes is only $\sim 0.02\ gm^{-1}cm^2$. As the galaxy presents only a maximum depth of $\sim 0.06\ gm^{-1}cm^2$ to an intergalactic gamma-ray, attenuation of gamma-ray flux is negligible.

At very high gamma-ray energies pair production with low energy photon background is the dominant absorption mechanism,

$$\gamma + \gamma \longrightarrow e^+ + e^-$$

The threshold energy for pair production is easily estimated since when a gamma-ray of energy E_γ collides with a photon of energy E_b at an angle of θ the available energy E^* in the c.m.s. is given by

$$E^{*2} = 2 E_b E_\gamma (1 - \cos\theta)$$

For a head on collision ($\cos\theta = -1$) the gamma-ray threshold energy is

$$E_\gamma = \frac{m_e c^2}{E_b} \quad \text{eV}$$

(m_e is the electron's rest mass 0.51 MeV / c^2)

The universal photon fields exist in the optical, infra-red, micro-wave and radio regimes and Gould and Schréder (1967 a, b) have evaluated the absorption probability as a function of gamma-ray energy. Figure 1.2 shows their results, where the thresholds appear smeared out due to the spread in energies in the photon distribution and

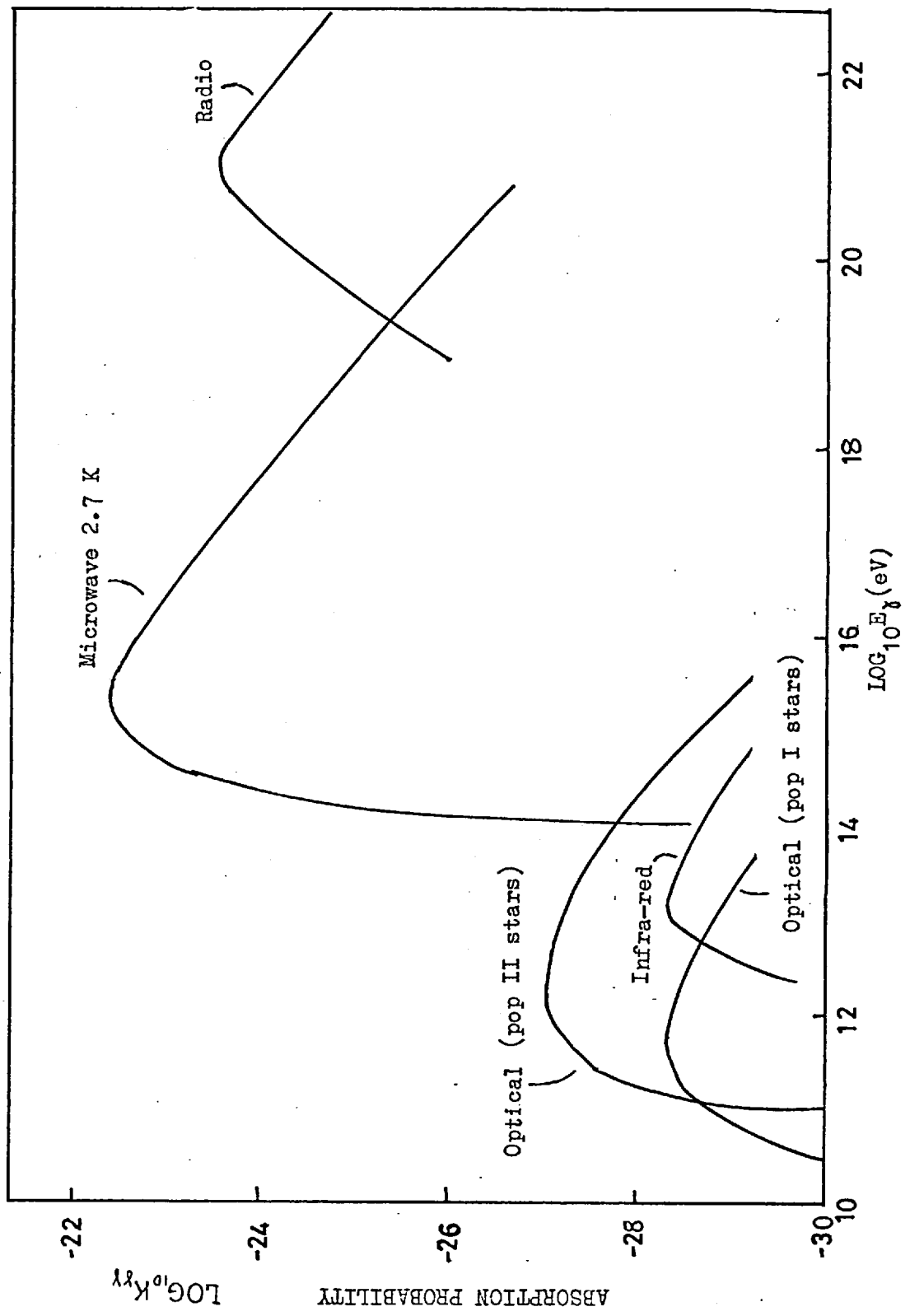


Figure 1.2 Absorption probability ($K_{\gamma\gamma}$ cm^{-1}) by $\gamma+\gamma \longrightarrow e^+ + e^-$ process for gamma-rays traversing the universal photon field.

the isotropy of the interacting photons.

1.4 Gamma-Ray Astronomy

Gamma-ray Astronomy was born in the late 1950's but the early years did not see the production of any significant results (see review by Fazio, 1967), however, during this period, the experimental techniques evolved rapidly to satisfy the need for higher detection sensitivity. The gamma-ray telescope gained such a level of sophistication (Fazio, 1970, and Kniffen, 1971), that it seemed only a matter of time before positive measurements would be made either by a successful satellite mission or by high altitude balloon flights.

In 1968, remarkable evidence for gamma-ray observation was reported by Clark, Garmire and Kraushaar from a gamma-ray telescope carried aboard the OSO 3 solar observatory satellite. The detector consisted of a complex sandwich of scintillator-Cerenkov elements and though no solar activity was observed their evidence for galactic emission was convincing.

As the angular resolution of the telescope was limited to its $\pm$ 15° opening angle, they divided the sky into 15° x 15° areas. When the detector axis was in the galactic latitude interval $-15^{\circ} < b^{II} < 15^{\circ}$, the count rate exceeded the overall sky average by 10σ, and the rate in the region of the sky $|b^{II}| > 15^{\circ}$ by 19σ (Clark, 1971).

Sood (1969), using a balloon borne scintillator-Cerenkov detector, similarly intended to look for solar emission, observed an enhancement in the gamma-ray counting rate as the galactic equator passed overhead. The opening angle of Sood's detectors was $\pm$ 15° so, like Clark, he was unable to determine any structure in the emitting region and thereby deduce whether

the increase arose from point sources or narrow line emission.

Kniffen and Fichtel (1970) confirmed the existence of a galactic line source using a large area balloon borne multi-plane spark chamber detector. At 100 MeV the observed signal from a strip of width $|b^{II}| < 6^{o}$ was 4.3σ above background.

Clark, Kniffen and Sood have all pointed out that the observed intensity was theoretically difficult to account for (the OSO 3 results were later revised, reducing the flux estimates by a factor of three). Taking the observed density of interstellar hydrogen as given by the 21 cm measurements and the local cosmic ray intensity, the estimated line intensity from π^{o} decay gamma-rays fell short by a factor of three (Stecker, 1969b). Alternative production mechanisms involving electromagnetic interactions invoked to explain the observed flux predicted line emission at low energies, i.e., in X-ray region (O'Connell and Verma, 1970). These explanations were given weight when Cooke, Griffiths and Pounds (1969) observed an anisotropic flux of ~10 KeV X-rays, an excess being along the galactic equator. However, the results of two balloon flights carried out in Australia to look at 50 MeV gamma-rays by Frye et al. (1969), using a photographic spark chamber system, did not confirm the evidence of the band source of gamma-rays in the Sagittarius region of the galaxy. In fact, the upper limit set by Frye was nearly an order of magnitude lower than Clark's original estimate of the intensity, and the lower detector threshold of Frye emphasized this discrepancy (Table 1.2).

Frye did, however, claim to have observed emission from a region of sky of proportions comparable with his detector angular resolution during both flights. He concluded that the excess counts were due to a point source of intensity $3 \pm 1 \times 10^{-5}$ cm^{-2}sec^{-1}.

Region of Galaxy Investigated	Reference	Energy Threshold of Detector MeV	Line Intensity $(cm^2 \text{ sec rad})^{-1}$	Width of Emitting Region
$-30^\circ < l'' < 45^\circ$	Clark et al. (1968) (OSO 3)	100	5×10^{-4}	$\lvert b'' \rvert < 15^\circ$
" revised	Clark et al. (1971)	100	$1.2 \pm {}^{.4}_{.5} \times 10^{-4}$	$\lvert b'' \rvert < 15^\circ$
$45^\circ < l'' < 75^\circ$	Hutchinson et al. (1970)	40	$(9 \pm 5) \times 10^{-4}$	$-10^\circ < b'' < 0^\circ$
$15^\circ < l'' < 45^\circ$	Sood (1969)	50	$(5.0 \pm 1.5) \times 10^{-4}$	$\lvert b'' \rvert < 15^\circ$
$-10^\circ < l'' < 25^\circ$	Fichtel et al. (1969)	100	$(2.2 \pm 1) \times 10^{-4}$	$\lvert b'' \rvert < 3^\circ$

TABLE 1.2

Region of Galaxy Investigated	Reference	Energy Threshold of Detector MeV	Line Intensity $(cm^2\ sec\ rad)^{-1}$	Width of Emitting Region
$-39^\circ < l^{II} < 24^\circ$	Kniffen & Fichtel (1970)	100	$(2.0 \pm 0.7) \times 10^{-4}$	$\lvert b^{II}\rvert < 6^\circ$
$60^\circ < l^{II} < 90^\circ$	Valdez et al. (1970)	100	$(3.0 \pm 1.5) \times 10^{-4}$	$-1.5^\circ < b^{II} < 4.5^\circ$
$l^{II} \simeq 350^\circ$	Cooke et al. (1969)	10 KeV	10×10^{-1}	-
$-15^\circ < l^{II} < 15^\circ$	Frye et al. (1969)	50	3.0×10^{-5} * 7.0×10^{-5} *	$\lvert b^{II}\rvert < 2.3^\circ$ $\lvert b^{II}\rvert < 15^\circ$

* 95% confidence upper limit

TABLE 1.2 (continued)

It was proposed by Ögelman (1969), that the line intensity was due to the integrated effect of many discrete emitters unresolved by the detectors of Clark and Sood. However, Kniffen and Fichtel believed that their angular resolution was sufficient to have detected this detail.

The present experiment was undertaken in an attempt to resolve the dispute regarding the existence of a line source of gamma-rays and, by measuring the energy, attempt to identify the production mechanism of any observed radiation.

CHAPTER II

THE GAMMA RAY DETECTOR

2.1 Introduction and Design Requirements

The intensity of the primary gamma radiation of energy greater than 100 MeV is such that a typical detector will register the passage of one primary photon per hour for every 100 cm^2 of detector area. A detector designed to survey the sky in order to locate and investigate the nature of sources or emission regions should, therefore, exhibit:

(a) good angular resolution.

(b) a large opening angle, so as to survey simultaneously a large area of sky

(c) a large detector area

(d) efficient rejection of noise and charged particle induced events and a means of unambiguous identification of a photon count

(e) robust construction, so as to withstand the extremes of environment that occur during a balloon flight, and a light weight

(f) high gamma-ray detection efficiency and small dead time

The sensitivity of the detector refers to the minimum source intensity discernable above the average background intensity of events (ϕ) and it may be expressed

$$I_m = S_m \cdot \sqrt{\frac{\Phi}{\epsilon} \cdot \frac{w.f}{A.T}}$$

The signal to noise ratio is specified by S_m thus I_m, the sensitivity, relates directly to the detector properties listed

above:

ε = detector efficiency

A = area of detector

T = viewing time of source

$w = \pi\eta^2$ where η is the angular resolution of the detector

f = dead time correction factor

The gamma-ray telescope which was constructed so as to optimize these performance requirements is shown schematically in Figure 2.1.

The gamma-ray telescope was of circular geometry and designed to detect photons which converted in the lead sheet into a secondary electron-positron pair which was counted by the scintillation elements B and C and the Cerenkov element D. The anticoincidence dome A vetoed all events which were characterized by the coincidence logic ABCD, and such an event was designated a charged particle cosmic ray event.

A spark chamber was positioned in the detector geometry in order to define the path of the secondary electrons and therefore infer the arrival direction of the parent gamma-ray.

The photon energy was estimated by pulse height measurements of the Cerenkov emission of the cascade shower produced by either or both of the secondary electrons in the deep lead glass element. The calibration threshold was set at 200 MeV.

Two detectors were built and flown by high altitude balloons in the early part of 1971 from Lusaka, Zambia, a detailed description of which follows.

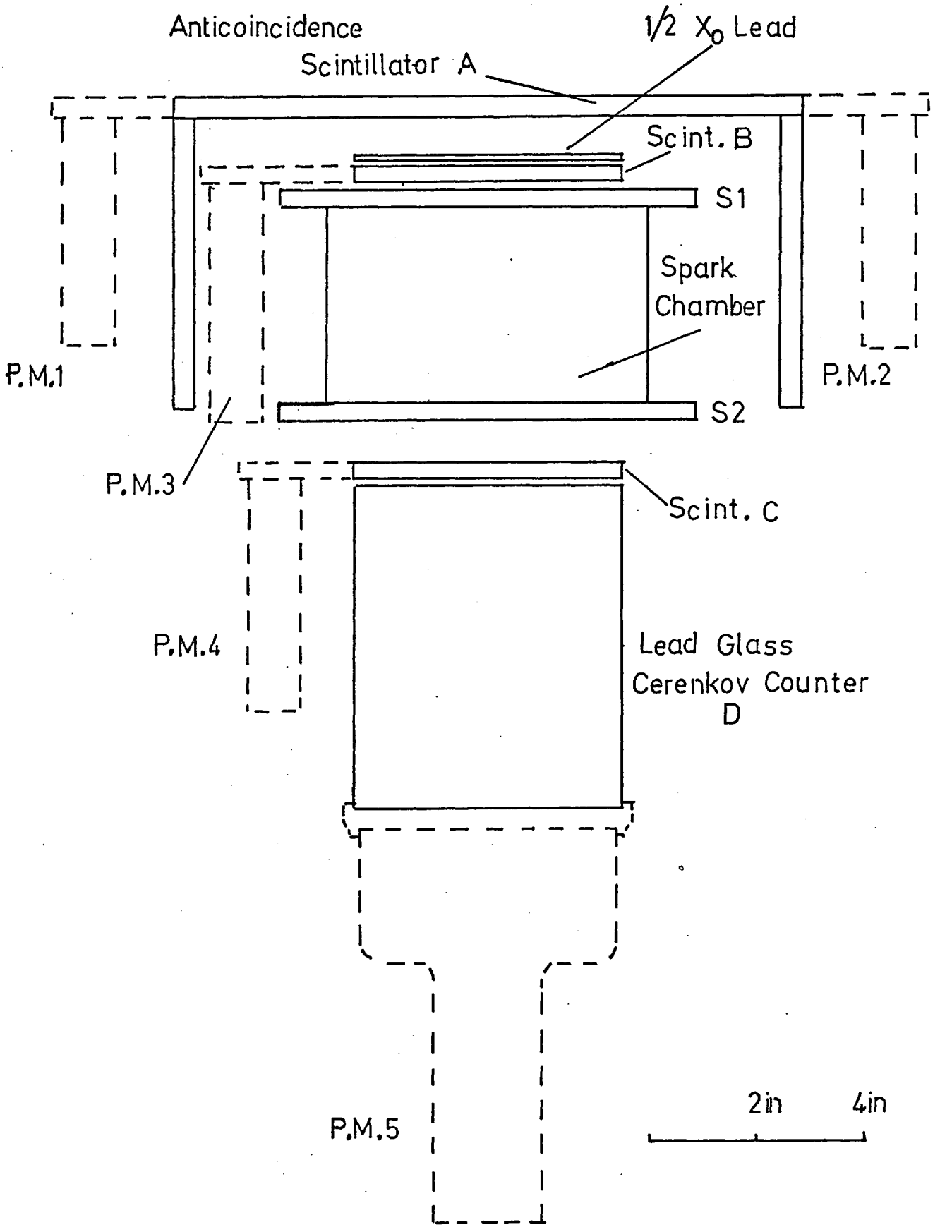


Figure 2.1 The Detector.

2.2 Coincidence Telescope and Logic Elements

2.2.1 The Scintillator Coincidence Elements

The Scintillation elements B and C were 5" diameter discs of NE102A plastic scintillator of thicknesses $\frac{1}{4}$" and $\frac{1}{8}$" respectively and each was viewed by a 1" diameter photomultiplier (PM3 and PM4, Type EMI 9524A) through perspex light guides. Ambient light was excluded by wrapping in layers of aluminium foil and black adhesive tape. A minimum ionizing particle generates about 5,000 photons in $\frac{1}{8}$" of scintillator (Crispin and Hayman, 1964, and Barnaby and Barton, 1960) so considering a quantum efficiency of 15% for the photomultiplier and a light collection efficiency of ~10%, at least 70 photo electrons were generated as a result of each charged particle traversal. A similar set up has previously been demonstrated to be better than 99.5% efficient for the detection of charged particles by Sood (1969).

2.2.2 The Cerenkov Element

The third coincidence element was provided by the lead glass Cerenkov detector which consisted of a 6" solid cylinder, 5" in diameter of Schott SF6 lead glass whose properties are listed in Table 2.1.

SCHOTT SF6 LEAD GLASS

Radiation length	1.56 cm
Density	5.19 gm/cc.
Refractive index	1.8052
E_{crit}	12.4 MeV
Electron threshold energy	110 keV
Proton threshold energy	190 MeV

TABLE 2.1

Cerenkov light is emitted when a charged particle travels through a medium at a velocity greater than the velocity of light in the medium. The light radiates forwards in a cone of half angle θ such that

$$\cos\theta = \frac{1}{\beta n}$$

where $c\beta$ = the velocity of the particle cm sec^{-1}

c = velocity of light

n = refractive index of the medium

The 5" diameter photo-tube PM5 (Type EMI 9618B) viewed the Cerenkov light generated in the glass, optical coupling being achieved using a shallow perspex light guide. The curved surfaces of the lead glass element were coated with diffuse reflecting paint in order to enhance the response to particles inclined to the axis. The upper face was painted black to absorb the upward moving light, particularly that from upward moving particles.

The output of the photo-tube PM5 was amplified through a charge amplifier, the output of which was fed into the coincidence electronics and a pulse height analyser (PHA). The pulse to the PHA was stored in a delay line until a decision was made as to whether the event was caused by a gamma-ray or a charged primary particle according to the coincidence signature. When the gamma-ray signature $\bar{A}BCD$ occurred, the amplitude of the output pulse was measured by the PHA and the digital output was recorded in a 7 bit counter.

Figure 2.2 shows a pulse height spectrum observed for sea level mu mesons which penetrated the entire length of the lead glass. An additional scintillator was temporarily positioned below the detector in coincidence with the elements

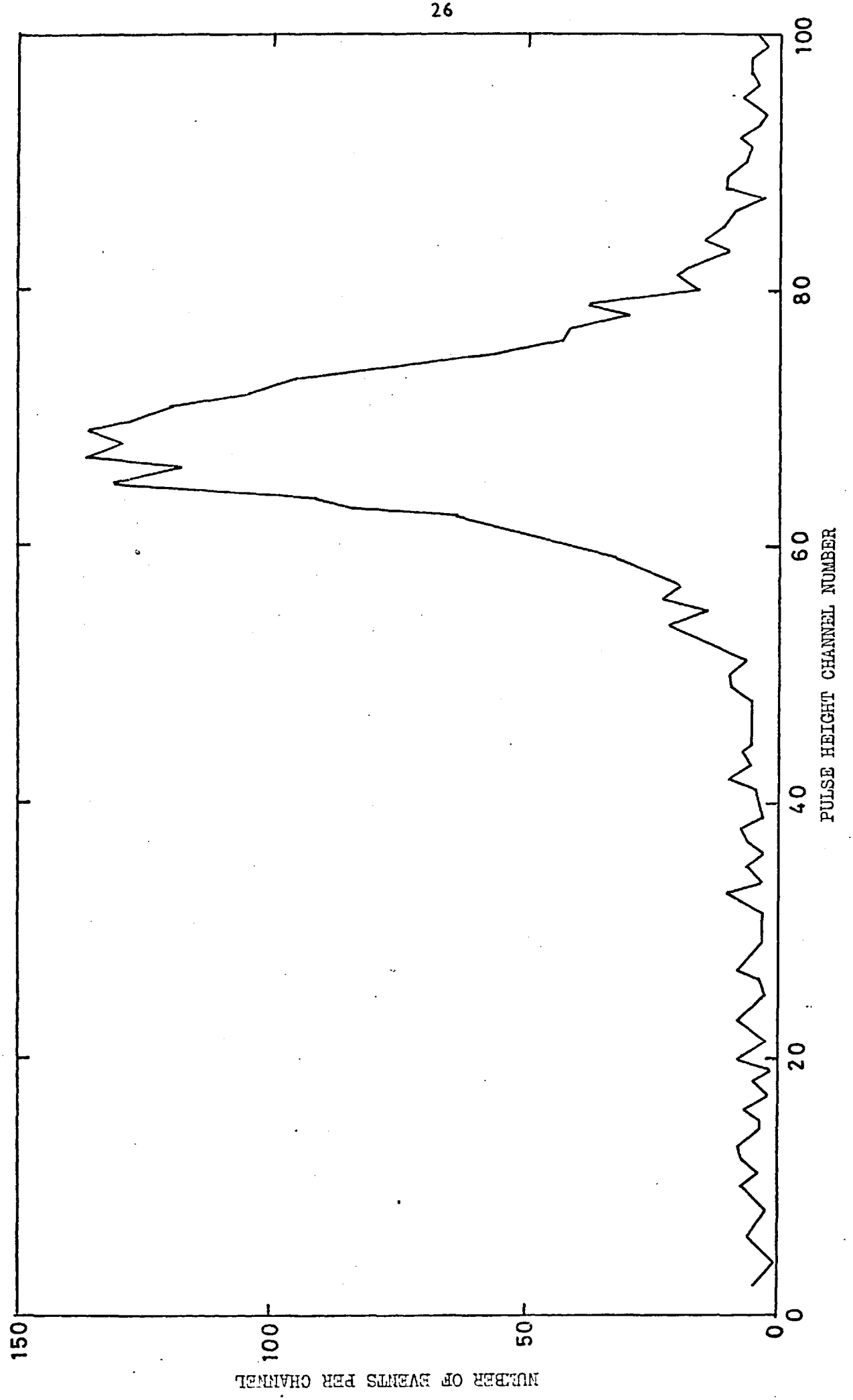


Figure 2.2 Pulse height distribution given by sea level muons which completely penetrated the lead glass counter.

B, C and D for this test. The number of photons generated by such a meson in the 6" of lead glass can be estimated, since the number of photons of frequency ν in $d\nu$ generated per centimetre of material, refractive index n is given by:

$$\frac{dN}{dl} = \frac{\pi^2 e^2}{hc^2}\left(1-\frac{1}{\beta^2 n^2}\right)\int_{\nu_1}^{\nu_2} d\nu \qquad \text{photons/cm}$$

(Zrelov, 1970)

this may be written

$$\frac{dN}{dl} \simeq 2\pi\alpha\,\frac{\lambda_2-\lambda_1}{\lambda_1\lambda_2}\left(1-\frac{1}{\beta^2 n^2}\right)$$

Noting that $\frac{d^2N}{dld\lambda} \simeq \frac{1}{\lambda^2}$, the Cerenkov light output peaked towards the blue end of the visible spectrum, but the transmission of the lead glass and of the perspex light guide fell off steeply at $\cdot 4\mu$. In addition the photomultiplier tube was only sensitive in the approximate range $\cdot 3.5\mu$ to $\cdot 6\mu$. The refractive index of the glass $n(\lambda)$ was assumed constant over the frequency range $\cdot 4$–$\cdot 6$ microns so the number of photons produced per centimetre was

$$\frac{dN}{dl} \simeq 370\left(1-\frac{1}{\beta^2 n}\right)$$

$$\frac{dN}{dl} \simeq 250 \text{ photons/cm}$$

A muon traversing the ten radiation lengths generated ~4,000 photons in this range.

The number of photo electrons produced at the photo cathode of the tube could not easily be estimated owing to the difficulty in determining the light collection efficiency of the system. However,

$$N_{pe} = 2\pi\alpha l\int_{\lambda_1}^{\lambda_2} \frac{1}{\lambda^2}\,\varepsilon_t(\lambda)\,L\,d\lambda$$

where ε_τ is the effective quantum efficiency after compounding the quantum efficiency (E_q) with the transmission properties of the glass as shown in Figure 2.3 and L is the light collection efficiency. Assuming L is independent of λ, the integration could be performed numerically, thus;

$$N_{pe} = \frac{2\pi \times l \times L}{137} \sum \langle \varepsilon_\tau(\bar{\lambda}) \rangle \frac{\Delta\lambda}{\langle \bar{\lambda} \rangle^2}$$

from which

$$Np_e \simeq L \times 530 \text{ photo electrons}$$

Although PM5 was situated directly below the glass cylinder, L may have been as low as 25% due to the combined effect of

(1) diffuse reflection at the walls

(2) large half opening angle of the Cerenkov light cone ($\sim 56^\circ$)

(3) blacking of the upper face and consequent absorption of reflected light

(4) differences in refractive indices of the materials

The narrowness of the peak for the muon pulse height distribution of Figure 2.2 provided a convenient calibration for the pulse height analyser and Cerenkov counter. This reference point was found to be extremely useful in setting up and cross calibrating the two detectors.

2.2.3 The Anticoincidence Detector

The anticoincidence element A surrounded the scintillator telescope and served to reject charged particle induced events by detecting their passage through the dome with high efficiency. The anticoincidence shield was constructed of $\frac{3}{8}$" thick scintillator (NE102A) and two 1" photomultipliers (PM1 and PM2) monitored the light output from the dome.

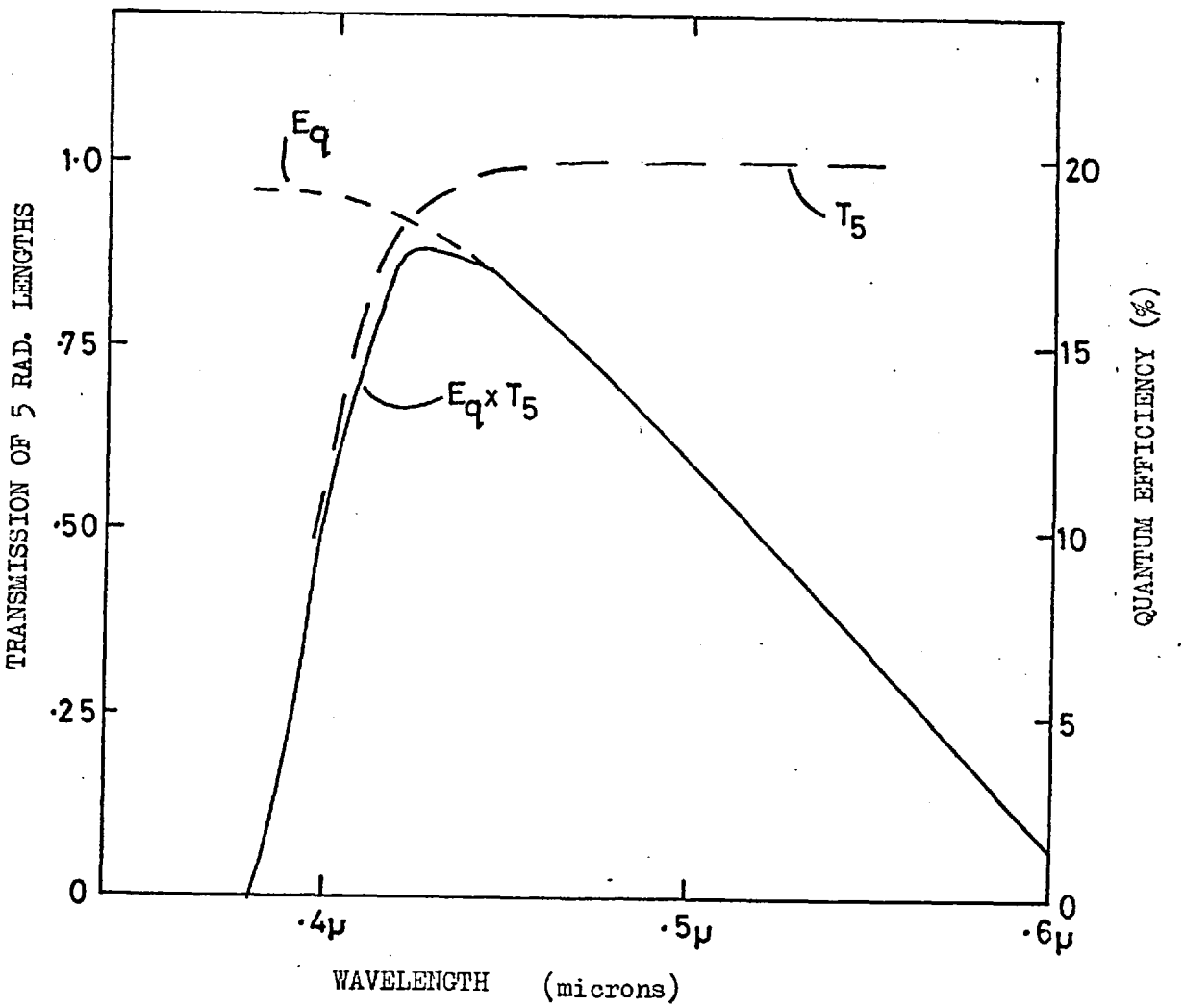


Figure 2.3 Curves showing the quantum-efficiency of the photomultiplier tube (E_q) and the transmission of the lead glass (T_5) as a function of energy.

The efficiency for rejecting primary charged particle events from the three-fold coincidence gamma-ray channel (coincidence logic $\bar{A}BCD$) was estimated by investigating the behaviour of the detector towards the flux of sea level cosmic rays. The rejection efficiency achieved exceeded 99% for each detector in the predominantly downward moving sea level flux.

2.3 Lead Converter

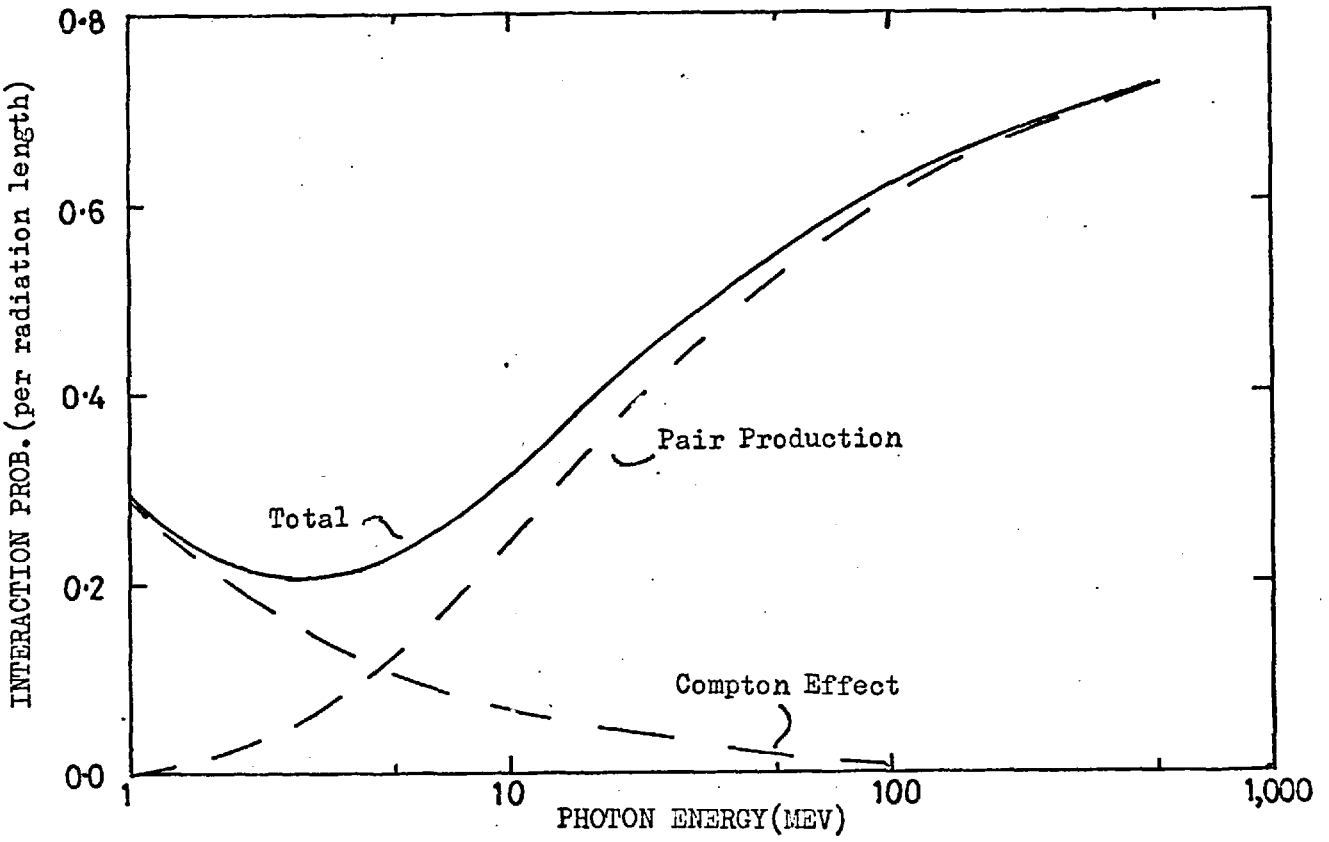
The pair production cross-section of a material is proportional to the square of its atomic number, so lead ($Z = 82$) was selected as most suitable for a gamma-ray converter, being both cheap and efficient in absorbing gamma radiation. The converter comprised a 5" disc of lead half a radiation length thick and it was seated directly above the scintillation element B.

The probability of interaction of an incident photon by the Compton effect and pair production as a function of energy is plotted in Figure 2.4a (Rossi,1952). At 100 MeV, pair production is the dominant effect and the pair production probability (conversion efficiency) for $\frac{1}{2}$ r.l. of lead is shown in Figure 2.4b.

2.4 The Spark Chamber

The spark chamber comprised a sealed unit connected by a single umbilical tube to a tap in the dural pressure tank in which it was seated. Figure 2.1 shows its position in the detector geometry.

The chamber consisted of two spark gaps separated by ~ 9 cm, which were made up of two multi-wire grids glued to opposite sides of a Tufnol former $\sim \frac{3}{8}$" thick. The wire grid



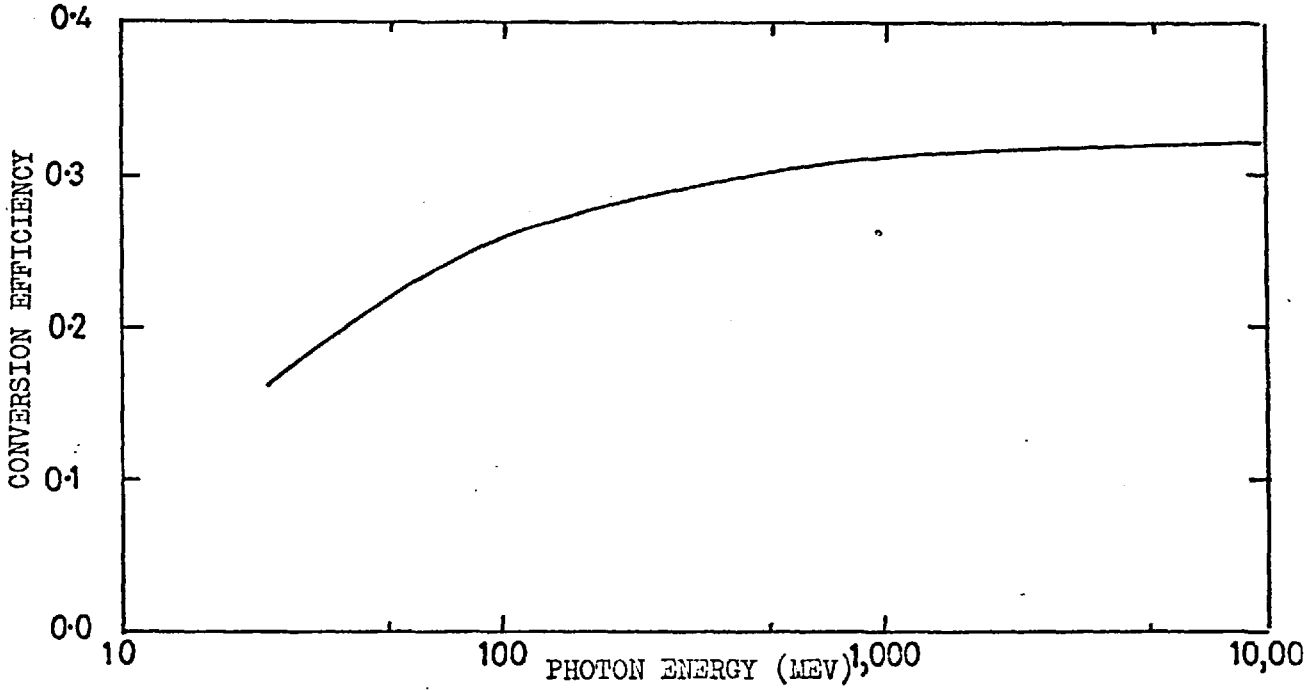


Figure 2.4a Interaction probability per radiation length of lead.

b Probability of pair production as a function of energy for $\frac{1}{2}$ r.l. of lead.

planes (manufactured by Bradford Hunt and Co. using photographic techniques) consisted of parallel copper strips 0.65 mm wide and separated by 0.65 mm, glued to a strong 'Melinex' backing sheet. To achieve even separation, and ultimately uniform electric field, between these planes, they were stretched flat and glued under tension. The active area of the spark plane was 126 mm x 126 mm. Each wire was soft-soldered to a bus-bar at one end which provided the connection to the high tension supply or ground.

The spark chamber unit was completed by gluing the spark gaps to each side of a square Tufnol box 9 cm high. Ventil ation holes were cut at each corner of the inner planes, out of the circular geometry of the telescope, so the box acted as a reservoir of gas, allowing the helium to circulate so preventing stratification.

The spark electronics and power supplies were fixed to the outside of the box and the unit was held securely in place by the dural pillars which joined the lid to the base of the pressure chamber. The spark chamber was filled with gas by evacuating the entire pressure vessel for several hours to allow the components to outgas, refilling to atmospheric pressure with helium, sealing off the spark chamber and, finally, flushing the excess helium from inside the tank. Use was made of the pressure tank's ability to withstand pressure differentials of up to an atmosphere to be experienced at balloon altitude. Rigorous tests at up to two atmospheres over-pressure were performed to ensure that leaking would not occur at altitude which would result in deformation and perhaps puncture of the spark module.

The high tension supply and triggering electronics were powered by low tension supplies outside the pressure tank. This

eliminated the need for high tension lead-throughs which reduced the likelihood of corona.

The outer planes of each spark gap were earthed and the inner planes were connected to the high tension pulsing circuits. Figure 2.5 shows the circuit diagram of the pulsing circuit. Two KN-22 Krytron tubes (coldcathode switching devices) held off high tension until triggered by a fast ~1 KV spike provided by the transformed switching output of the NS1110 avalanche transistor.

The high tension negative pulse was applied to the spark planes and the current which flowed along the ionized path of the charged particle drew charge from the 500 pf capacitors. The spark current flowed from the ground bus along the wires between which the spark occurred and out of the high voltage bus. The recovery time of the pulsing circuit was given by the product of R_r and C and was~0.1 seconds. The exact value was not critical since this time was short compared with the other dead times in the system.

The position of the wire along which the spark occurred was determined using a magnetostrictive delay technique. A length of Permendur alloy wire was laid across the spark plane near and parallel to the bus-bar and was electrically insulated from the planes by Melinex strips. The method, which was first suggested by Perez-Mendez and Pfab (1965), enabled the position of the spark to be determined by measuring the transit time of a magnetostrictive stress wave which travelled along the wire with sonic velocity.

The stress wave was produced by the change in magnetic field in the wire (the Joule effect) at the point at which the fired wire and magnetostrictive wire (M.S.W.) crossed. The resulting pulse was detected at both ends of the M.S.W. by sensing coils located inside cylindrical biasing magnets. Figure 2.6a

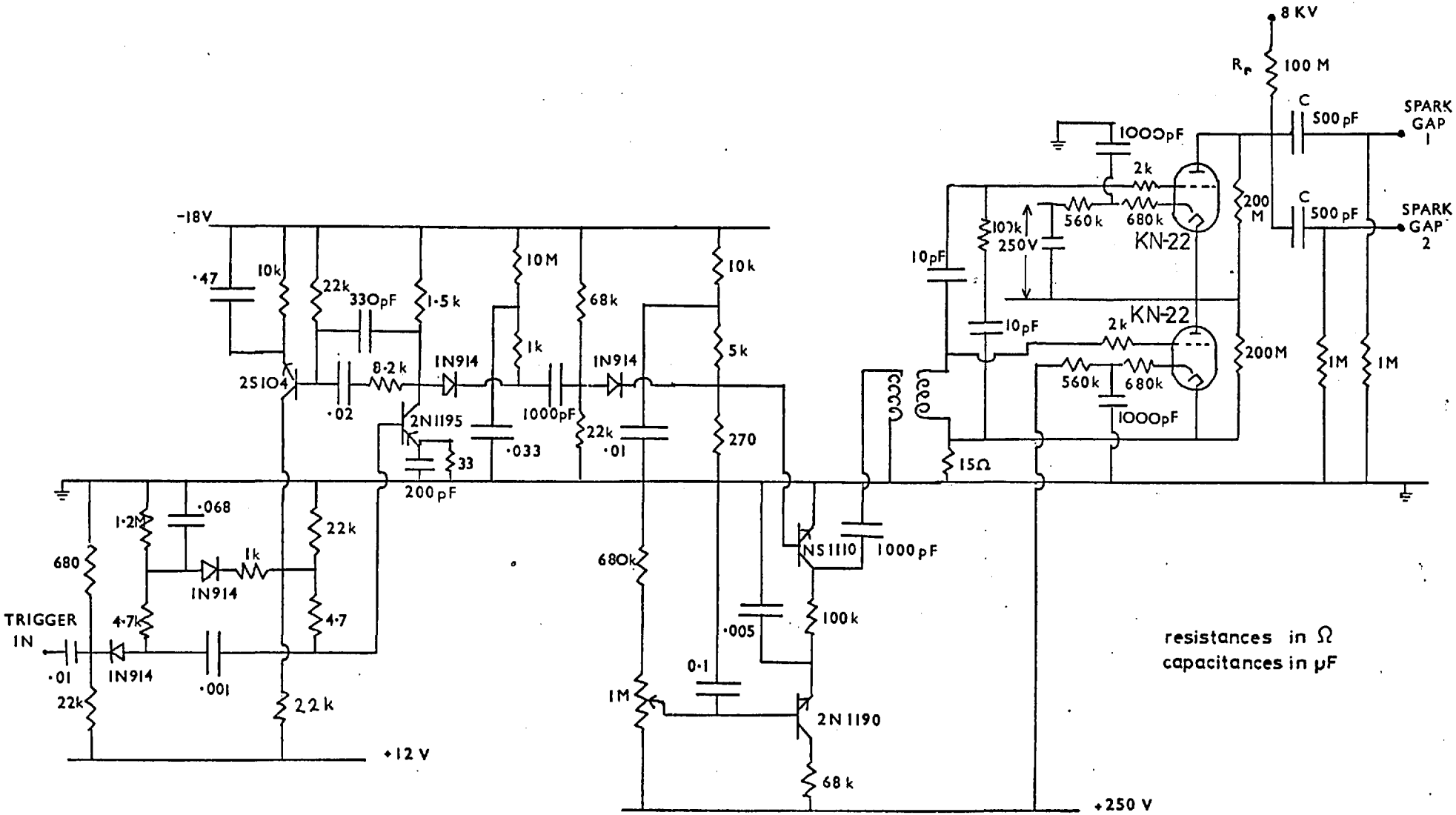


Figure 2.5 Spark chamber pulsing circuit

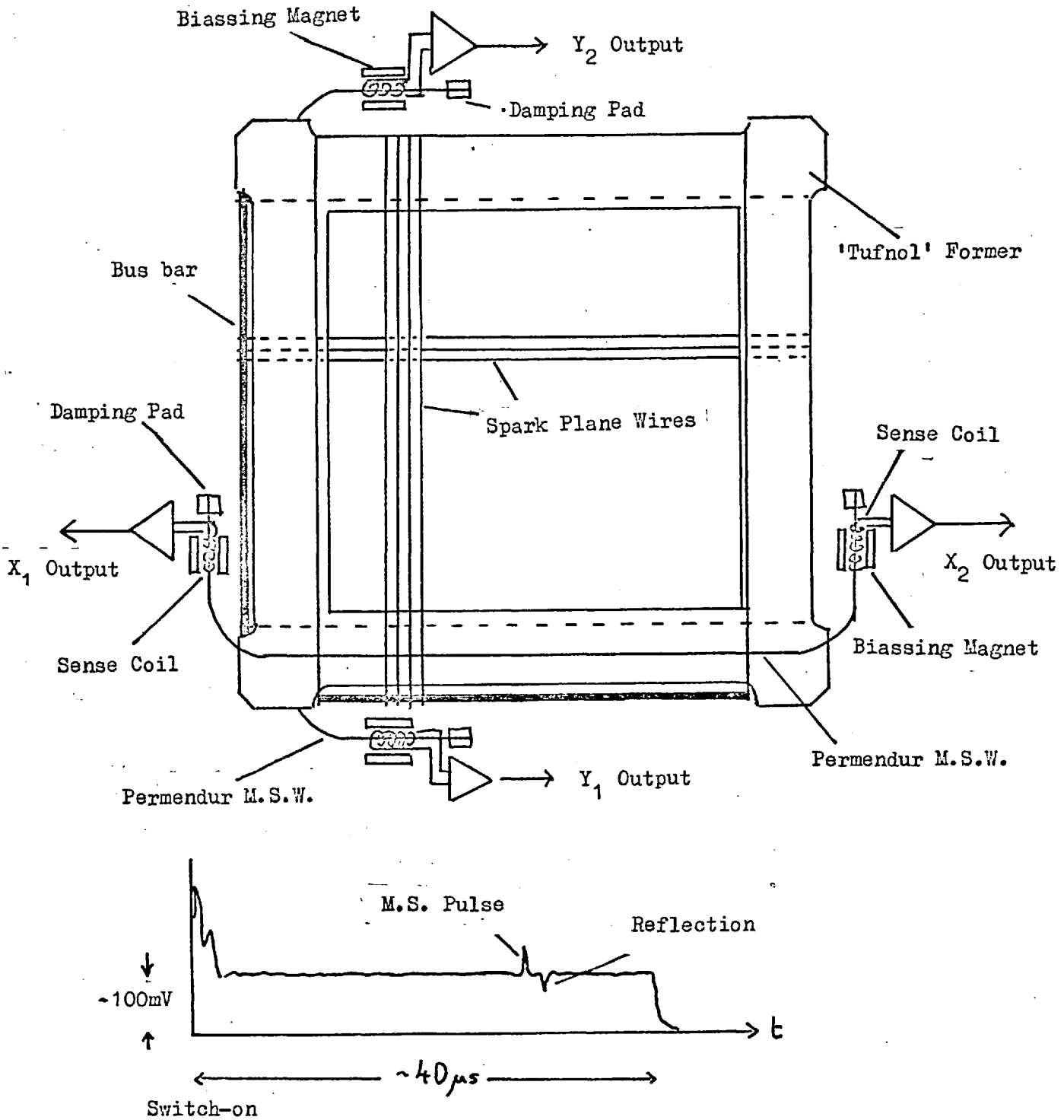


Figure 2.6a A schematic diagram of the spark module, indicating the position of the magnetostrictive wires.

b The form of the typical sense amplifier output.

shows the construction of each spark gap and the position of the M.S.W.'s and sense coils. The outputs of each sense coil were amplified and an output typical of each head amplifier is indicated in figure 2.6b.

There were eight sensors in all, allowing two measurements of each co-ordinate for a single track event (one spark in each plane). The time for the M.S. pulse to reach the sensing coil was determined individually for each sensor by gating open a 4.6 MHz free running oscillator (the frequency of which was halved), following an initial delay which was imposed to reduce spark interference. The detected M.S. pulse was shaped and gated the oscillator off at a time corresponding to the mid-point of the M.S. signal, and the number of complete oscillations in the intervening period was counted.

The timing clock was allowed to run for a maximum of 26 micro seconds after which time it was automatically gated off. Failure to detect a M.S. pulse on the wire resulted in an output delay count of 64 or 65 pulses, and since the maximum co-ordinate was equivalent to ~57 pulses, a count of 64 (or 65) cycles signified that the M.S. pulse had been undetectably small or that the gap had failed to spark. (In this case, all four sensors would not detect a pulse.) Failure to trace the signal on the M.S.W. was the main cause of inefficiency of the spark chamber.

The H.T. voltage was selected to give maximum sparking efficiency. However, before launch from Zambia further re-adjustment was required since a reduction in the atmospheric pressure at the higher altitude reduced the breakdown potential of the helium gas. When the spark voltage was lowered to compensate, no loss of efficiency was detected.

A clearing field was not applied to the spark gaps but no false tracks arose as a consequence. This was confirmed at ground level by triggering the detector at random with a pulse generator and less than 1% of these pseudo-events gave meaningful co-ordinates from the spark chamber electronics. This was as expected because the rate at which ionizing particles crossed each plane was less than one per millisecond while the recombination time for the ions in the trail was less than six microseconds (observed by delaying the spark trigger). Chance co-incidences at a trigger rate of ~ 20 per minute would therefore be rare.

2.4.1 Spatial and Angular Resolution

(a) Single track events

The co-ordinates of the spark position in both spark gaps were computed as follows:

$$x_i = (\rho_i + S_i - \rho_{i+1}) \times \frac{\rho c}{2} + zc_i$$

where x_i is the co-ordinate in cm.

ρ_i and ρ_{i+1} are the delays at either end of the magnetostrictive wire, measured in cycles.

ρc converts cycles to cm.

zc_i adjusts the origin in the spark chamber co-ordinate system.

S_i is the most probable value of $(\rho_i + \rho_{i+1})$.

The error in measuring x_i occurs due to digitization and spark spread, or jitter, causing a distorted current profile appearing at the magnetostrictive wire.

The timing frequency was 2.3 MHz and the velocity of the magnetostrictive pulse down the wire gave a conversion factor of 1 cycle per 2.2 mm. By combining the outputs of the complementary

sensors in this manner, the spark's position was estimable to within $\pm$ 0.2 cm. The inaccuracy due to the wire width and separation of 0.065 cm was relatively insignificant.

The shift in spark position for non-vertical tracks introduced a further source of inaccuracy but Allkofer (1969) has estimated the degree to which this effect occurred and showed it to be small compared with the error due to digitization in this instance.

On average, the particles entered the spark chamber, as a result of the geometry of the telescope, at an angle of about 20° from the vertical. The angular resolution in the spark inclination for such tracks was $\pm 1^{\circ}$.

(b) Double Track Events

The spark position for a double track event was located with less accuracy since the delay to each sensor was not combined with that of its partner in calculating the co-ordinates, which were computed thus:

$$x_{iI} = \rho_i \times \rho c_i + zc_i \qquad \text{— prong I}$$

$$x_{iII} = (S_i - \rho_{i+1}) \times \rho c_i - zc_i \qquad \text{— prong II}$$

This led to an angular error of $\pm 2^{\circ}$ in the measurement of the inclination of each prong of the pair, or an error of $\pm 15^{\circ}$ in the bisector.

2.4.2 Spark Chamber Efficiency

The main inefficiency was due to failure to detect a pulse on the M.S.W. by the read-out electronics. It might have been expected that there should be a fall in sparking efficiency as the zenith angle increased. However, Bradamente and Sauli (1967)

have previously demonstrated that within 40° (the detector half opening angle) the effect was small. From histograms of zenith angles of spark chamber events, no deviation from the expected cosine square dependence was noticeable for sea level muons. This isshown in Figure 2.7 where the observed angle of distribution of events is compared with that expected for muons as calculated for the opening angle of the telescope.

The overall spark chamber efficiency was evaluated from the event information as follows:

$$\xi = \frac{\text{number of events with 'meaningful' co-ordinates}}{\text{total number of spark chamber triggers}}$$

The events were deemed meaningless if they did not satisfy the following acceptance criteria:

(1) No '65' in the output data.

(2) The sum of the complementary co-ordinates for each wire did not exceed a realistic limit set empirically.

(3) If the tracks show evidence of a two prong event then the prongs should have had an apex in the lead converter (with allowance for scattering).

(4) The co-ordinates of the event fell within the circular geometry of the telescope.

If the pulsed electric field was not uniform between the spark planes, then preferential sparking could have occurred. Irregularities could have arisen due to 'kinks' in the plane and the field distortion at the edges. However, by care in construction, the former was avoided, and by design, the latter was eliminated. Both these effects were demonstrated to be absent from the accepted class of events, by plotting the distribution of sparks in each plane. No excessive sparking in any region was discernable.

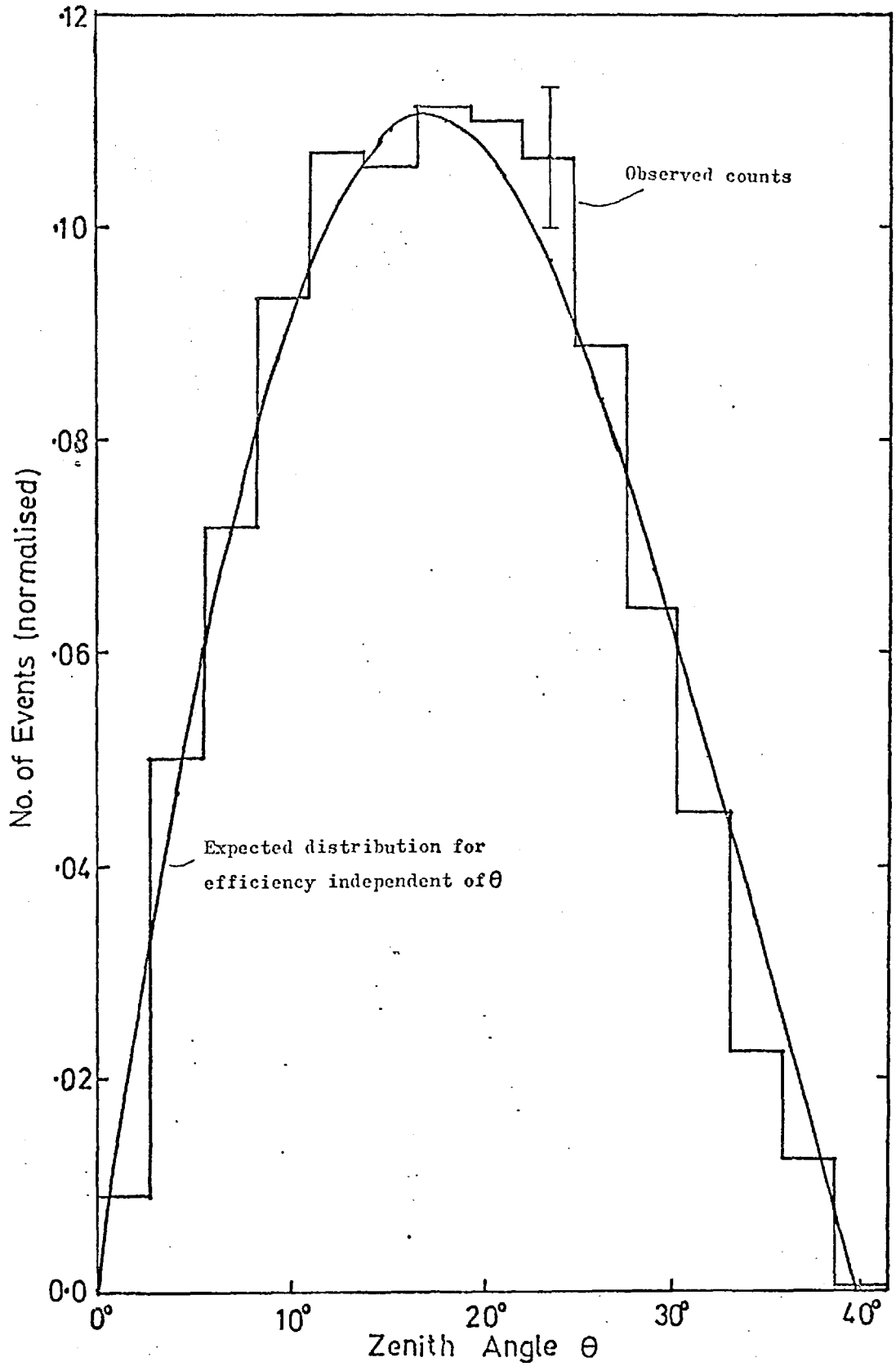


Figure 2.7 The angular response of the Detector and spark chamber to the sea level flux of cosmic rays.

2.5 The Cerenkov Energy Calorimeter

When an electron of energy $\geq$ 100 MeV is absorbed in lead glass it produces an electron-photon cascade which develops through successive pair production and bremsstrahlung interactions, the initial energy of the electron being shared among the secondary particles. The number of particles in the shower increases with depth but the energy of each generation diminishes until the pair production and bremsstrahlung processes no longer dominate and the remaining particles are absorbed by the Compton process and ionization.

An electron produces a shower population versus depth profile which is a function of its original energy. The primary electron and those secondary electrons whose energy exceeds the critical energy of the lead glass radiate Cerenkov light along their path before absorption or degradation in energy. The integrated light output of the shower indicates both its density and penetration and therefore provides a measure of the energy of the progenitor electron.

The development of the electron-photon shower in lead has been investigated using Monte Carlo techniques by Messel and Crawford (1970) and their results are indicated in Figure 2.8. The growth curves relate the number of particles in the shower to the depth t (in radiation lengths) for several energies. Of greater interest from the point of view of calibrating the response of the energy calorimeter are the curves of Figure 2.9 which indicate the total number of electrons which have occurred in a depth dt integrated over t. Since the scale is arbitary, only the relative values are of importance. However, it is seen that below a few radiation lengths, no further electrons are produced by a

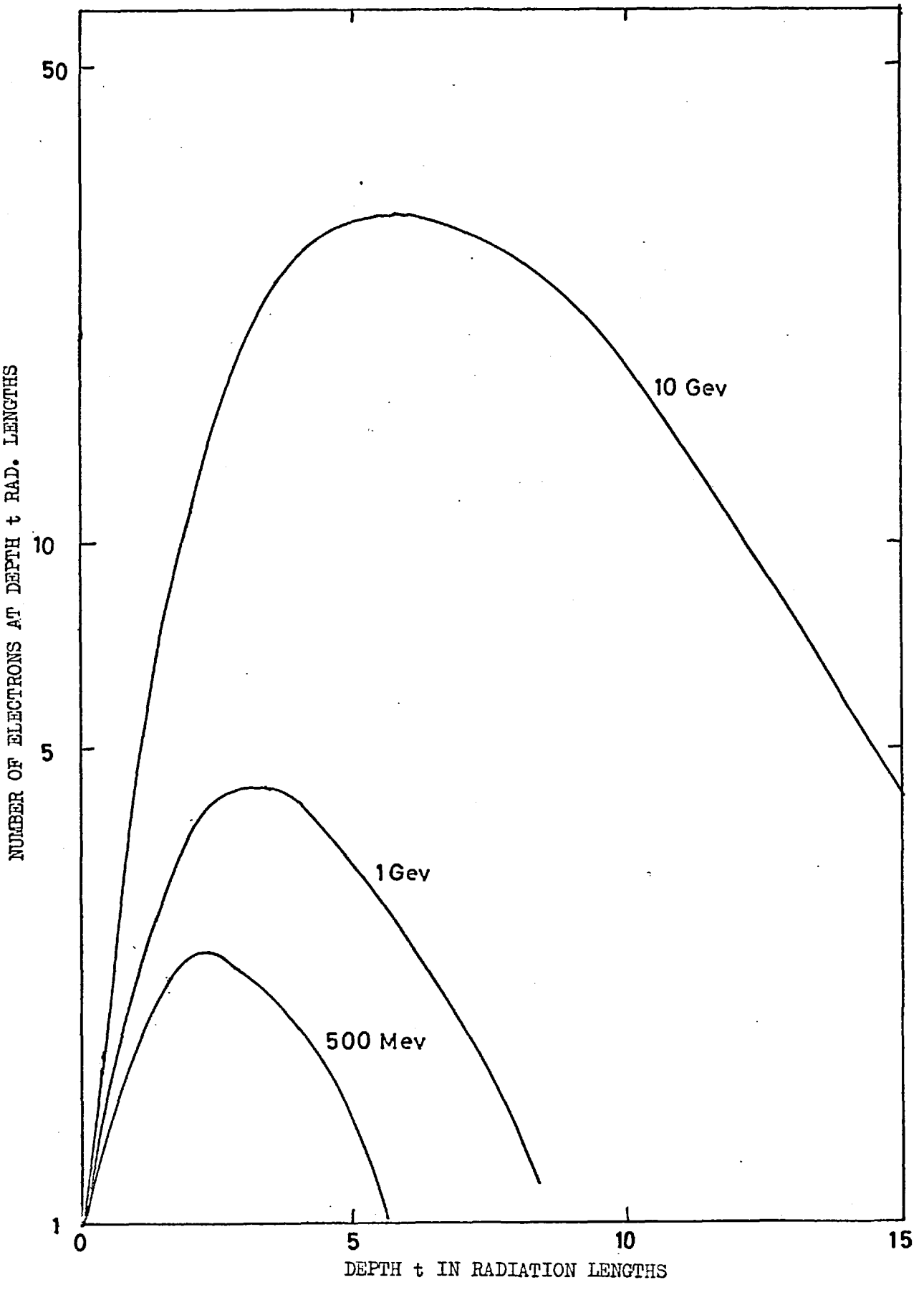


Figure 2.8 Growth curves for electron-photon showers in lead glass.

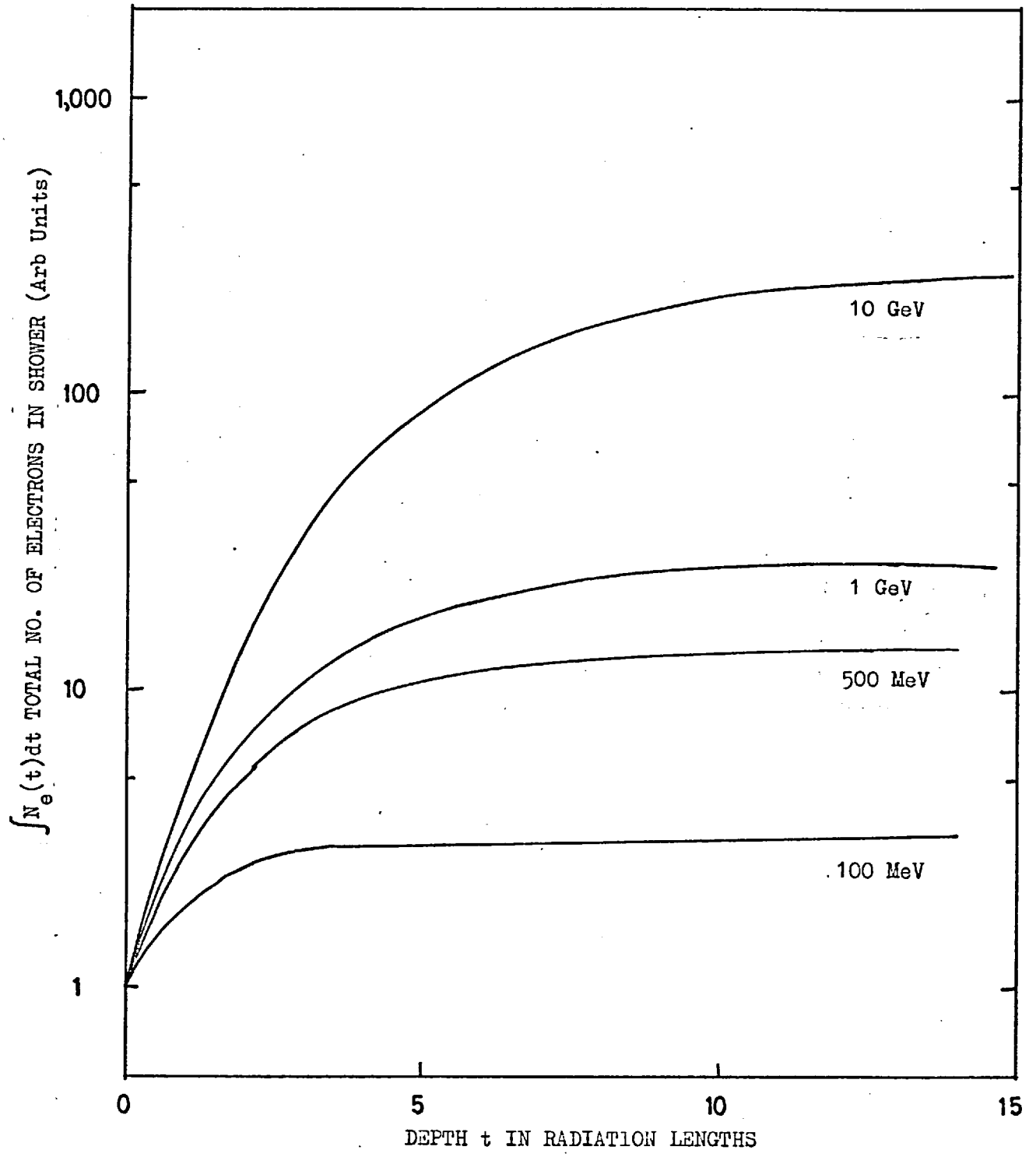


Figure 2.9 The integrated shower density for different energy electrons in the lead glass.

100 MeV primary electron, whilst a 5 GeV particle continues to deposit energy past a depth of 10 r.l. (although the important maximum in the development curve occurs at about 6 r.l.).

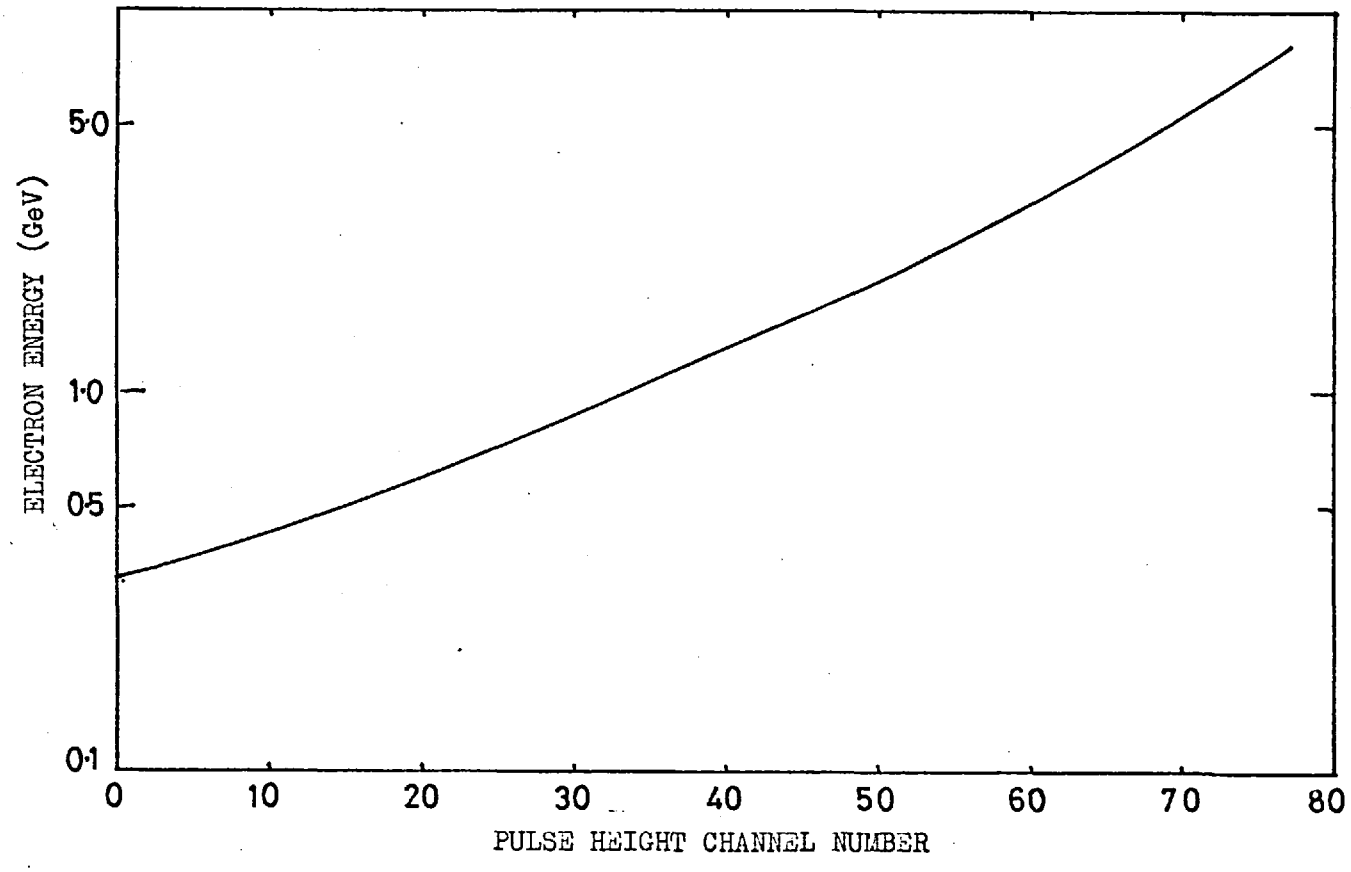
Calibration of the lead glass energy calorimeter was achieved by using the'Test Beam' facility of the NINA electron synchroton at Daresbury. A low flux pencil beam of electrons ranging in energy from 250 MeV to 4.4 GeV was detected and a pulse height distribution was plotted for several beam energies. A plot of mean pulse height versus energy in Figure 2.10a illustrates an approximate logarithmic relation.

From this curve, the width of the pulse height distribution for a particular energy was interpreted in terms of the energy resolution (H.W.H.M.) of the lead glass for each electron energy. The resulting resolution curve was extrapolated back to 100 MeV and plotted in Figure 2.10b.

Assuming equipartition of the gamma-ray energy between the electron and positron, the expected energy resolution resulting from a combination of the outputs of two electrons of half the gamma-ray energy was calculated and plotted in Figure 2.10b.

At low energies, the resolution was poor since few secondary electrons were generated in the shower and statistical variations were therefore large, as were variations in the photon output. Since lower energies were absorbed at the top of the glass, poor transmission to the photo-tube and a consequent reduction in the photo-electron production further reduced the resolution.

The energy of a gamma-ray was determined by firstly evaluating the path length of the shower in the lead glass by projecting the trajectory of the secondary electrons from the



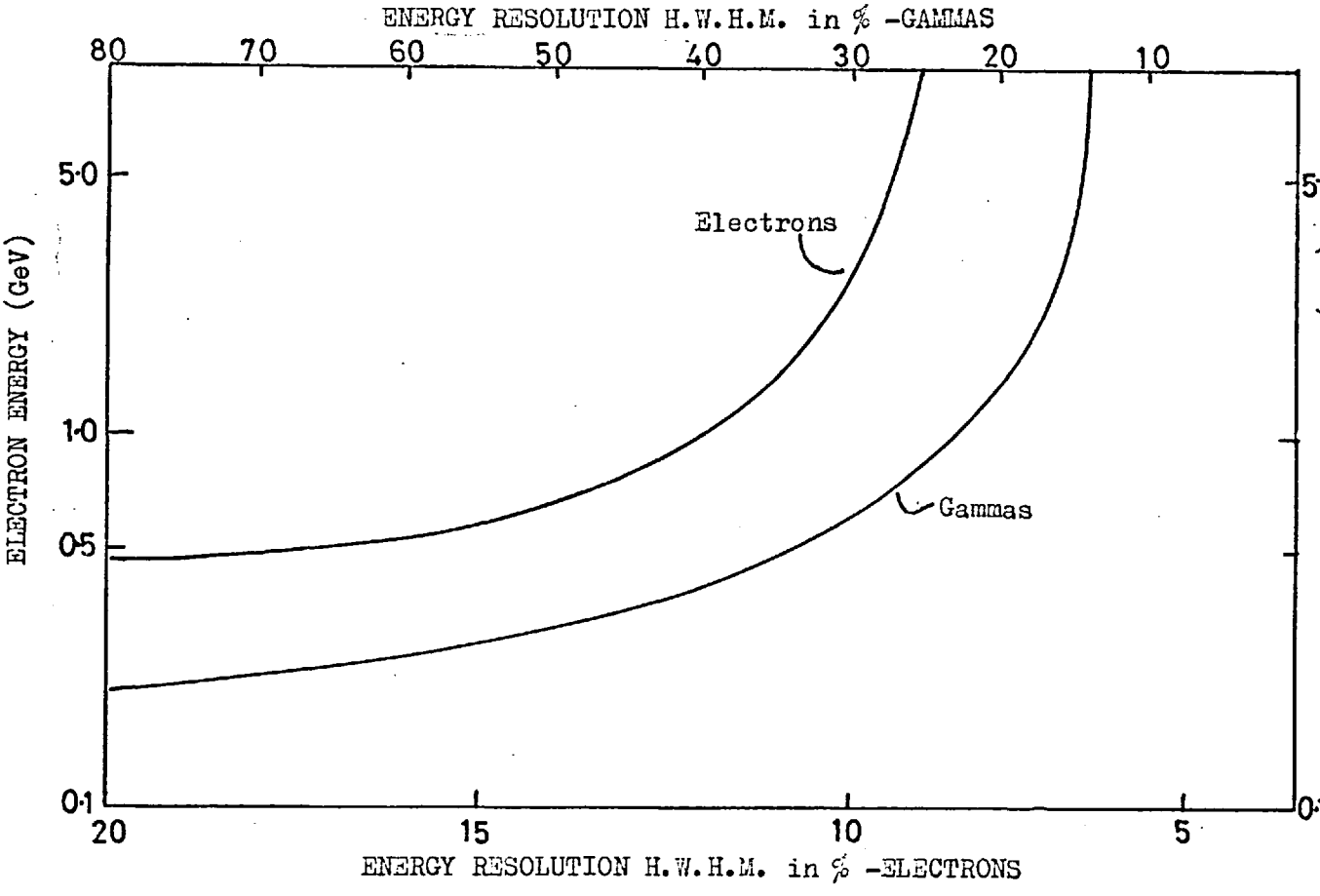


Figure 2.10a Calibration curve for the lead glass energy calorimeter and pulse height analyser.

b The energy resolution of the lead glass counter for electrons and converted gamma-rays.

spark chamber into the lead glass. The lateral spread of the shower was neglected, since this amounted to one r.l. after seven r.l. penetration for a 200 MeV electron shower (Messel and Crawford, 1970).

As the axial calibration electron beam was incident normal to the top surface of the lead glass, the electrons could be assumed to be totally absorbed in it. The energy of the electrons was well defined so the calibration curve obtained yielded a relation between the pulse height number and the energy deposited in the glass (Figure 2.10a). In the general case, the energy of an electron absorbed in the glass was inferred from the curves of Figure 2.9, knowing the path length of the electron in the glass and the pulse height measurement of the energy deposited (i.e., the shower density axis of Figure 2.9 was calibrated against the PHA). Figure 2.8 shows that the energy is deposited by the electron pair mainly in the first $2\frac{1}{2}$ r.l. of the lead glass for electrons of energy $\lesssim$ 500 MeV. Hence the energy deposited by the electron and positron did not differ significantly provided both travelled more than $2\frac{1}{2}$ r.l. The single tracks were assumed to be unresolved pair events and the mean electron (positron) energy was calculated for this type of event, and for resolved pair events, from half the deposited energy (given by the pulse height measurement) and the mean path length of the electron and positron. The gamma-ray energy was obtained by doubling the mean electron energy.

In addition to the reference point on the PHA scale given by the muons a second calibration reference was provided by the pulse height measurement of the light output of a photo-diode flasher fixed at the top of the lead glass element. This facility provided in-flight calibration and an essential check on the electronics and photo-multiplier. The flasher was activated by a sun-sensing device described later (Section 2.6.4).

2.6 The Aspect Sensors

In order to determine the arrival direction of the incident gamma-ray in the celestial or galactic co-ordinate system from its track in the spark chamber, the following information was required:

(1) The latitude and longitude of the detector.

(2) The orientation of the detector in terrestrial co-ordinates.

(3) The time of occurrence of each event.

The following sections discuss how these quantities were determined.

2.6.1 Detector Tracking

The distance from the detector at altitude from the ground station was continually monitored by means of an on-board 'transponder', which received a square wave modulated signal on 108 MHz waveband and then retransmitted it on the data channel (136 MHz). A second 136 MHz receiving aerial was used to measure the bearing of the detector. The output of each identical Yagi array of this second aerial was combined after introducing a π phase delay to one of the signals by lengthening the connecting cable. Since the polar diagram of each array peaked sharply in the forward direction, when both were directed towards the distant source a null was observed. When the aerial array was so positioned, its pointing direction was measured with a magnetic compass, thus giving the bearing of the detector. The error in this measurement was of the order of a few degrees, but by plotting the progress of the detector and its bearing, measured at frequent intervals, the flight history was determined with sufficient precision to give the position of the detector accurate to within $\pm \frac{1}{4}^{o}$ in both latitude and longitude.

2.6.2 The Magnetometer

The orientation of the detector at the time of the event was determined by a simultaneous measurement of the magnetic field by a three axis magnetometer, the mode of operation of which has been discussed in detail by Sanderson (1972). The magnetometer elements (manufactured by Smith's Industries) were set orthogonal to within 1/20 degree and the sensor was positioned at the end of a boom, one metre long, in order to reduce the effects of stray fields from the detector. The output of each sensing element was digitized and with a range of 511 numbers (9 bits), a sensitivity of 123 gammas (1 gamma = 10^{-5} Gauss) per number was set for all three sensors.

Provided the payload was hanging vertically below the balloon, the X and Y horizontal field values alone gave an estimate of the orientation of the detector with respect to the earth's horizontal field component.

Used in conjunction with computed field values given by a theoretical model of the earth's field, the limiting accuracy of the magnetometer (see below Section 3.5) was $\pm \frac{1}{2}^{o}$ in azimuth.

2.6.3 Event Timing

The time of occurrence of each event was added to the data after reception at the ground station. The electronic clock was digitized in twenty second intervals, a figure limited by the frequency response of the magnetic tape-recorders used. It was not intended to look for fast time varying phenomena so the resolution was sufficient to enable chronological recognition of the events in the ensuing analysis.

2.6.4 Solar Sensor

A solar sensor provided in-flight calibration of the detector aspect sensors and, by causing the photo-diode to flash, the Cerenkov counter and PHA. It consisted of a cylindrical drum with three vertical slits, equally spaced, each viewed by a photo-transistor situated opposite. As the balloon payload rotated, the sun passed across the slits and, providing no gamma-ray event was being processed, the light incident on the photo-transistor caused it to switch on and a 'pseudo-event' was triggered. The event word, which was identical to the gamma-ray word, transmitted the following information:

(a) The identity of the switched photo-transistor.

(b) The timing delays from each of 8 sensing circuits, which, since no spark was fired, should all have counted the maximum delay of 64 (65) cycles (Section 2.4).

(c) The size of the light output from the photo-diode flasher at the top of the lead glass, as measured by the PHA.

(d) The readings of the magnetometer.

Transmission of this data enabled a periodic check to be kept on many aspects of the detector while at altitude.

2.7 Electronics and On-Board Data Handling

(a) Power Supplies

Twelve volt 'Deac' rechargeable Ni-Cd batteries were the primary source of power arranged in 12v and 24v packs. The capacity of each pack was sufficient to give a detector lifetime of ~15 hours, providing 1.5 watts and 6 watts respectively.

Low tension converters satisfied the different voltage

requirements. A monolithic voltage regulator (Type LM305) was included in each circuit which provided output voltage stability of $\pm\frac{1}{4}\%$ when the temperature varied by $\pm 20^{\circ}C$ and the 24v input supply was varied by $\pm$3v. The efficiency of each converter was typically 80%.

There were three high tension supplies, one of which was a 1.8Kv ringing choke converter which powered the photo-multiplier tubes of elements ACD. The output of the converter was stabilized by a corona-stabilizer in a feed-back loop.

The high voltage supply which charged the two spark chamber storage capacitors provided about 8Kv, the precise value of which could be varied by adjusting the reference voltage at the first stage of a Cockcroft- Walton voltage multiplier chain (set by a corona-stabilizer). This voltage could also be varied by altering the output tapping on the chain. This converter also powered the photo-tube of scintillation element B by tapping the voltage multiplying chain at ~ 1000v . A 250v supply provided the 'keep-alive' current of the KN-22 Krytron tubes and the 250v line in the spark chamber pulser (Figure 2.5)

(b) On-Board Data Handling and Transmission

The gamma-ray event information was digitized as follows:

Information	Number of Channels	Length of Word	Dynamic Range
Spark chamber	8	7 bits	127
Pulse Height Analyser	1	7 bits	127
Magnetometer	3	9 bits	511

Each item of information was stored in a Random Logic counter. In addition to the main event information, five further bits were available, of which three were set by the output of the solar sensor, the rest being redundant.

Once the entire event information had been digested the stream of words were clocked out sequentially at the rate of 200 bits per second. Each clocked level corresponded to a 'zero' or 'one' binary state, which initiated a 1 msec or 2 msec wavetrain respectively from a 14.5 KHz oscillator. In this way a degree of noise immunity was achieved, since the 'zero' and 'one' levels corresponded to a train of ~20 and ~40 pulses respectively.

The stream of wave trains modulated the output of a 136 MHz F.M. transmitter generating 97 pulse trains of differing lengths. During the read out time of 0.5 seconds, the coincidence circuit was suppressed and this instrumental dead time was a factor to be considered, when evaluating the results.

When a primary charged particle event was registered a 5.4 KHz modulation was provided to the transmitter for a period of ~ 4 ms.

The radiated power from the transmitter was ~500 milliwatts which was found in practice to be sufficient to give a flight range of approximately 600 Km before the inevitable loss of contact as the payload fell below the horizon.

(c) Pressure and Temperature Gauges

In flight measurement of pressure and temperature was provided by two 'Olland cycle' devices on board each detector. Each gave a measurement of the atmospheric pressure, on both a coarse and fine scale, and the temperature.

The information, which was in morse code, from one Olland cycle was transmitted at a subcarrier frequency of 1.2 KHz and the other at 2.3 KHz. The power for these motor driven devices

was supplied by their own batteries, which reduced the interference with the other low voltage lines.

2.8 Environmental Stability of the Detector

The detectors were built and tested to withstand the extremes of temperature and pressure experienced in a balloon flight. The individual elements were rigorously tested in production, and the integrated system was run under near vacuum and refrigerated conditions. No change in performance was detected over the ranges to be experienced in flight.

The payload was enclosed in a Styrofoam box to provide thermal insulation in flight. The outside of the box was partially blackened to absorb radiated heat in an attempt to maintain a detector temperature of about 15°C.

2.9 Contamination of the Gamma-Ray Event Channel by Spurious Events

Since the primary gamma-radiation is weak in intensity it was vital that spurious effects, which would otherwise contaminate the gamma-ray channel, were either rejected or recognized and discarded.

In addition to the charge particle contribution, which was eliminated by the anticoincidence shield and duly categorized, there existed possible events which would trigger the coincidence logic and would resemble a gamma-ray. The importance of such events is discussed in the following sections.

(a) Neutron Induced Events

In these events a neutron which passed undetected through

the veto-counter interacted in the lead converter to produce a proton with sufficient energy to trigger the coincidence telescope elements B,C and D.

The rate of occurrence was estimated by considering the flux of atmospheric neutrons reported by Eyles et al. (1972) of 4×10^{-3} cm^{-2} sec^{-1} str ($E_{neutron} > 50$ MeV). The results of Hadley and York (1950) indicate that the probability of a 90 MeV neutron interacting in $\frac{1}{2}$ r.l. of lead producing a proton of energy > 20 MeV was 0.15%. As the range of a 20 MeV proton is ~ 1 gm cm^{-2} - equivalent to 1/3 r.l. of lead or 1/6 r.l. of lead glass it would be unlikely to reach the Cerenkov element D and trigger the detector.

The neutron spectrum is steep ($\propto E^{-2}$) so the expected contribution to the gamma rate from neutrons was negligible.

(b) Chance Coincidences

The chance coincidence rate (C) for three photo-multiplier type counters is :

$$C = 3 \times C_1 \times C_2 \times C_3 \times T^2 \quad \text{sec}^{-1}$$

(Janossy, 1948)

C_1, C_2 and C_3 were the individual counting rates of each photo-tube (due mainly to thermal noise) and T was the resolving time of the coincidence circuits.

The individual count rates were approximately 10^3 per minute and the resolving time was approximately 150 nsec so the chance coincidence rate was about 5×10^{-6} min^{-1}. An order of magnitude increase in C_1, C_2 and C_3 would still only result in one event per day.

A greater chance of a coincidence between a noise pulse in B with a cosmic ray produced coincidence pulse in C and D, was

possible. The rate predicted for this type of event was one per three hours.

In view of the low rates expected and that the spark chamber had been demonstrated (Section2.4)to spark when triggered randomly (i.e., as in this case) with only 1% efficiency, chance coincidences were not considered a likely source of contamination.

(c) Shower Events

Only events in which upward moving particles were absorbed in the lead converter would be counted as gamma-rays since they would otherwise have been detected by the anticoincidence shield.

Sood (1969) has investigated the likelihood of shower events contaminating the gamma-ray channel of a detector of similar geometry. The spark chamber in the present system offered an additional means of discriminating against such events, so the contribution was likely to be less than the ½% estimated by Sood.

CHAPTER III

GROUND EQUIPMENT AND BALLOON FLIGHTS

3.1 Ground Equipment

The main receiving aerial was a twin 7 element Yagi array, adjustable in both zenith and azimuth to facilitate tracking of the detector and to achieve maximum signal. The signal was preamplified and monitored by an Eddystone VHF receiver.

The raw data was recorded on Channel 1 of a Tandberg Stereophonic tape-recorder. This data was filtered to extract the gamma-ray event information and the timing pulse added before being recorded on the second channel. Real time monitoring of the gamma-ray channel could not be achieved because the data clocking out frequency was set at 200 Hz in order to reduce the dead time. This was too fast to drive the 'FACIT' paper tape punch, so complete tapes were replayed at $\frac{1}{4}$ speed, and by inspection of the paper tape output, correct functioning of the detector was verified. House-keeping data and cosmic ray event count rate were continuously monitored in real time, as was the transponder range-finder signal, the delay between transmission and reception of which was observed on an oscilloscope trace.

3.2 The Balloon Flights

Two balloon flights were successfully accomplished on January 25th and February 9th, 1971 from Lusaka, Zambia, a launch site offering the opportunity of surveying the southern sky. The vertical cut-off rigidity for Lusaka was 11.6 GV (Shea and Smart, 1967) and the small primary cosmic ray flux at this high threshold produced a correspondingly small flux of atmospheric

FLIGHT	DETECTOR WEIGHT lbs.	DATE	LOCATION AND TIME OF LAUNCH	BALLOON SIZE $\times 10^6$ cu.ft.	MAX. ALTITUDE gm/cm^2	FLIGHT TIMES				TIME TO REACH ALTITUDE hrs
						Beginning		End		
						U.T.	S.T.	U.T.	S.T.	
1	112	JAN 25th 1971	LUSAKA 07.40	0.803	4.1	5.40	15.46	11.25	21.21	1.5
2	110	FEB 9th 1971	LUSAKA 06.25	0.45	11.1	4.25	15.35	10.13 (20mb alt.)	21.23	2.0

Table 3.1 Summary of the Balloon Flights

secondary background radiation which improved the sensitivity of the detectors (Section 2.1).

Whereas the primary gamma-ray flux was attenuated by the atmosphere, the intensity of the secondary radiation increased with atmospheric depth. With this in mind, large capacity balloons were originally chosen in order to reach a high altitude (low residual pressure). The altitude profile of Flight 1 (Figure 3.1) shows how constant float altitude of ~ 4.3 gm cm^{-2} was attained using an 803,000 cu. ft. 'Stratofilm' balloon (manufactured by Winzen Industries Incorporated, U.S.A.). Unfortunately, during the launch of the second flight, an accident resulted in the balloon being lost, and a smaller, reserve balloon was unable to reproduce the excellent performance of the first flight.

The variations in payload temperature experienced during both flights were within the tolerance limits of the detectors and are plotted in Figure 3.2 as a function of time.

Data reception lasted for six hours in Flight 1 before contact was lost as the payload passed beyond the horizon. The range-finder and tracking information indicated a velocity in excess of 130 Km/hr, which was unexpectedly high. Flight 2 lasted for approximately the same time.

3.3 Preliminary Data Analysis

3.3.1 Charged Particle Events

At high altitudes there was a risk of corona discharge occurring in the detector electronics. Although precautions were taken to reduce the likelihood of breakdown, it was essential that the resulting surges in count rates that generally accompany the phenomenon should be detected.

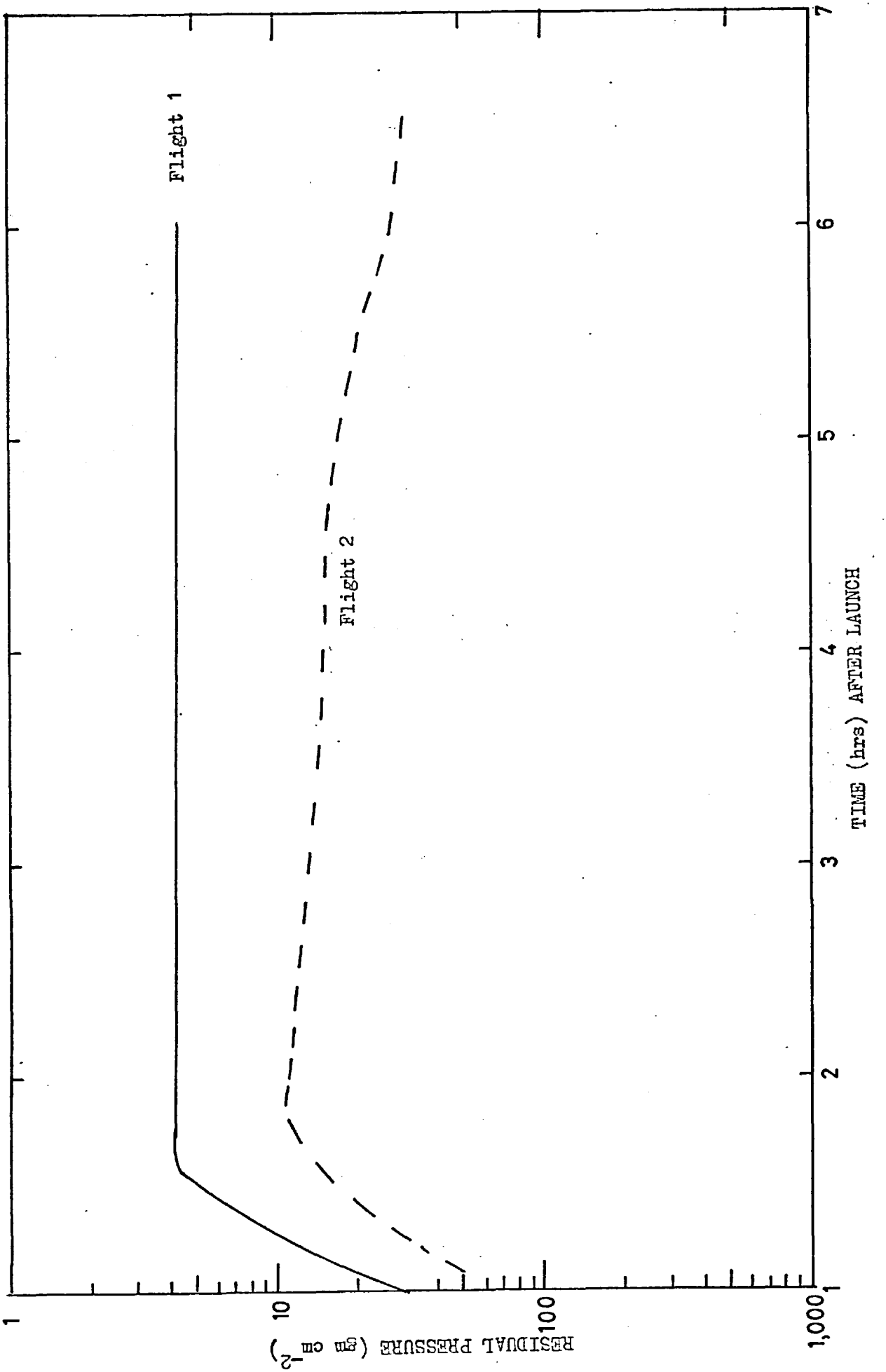


Figure 3.1 Altitude-time profiles for balloon flights.

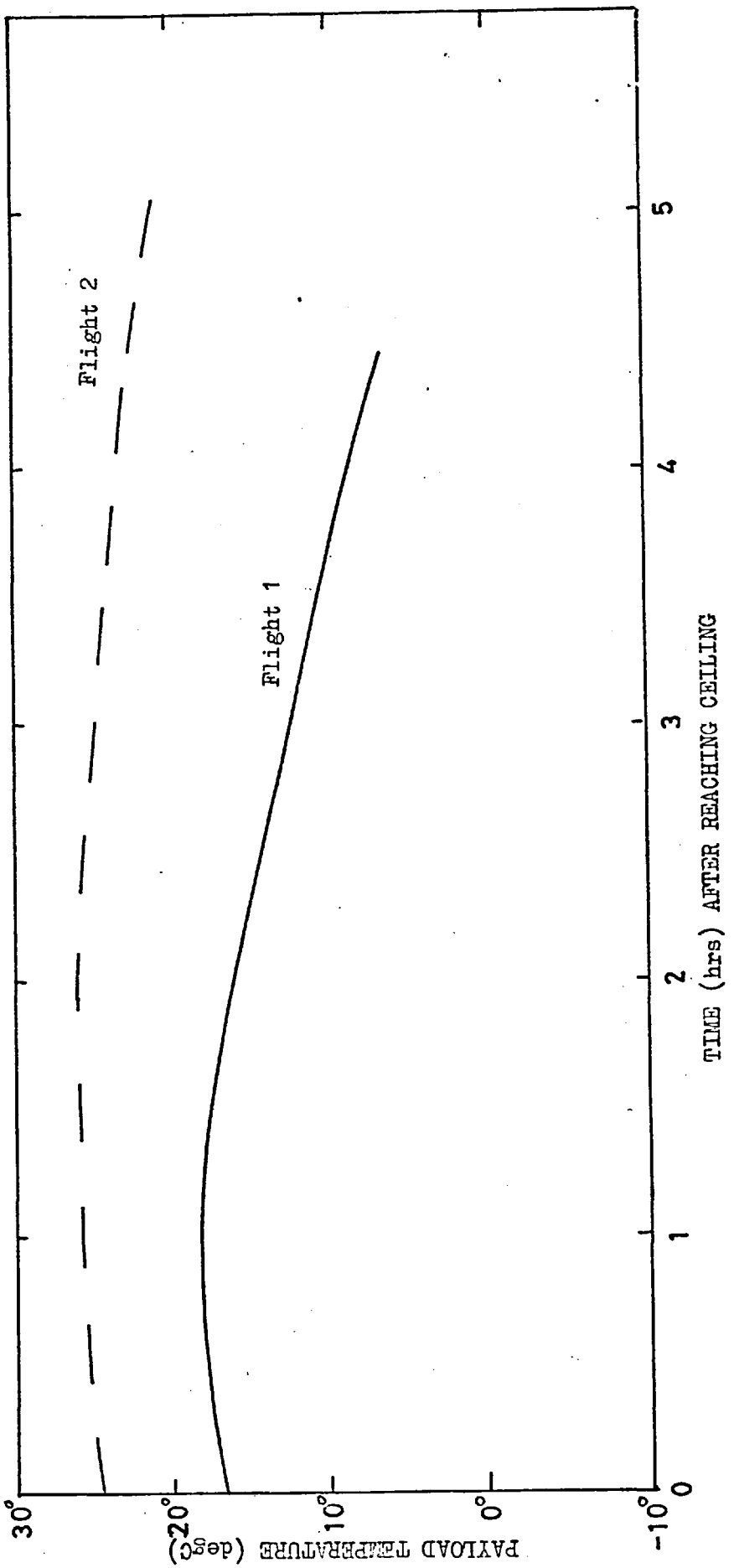


Figure 3.2 Payload temperature during balloon flights,

Flight 1 - payload 60% blackened.

Flight 2 - payload 75% blackened.

Transmission of the count rates of the individual photomultiplier tubes was not attempted since this would have placed increased demands on the transmitter and power supplies. Instead, the transmitted 4-fold coincidence rate of charged particle events was continuously checked.

The 4 ms (at 5.4 kHz) wave train recorded on the magnetic tape was filtered from the raw data using a band pass filter of band width $\pm 7\frac{1}{2}\%$. Each detected train initiated a pulse shaping device, the output pulse of which triggered a scaler. The rate of these 4-fold coincidences was plotted as a function of atmospheric depth (5 minute averages) for the ascent phase of Flight 1 and is shown in Figure 3.3. No tell-tale irregularities were noticed at any time during the ascent. The count rate firstly increased to the Pfotzer maximum then fell off as the detector climbed through the remaining atmosphere giving no evidence to suggest a detector malfunction.

For Flight 1 the altitude count rate was 160 $mins^{-1}$ corresponding to a rate of 3.2 events $second^{-1}$ after correcting for the dead time due to the average gamma trigger rate of 19 $minute^{-1}$.

The area-solid angle factor for the coincidence telescope of $\pm 42^{o}$ half angle was calculated to be 59 $cm^{2}str$, thus, the measured apparent charged particle flux was 540 $m^{-2}sec^{-1}str$.

Ormes and Webber (1966) measured the primary proton flux at a similar geomagnetic latitude to be 200 $m^{-2}sec^{-1}str$ so in comparison the observed flux appears high. The results of Ormes and Webber, however, do not include all the fast ionizing radiations which exist at 4.3 gm cm^{-2}, having eliminated back-

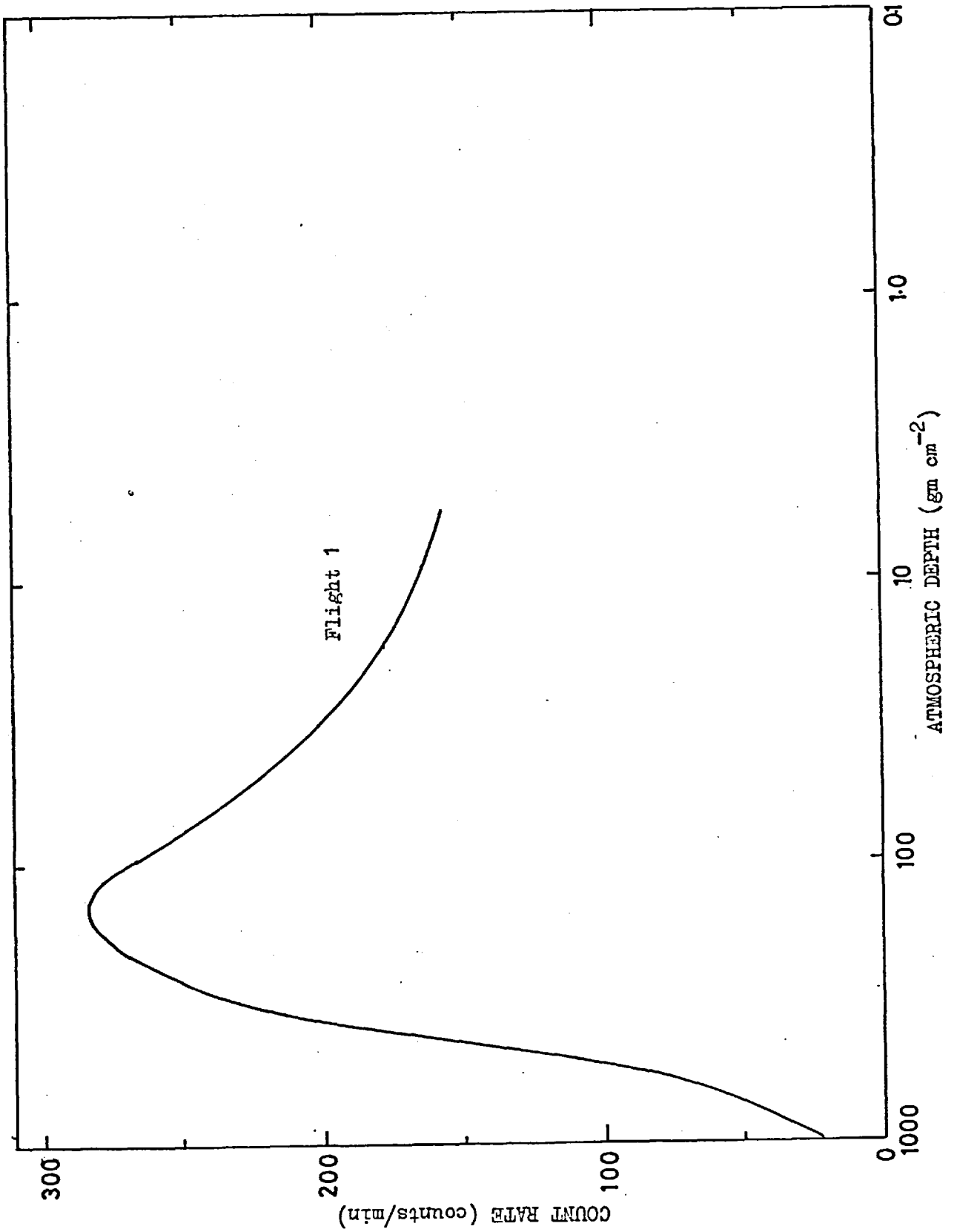


Figure 3.3 Variation of charged cosmic ray count rate during the ascent of Flight 1.

ground and albedo by pulse height discrimination.

The sum of the charged secondary products of nuclear interactions (Perola and Scarsi, 1966) would account for only part of this difference but König et al. (1970) have reported that at 12 GV cut off albedo radiation could contribute as much as 55% of the total fast particle intensity. Though this result goes far in explaining the apparent discrepancy, an absence of pulse height information in the present experiment prevented a corroboration of König's results.

A further source of background was the lead glass element in which there was a high probability for nuclear interactions to take place with the cosmic ray nuclei. The secondary ejecta from these events triggered the coincidence telescope and simulated a cosmic ray type event. The disagreement between the accepted proton flux and the observed trigger rate was not considered excessive and the channel served its designed rôle as a check on detector malfunctions effectively.

3.3.2 Gamma-Ray Events

The half second wave train of the gamma-ray data word was filtered from the raw data channel at the sub-carrier frequency of 14.5 kHz at which it was transmitted and, like the cosmic ray events, was counted by a scaler.

The ascent curve for the gamma-ray trigger rate obtained for Flight 1 and Flight 2 was recorded and plotted in Figures 3.4 and 3.5 after correcting for dead time effects. When the curves were extrapolated to zero millibars pressure both implied a large primary flux, but little significance was given to these estimates as the raw gamma-ray event data included false triggers and solar sensor triggered calibration

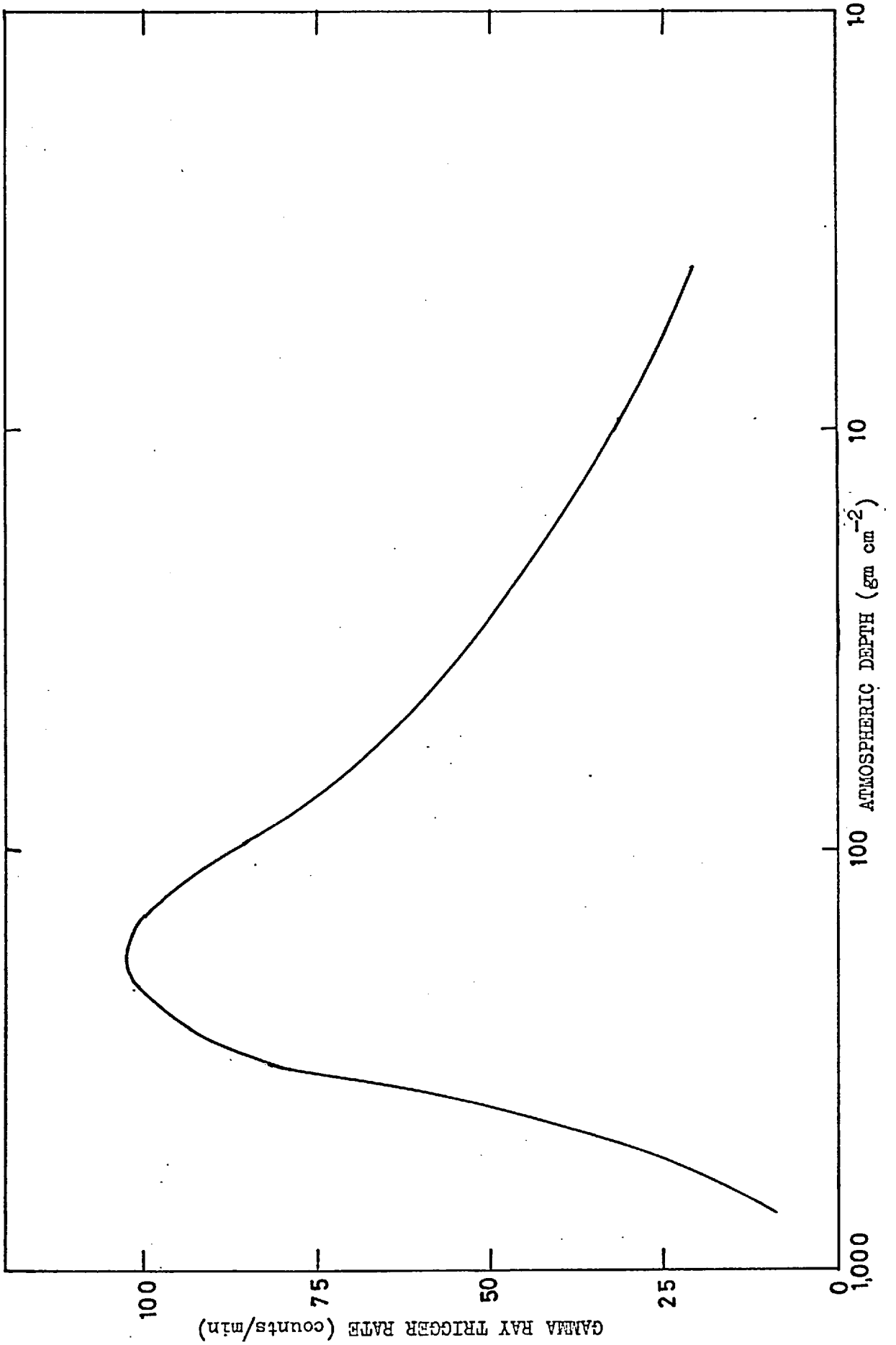


Figure 3.4 Variation of gamma-ray trigger rate during the ascent of Flight 1.

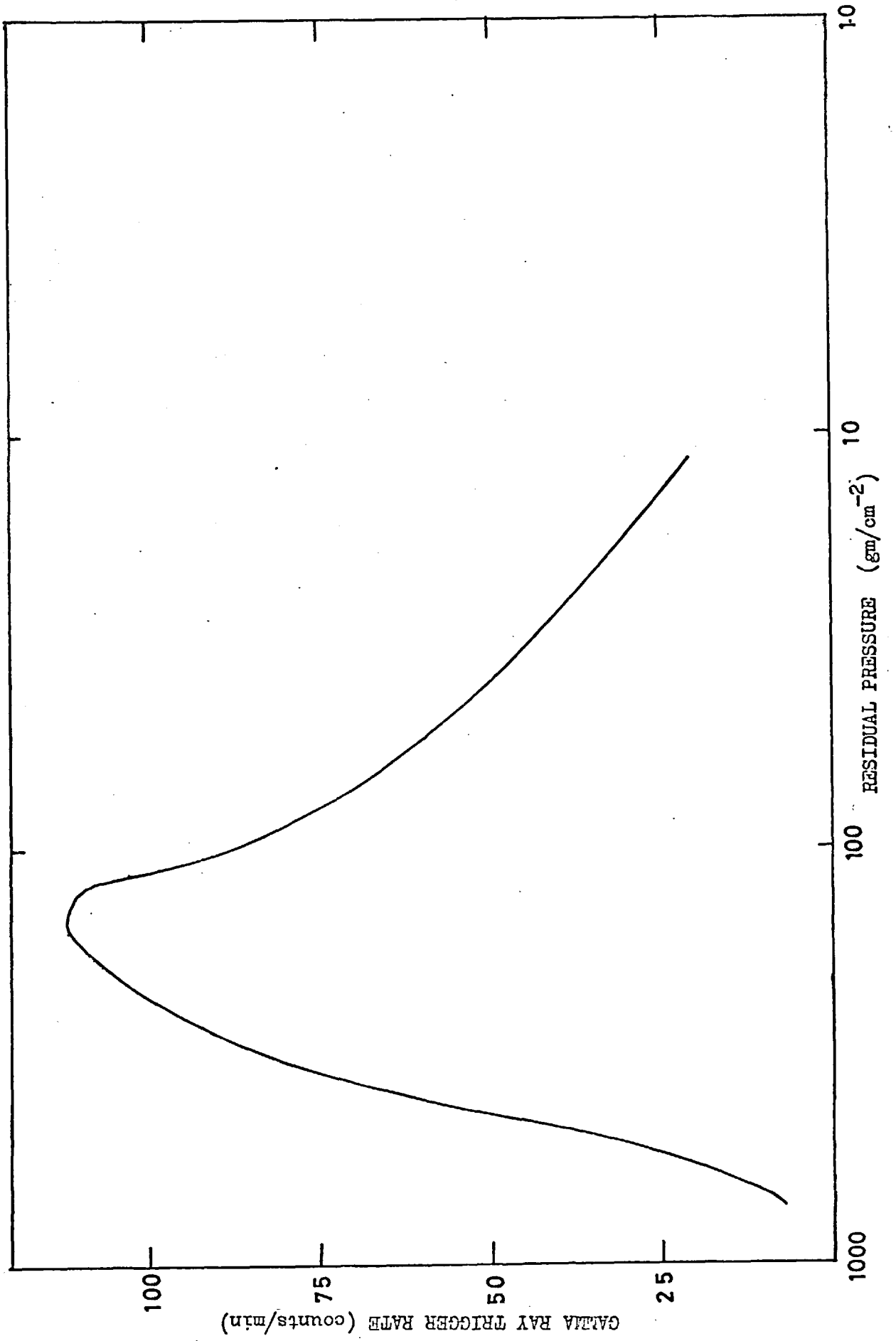


Figure 3.5 Variation of gamma-ray trigger rate during the ascent of Flight 2.

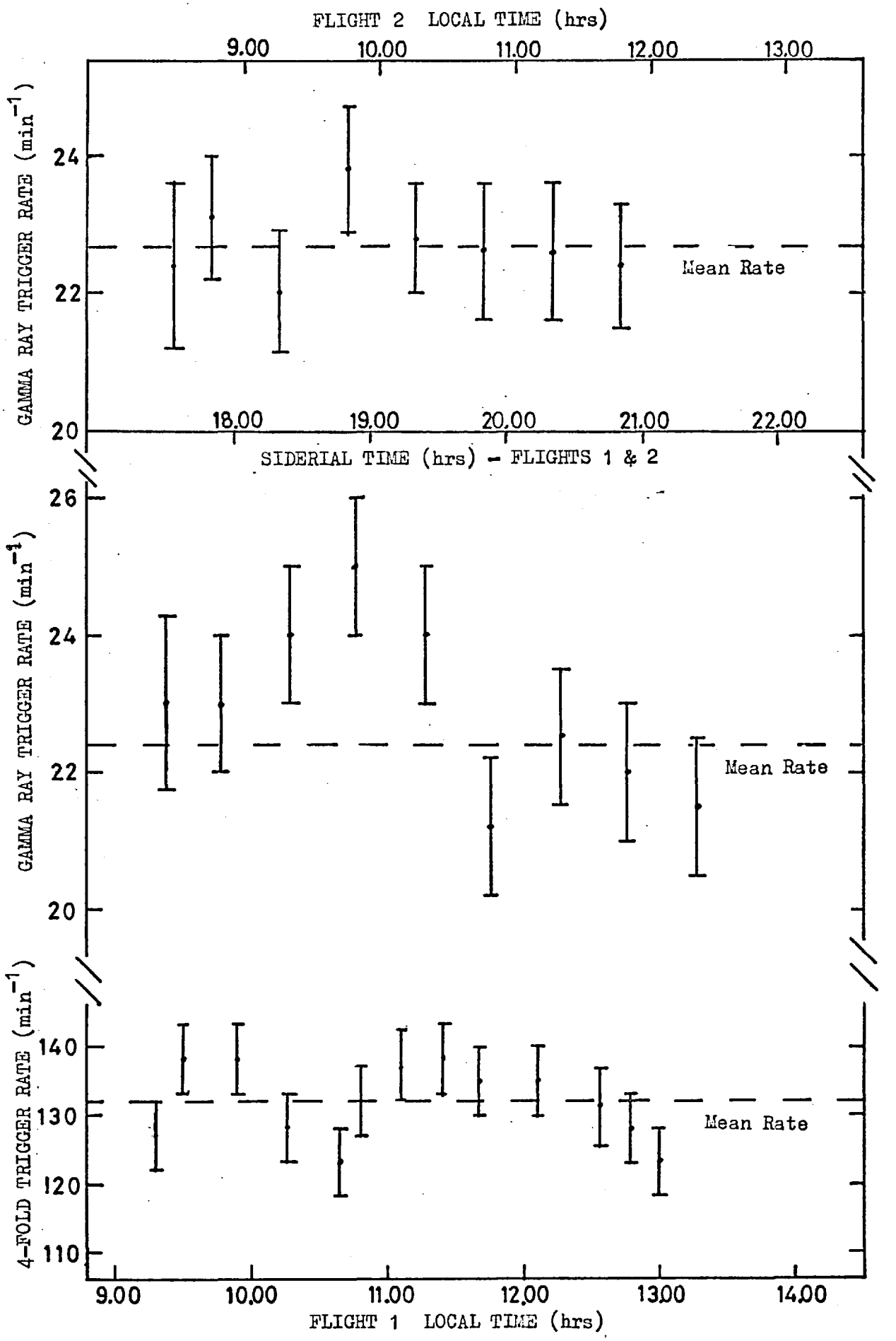
events. These were later sorted by stringent computer reduction of the data.

The steep slope of the ascent count rate curve as the payload approached ceiling is contrasted with that obtained for the cosmic ray channel. The contribution due to background was less in evidence in the gamma-ray curve and comparatively good rejection of splash albedo and nuclear interaction induced events was implied.

The gamma-ray trigger rate at altitude averaged over thirty minute intervals (and corrected for dead time effects) for Flights 1 and 2 was plotted in Figure 3.6 against both local time and Siderial time. Owing to the slow descent in Flight 2, the average count rate increased as the flight progressed, which necessitated normalization of the count rates to that at 11.3 mb, the maximum altitude.

The 4-fold trigger rate for flight 1 is also displayed in Figure 3.6 to indicate that no detector malfunctions were apparent while at altitude.

It was noteworthy that there was an enhancement in the gamma-ray trigger rate which occurred during Flight 1 at about 19.00 Siderial time. No corresponding increase was evident in the cosmic ray channel, indicating that it was unlikely to have arisen from a variation in detector response. It was understandable that no similar effect was observed during Flight 2 since the detector was at a lower altitude, so if the increase was dug to the transit of a primary gamma-ray source, it would have been shrouded by the increased background flux.



Flight 3.6 Comparison of the gamma-ray trigger rates of Flight 1 and Flight 2 (corrected for dead time), and the 4-fold coincidence rate of Flight 1, as a function of both Local and Siderial time.

3.4 Detailed Gamma-Ray Event Analysis

The major part of the analysis was carried out using a C.D.C. 6,600 computer. The data was presented to the computer in paper tape form and encoded on to magnetic tape for ease of access. Flight data was recorded at the rate of about 1 paper tape per 45 minutes at altitude, and by cataloguing all the flight data on a single magnetic tape, the entire flight could be processed by a single programme.

Two computer programmes were used, a calibration, or test-run, programme and a flight data programme. The calibration programme analysed ground level muon events by performing the following operations:

(1) Reject the events if the spark chamber co-ordinates do not comply with the event acceptance criteria (Section 2.4.2)

(2) Create histograms of

- (a) spark chamber co-ordinates
- (b) sum of complementary co-ordinates for each wire
- (c) PHA output
- (d) magnetometer output for the accepted events

It was a tedious process to interpret the data generated by the random-logic counters, so these runs enabled minor faults, e.g., spark interference or pick up in the counting circuits and failure in tracing the magnetostrictive pulse on the M.S.W., to be detected.

The flight data was to be accessed many times in the ensuing analysis so the decoded data from accepted events was

written on to a second magnetic tape and for each event, the following information was stored:

(1) original and new event number

(2) eight spark chamber co-ordinates

(3) PHA number

(4) magnetometer readings

(5) local time of event

(6) Siderial time of event

With the event information stored in this manner, complete analysis of each flight was completed in about 30 seconds of computer time, outputting the results on to a line printer.

3.5 In-Flight Detector Calibration and Orientation Accuracy

The solar sensor triggered satisfactorily in the early stages of both flights before the angle of elevation of the sun increased above the field of view of the photo-transistors. The pseudo-event words transmitted were sorted by the computer, 23 being recorded during Flight 1 and 17 during Flight 2.

For each of the calibration event words all the spark chamber timing channels showed the expected maximum count of 64 (or 65) and the pulse height measurements of the light output from the photo-diode light flasher were seen to be in excellent agreement with the distributions obtained before the flights (Figure 3.7).

The calibration events enabled the accuracy of the magnetometer to be checked by comparing the computed bearing of the sun with that given by the outputs of the solar sensor and magnetometer. The calculated and measured bearings agreed to within $\pm 1^{o}$.

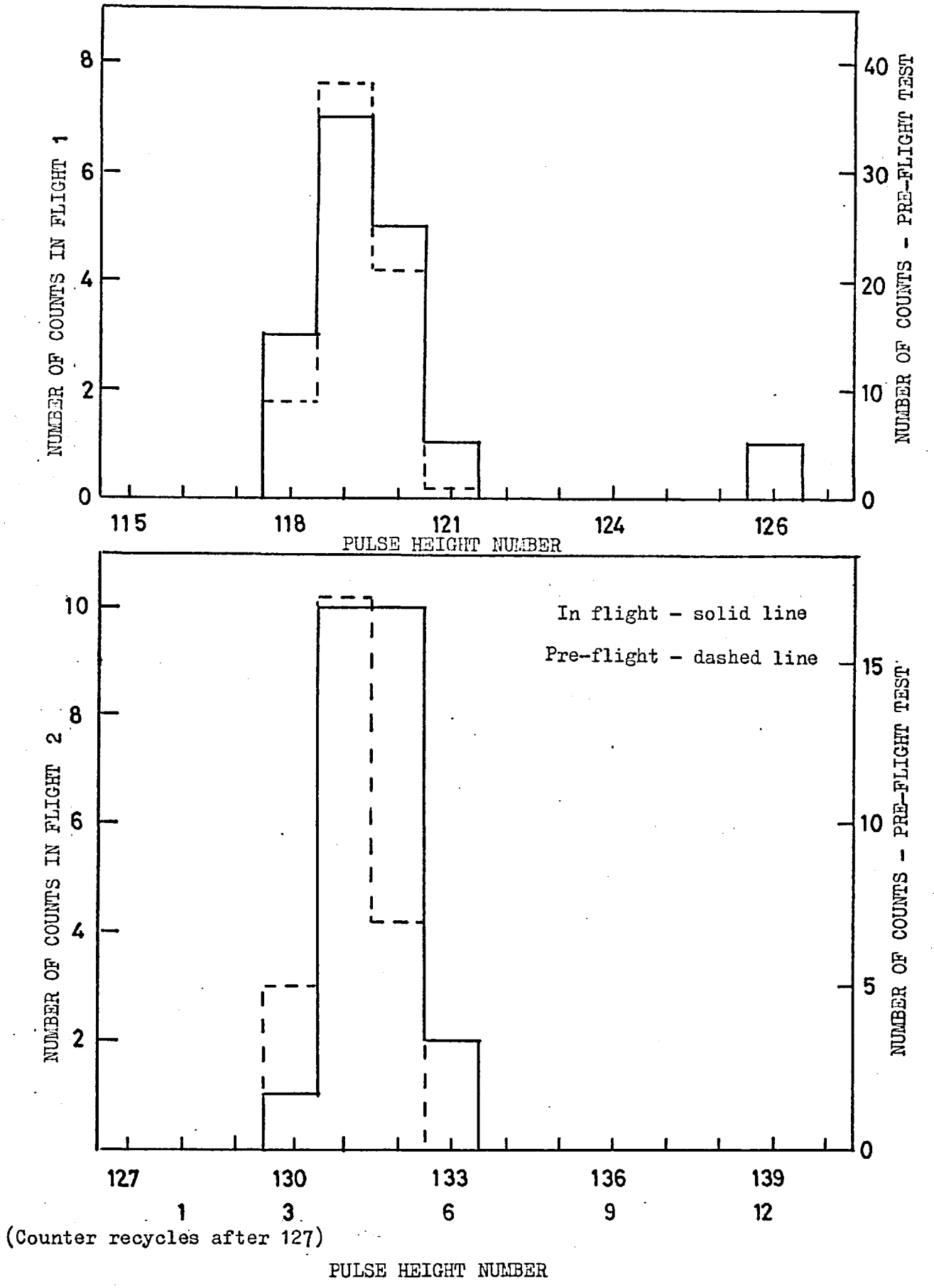


Figure 3.7 Pulse height measurements of the calibration light flasher for both flights.

The angular arror which arose because of the digitization of the magnetometer readings was $\pm\frac{1}{2}^{o}$ when the x and y values of the field (error of123γ's in each) were combined to calculate the angle to the horizontal field vector. The solar sensor drum was aligned with the spark chamber to no better than $\pm\frac{1}{2}^{o}$ while the magnetometer alignment was thought to be accurate to not less than $\pm\frac{1}{4}^{o}$ with respect to the spark chamber. Considering, in addition, that the angular diameter of the sun is $\frac{1}{2}^{o}$ the agreement between the experimental and predicted bearings was excellent.

The computer programme which analysed the flight data rejected those events in which the measured magnetic field was not in agreement with that computed by the International Geomagnetic Reference Field. (Malin, 1969) The I.G.R.F. model was an order of magnitude more accurate than the limiting accuracy of the detector's magnetometer when account of altitude, epoch, latitude and longitude of the detector was taken. Some events arose in the data in which interference had caused a random output from one or more of the magnetometer data channels. In analysis of these events the incorrect field values were substituted by interpolated readings of previous and later events where possible.

The payload was hung below the balloon in such a way that the vertical field measurement should have remained constant as the balloon rotated. By scrutinizing these B_z values, in conjunction with B_x and B_y, account could be taken of slight swinging and tilting observed during flight. The computer routine detected and corrected for the swinging which occurred at the beginning of the first flight. Overall, the permanent

tilt, either due to misalignment of the magnetometer sensor, or in the suspension of the payload was deduced to be less than $\frac{1}{2}^{o}$. For Flight 1, the magnetic field values varied as the balloon travelled towards the west, in agreement with the trajectory on a magnetic field map at 37 Km altitude. The variable height of Flight 2 produced corresponding variations in the field but using altitude-pressure data for equatorial regions (Shearman, Private Communication), it was again possible to correlate the flight path with the calculated field values.

3.6 Atmospheric Gamma-Rays

3.6.1 Comparison of Gamma-Ray Rates Observed in Flight 1 and Flight 2

Although the gamma-ray trigger rates during Flight 1 and Flight 2 (normalized to 11.3 mb) were comparable (Figure 3.6) it was observed that during the ascents of Flight 1 the rate at 11 gm cm^{-2} was about 50% higher than at ceiling (4.3 gm cm^{-2}). This apparent contradiction was resolved when measurements of the gamma-ray energies were carried out.

The growth curves of shower population in Figure 2.9 indicated that the difference in shower density for the various energies was not significant until after a few radiation length's penetration. For this reason, only those particles whose projected path length in the lead glass exceeded 2.5 r.l. were accepted for energy determination.

The consequent reduction in the effective opening angle of the detector was calculated and the results are shown in Table 3.2.

Class of Event	Effective Half-Opening Angle of Detector	Geometric Factor*
3-Fold Coincidence Events (γ-rays)	$\pm 42^{\circ}$	59.0 cm^2 str
'Acceptable' γ-ray events	$\pm 37^{\circ}$	44.5 cm^2 str
4-Fold coincidence	$\pm 42^{\circ}$	59.0 cm^2 str

TABLE 3.2 * Heristchi , 1967

At low energies two categories of events were discarded - those giving a 'zero' in the pulse height channel and those whose pulse height indicated that the energy deposited in the lead glass was less than that from a 200 MeV photon.

The first occurred because there were two discrimination levels on the Cerenkov counter. One level was set arbitrarily above the noise of the photo-tube and the other set the pulse height analyser threshold. A zero PHA output arose when the pulse was big enough to trigger the coincidence logic but was below the PHA threshold.

Events of the second type were due to low energy gamma-rays whose measured energy was below the 200 MeV threshold or Compton electrons and low energy electrons produced in pair production interactions and scattered into the detector geometry. (Section 4.2)

The number of gamma-rays observed in each flight whose energy exceeded 200 MeV was compared and after accounting for

Flight	Average Altitude	Rejected Events		Accepted Events	Normalized for Dead Time Efficiency & Exposure		Flight 2 Normalized Relative to Flight 1	Flux Ratio	Relative Flux from Ascent Curve Flight 1
		Zero Pulse Ht	Pulse Ht Low (E < 200 MeV)		Efficiency of spark chamber ξ	Dead Time Factor			
1	4.3 mb	308	300	578	62%	12/10	578	1	1 (20/min)
2	15 mb	66	457	934	54%	29/23	1140	1.97	1.9 (38/min)

TABLE 3.3

differences in detection efficiency, dead time and length of flight, the ratio of the fluxes at 15 gm cm^{-2} (approximate average for Flight 2) and 4.3 gm cm^{-2} were in the ratio 2:1. The rates at these two altitudes were measured during the ascent of Flight 1 to be in the ratio 1.9:1.

At 200 MeV, therefore, the count rates for each flight were in accordance with their different float altitudes (Table 3.3).

3.6.2 The Secondary Gamma-Ray Energy Spectrum

During 255 minutes of Flight 1, at ceiling 578 events were detected whose measured energies exceeded 200 MeV and the observed number of gamma-rays in the various energy intervals is shown in Table 3.4. (The bin widths are constant on a logarithmic scale.)

Energy Interval MeV	No. of Gamma-Rays Observed
200 - 320	157
320 - 500	137
500 - 800	94
800 - 1,300	78
1,300 - 2,000	55
2,000 - 3,200	20
> 3,200	17
> 7 GeV	0

TABLE 3.4

The spectrum of the secondary gamma-rays at 4.3 gm cm^{-2} was calculated according to:

$$I(E)\,dE = \frac{\text{No. of gammas observed in } dE \times f \times g(E)}{\varepsilon(E) \times A \times \Omega(E) \times \tau}$$

where the various terms have the following meaning:

$\varepsilon(E)$ = detection efficiency at energy E

A = area of the detector

τ = time of flight

$\Omega(E)$ = solid angle at energy E

f = dead time correction

$g(E)$ = correction for detector energy response

The flight lasted 255 minutes, the detector area (A) was 127 cm^2 and at the average gamma-ray trigger rate of 19 min^{-1} f≈1.2. The detection efficiency was a function of energy since pair production probability (Figure 2.4b) increased with energy. The effective opening angle $\Omega(E)$ of the telescope also varied with energy because of the scattering of the secondary electrons in the converter (Section 4.2).

An effect of the limited energy resolution of the detector was that at an energy boundary some photons of lower energy would have registered higher whilst some at higher energy than the boundary registered lower. Because the intensity of the photon flux decreased with increasing energy more gamma-rays registered high than registered low. The net effect was an over-estimate of the count rate in each energy interval, or, alternatively, a shift in the energy scale towards lower energies.

This 'spillage' effect was estimated for each energy interval by considering the energy resolution curve in the region near the energy boundaries and the shape of the secondary

gamma-ray spectrum as measured by Fichtel (1969) and Fazio et al. (1968) in the upper atmosphere at Palestine, Texas, (4.5 GV cut-off).

An exponent in the integral spectrum of 0.45 was consistent with both results and the resulting additional count rate in the 200 - 500 MeV energy interval was estimated to be 6% i.e.

$$g(E) = \frac{100}{106}$$

At higher energies the energy resolution was more or less constant (Figure 2.10b) and a 2% increase was estimated for the higher energy bins.

The differential energy spectrum as measured at 4.3 gm cm^{-2} for 11.6 GV cut-off is shown in Figure 3.8 with the derived spectrum of Perola and Scarsi for a similar cut-off rigidity.

3.6.3 Comparison of the Measured Spectrum with Other Results

Few experiments detecting gamma-rays have taken place at such high geomagnetic cut-offs so comparison with other data was difficult. An attempt has been made to normalize the present results with those measured under different experimental conditions.

Since the gamma-ray flux varies almost linearly with residual pressure at the top of the atmosphere, the results were normalized to unit atmospheric depth by dividing the flux observed at depth x by x gm cm^{-2}. This made it possible to compare measurements at different altitudes. A maximum depth of 11 gm cm^{-2} was considered.

The variation in the atmospheric gamma-ray flux with geomagnetic latitude is related to the variation in primary cosmic ray intensity. Figure 3.9 shows the variation in

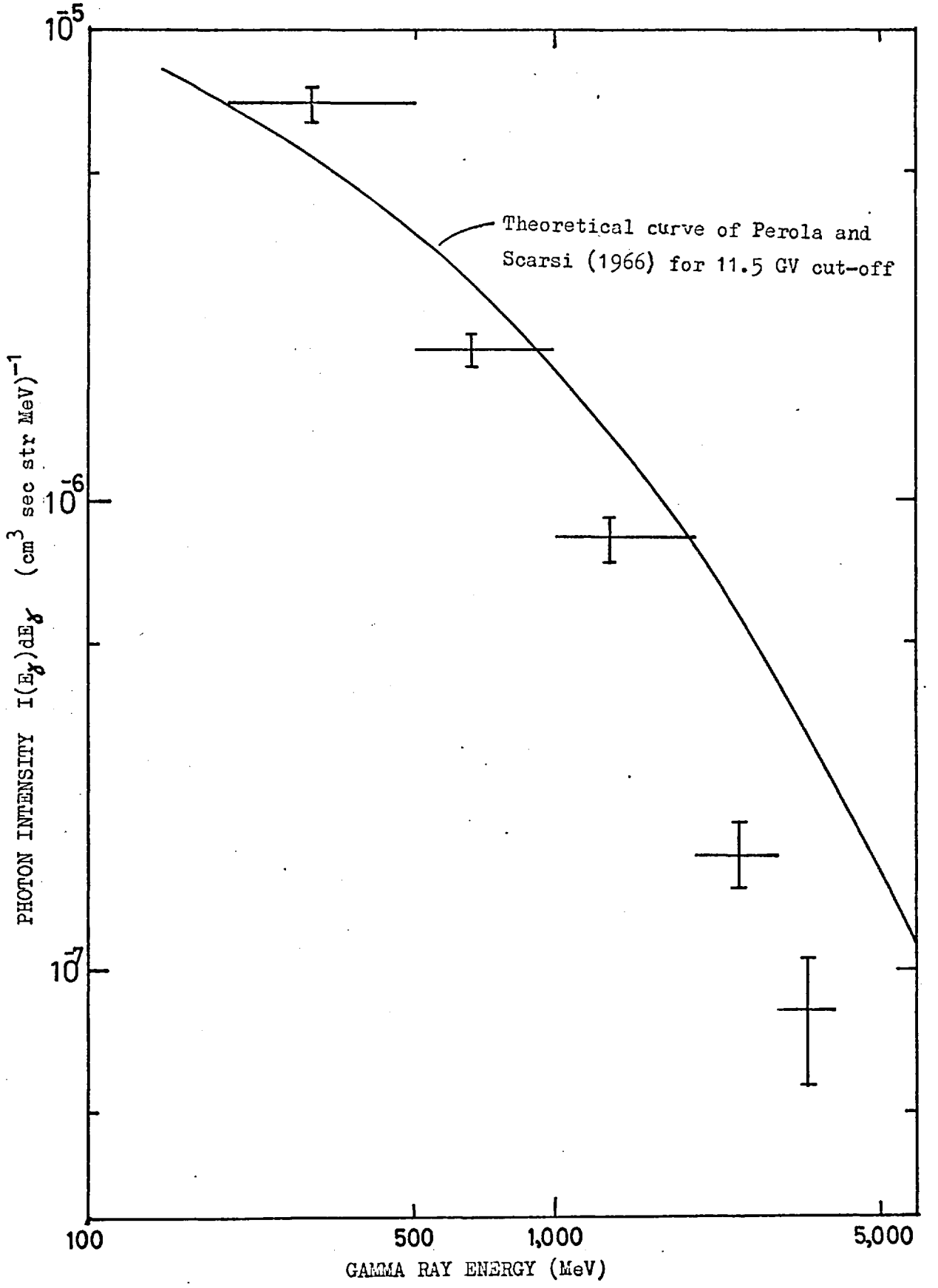


Figure 3.8 Atmospheric secondary gamma-ray spectrum.

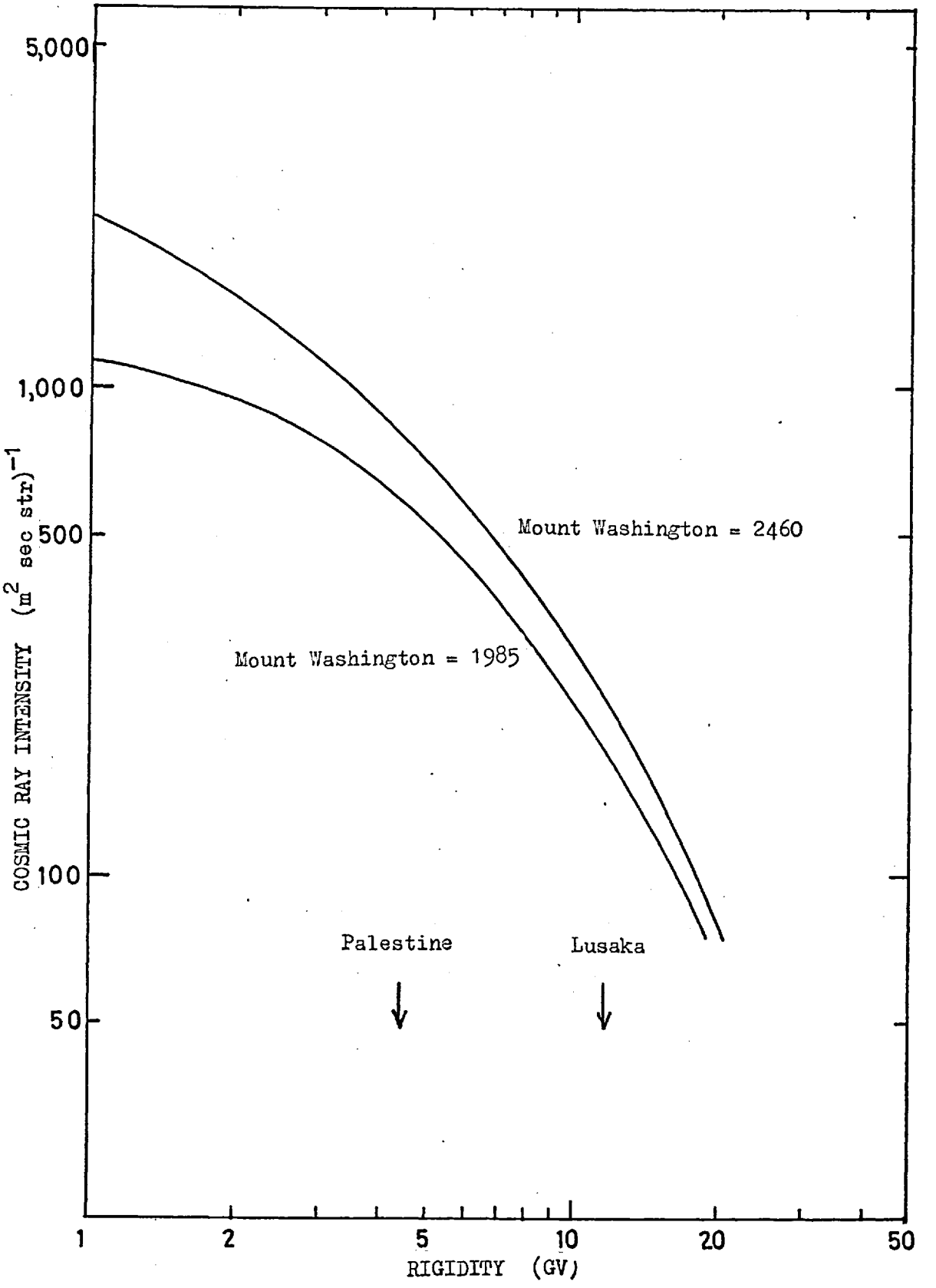


Figure 3.9 Integral rigidity spectrum of the total primary cosmic radiation at sunspot minimum and sunspot maximum (after Webber, 1967).

cosmic ray intensity as a function of geomagnetic rigidity from which it is seen that the primary flux is a factor of 3 less at Lusaka (11.6 GV) than at Palestine (4.5 GV), a popular launch site in the Northern Hemisphere. Perola and Scarsi (1966) calculated that the intensity of π^0 decay gamma-rays in the atmosphere at 200 MeV varied by a factor of 2.5 between the same latitudes (Figure 3.10). In addition at 11.6 GV, solar modulation accounted for 30% variation of the cosmic ray intensity over the large solar modulation cycle depicted in Figure 3.9. However the level of modulation in 1971 was not too different from that in 1966 when most of the results considered were achieved.

In Figure 3.11, the findings of Fazio et al. and Fichtel et al. are plotted, normalized to unit atmospheric depth, and both are from experiments carried out from Palestine. The present results, further normalized to take account of the geomagnetic variation in intensity, are shown and also included are the measurements of Anand et al., made at Hyderabad, India (16 GV cut-off).

Although the Zambia results after the normalization, show a similar spectral shape to the rest, the intensities lie above the average Palestine level.

Frye et al. (1971) reported that the second gamma-ray intensity measured at Parkes, N.S.W. (4.5 GV cut-off), was 1.45 times that measured at Longreach, Queensland (8.8 GV cut-off) when the corresponding ratio of cosmic ray intensity over the same rigidity range was 2.2. Furthermore the curves of Perola and Scarsi predicted a ratio of 2.5 in the gamma-ray intensities at 100 MeV. In view of Frye's results it would appear that normalization of the fluxes measured at different

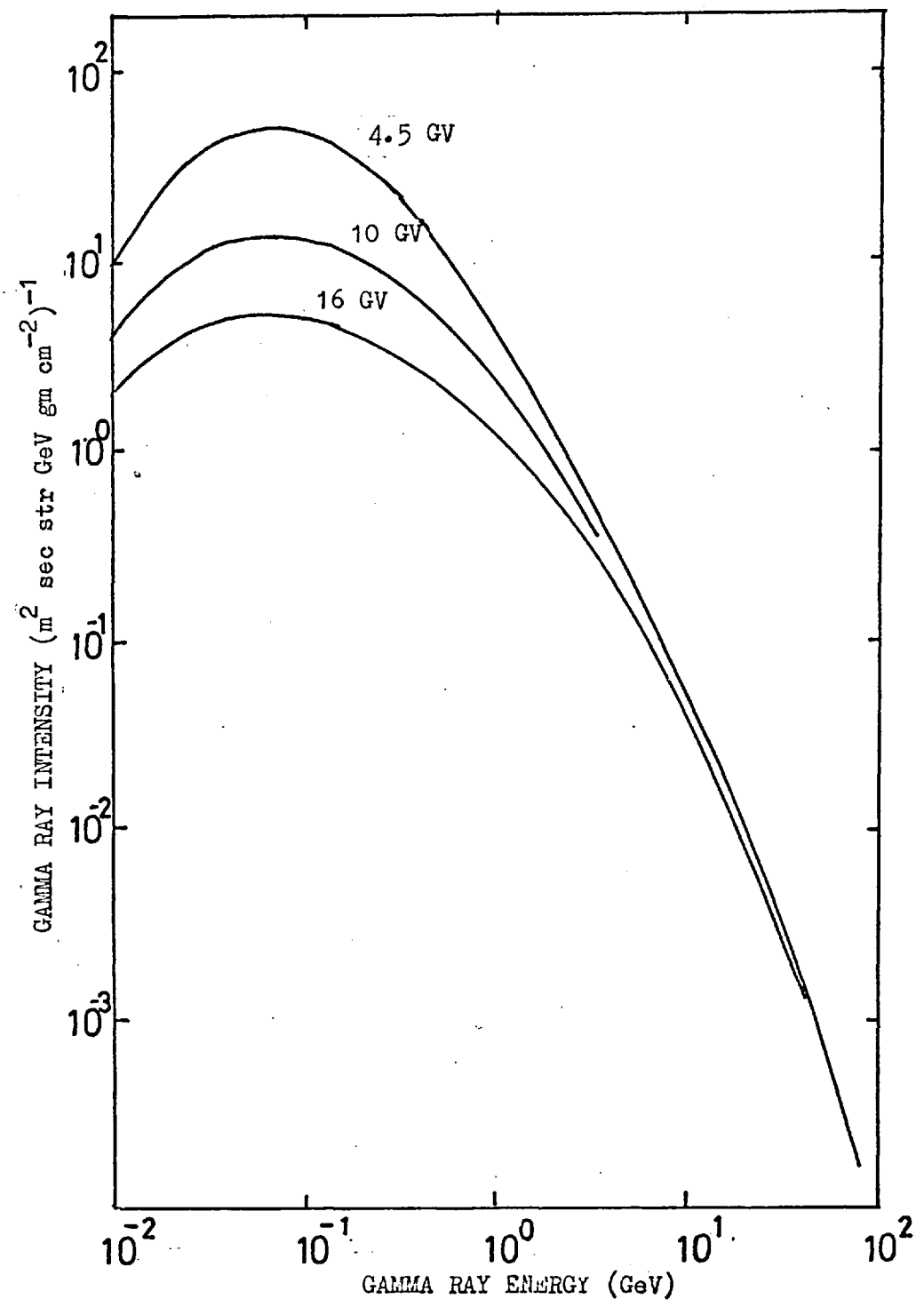


Figure 3.10 Calculated intensity of secondary gamma-rays at various cut-off rigidities (after Perola and Scarsi, 1966).

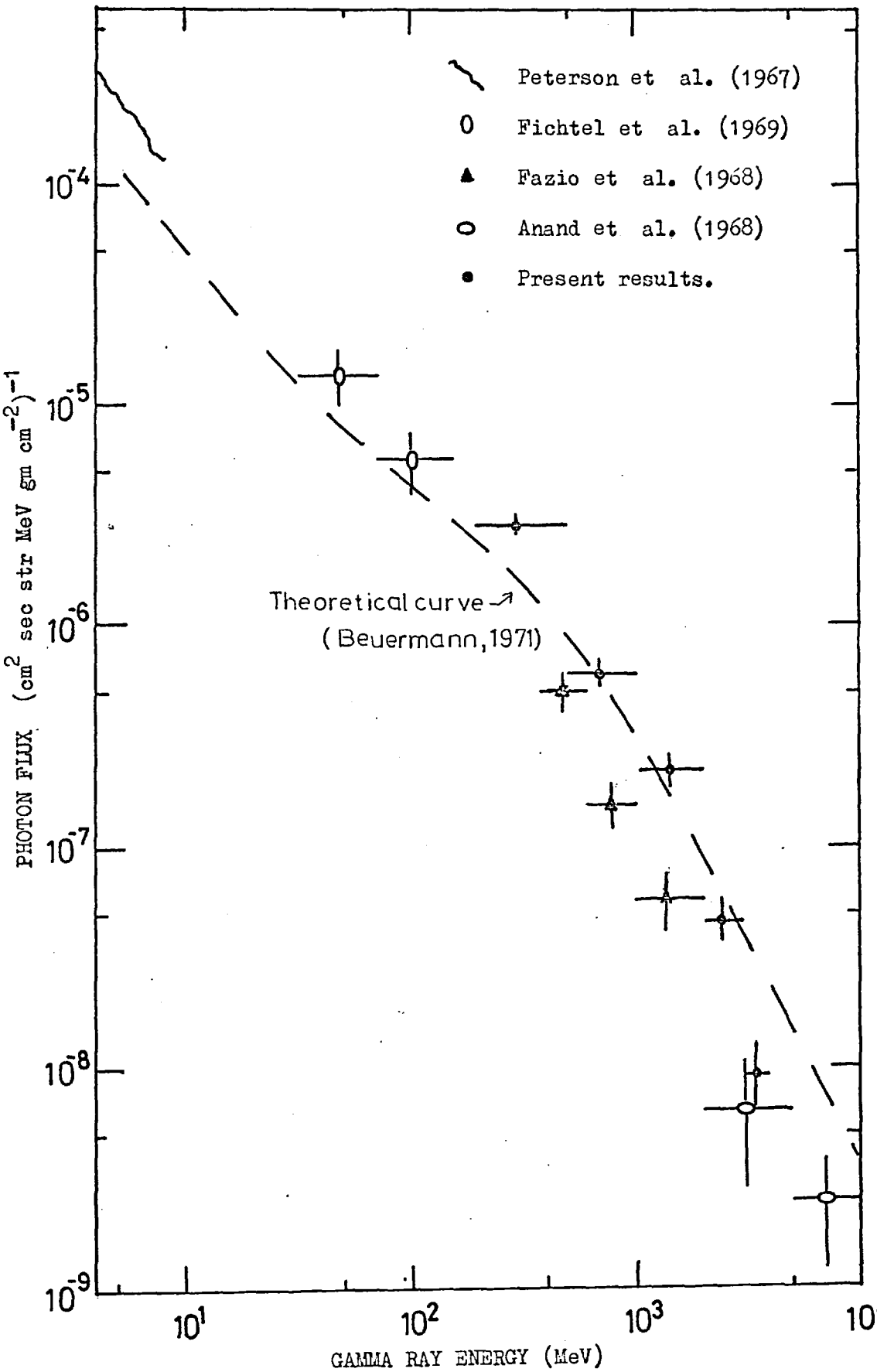


Figure 3.11 Atmospheric photons at 4.5 GV cut-off.

geomagnetic latitudes by the factor relating either the cosmic ray intensities or the predicted secondary gamma-ray fluxes of Perola and Scarsi at the different latitudes is suspect. For this reason no significance was given to the fact that the normalized Zambian flux values were higher than the average Palestine level but the excellent agreement between the spectral form indicated that the detector had been correctly calibrated and had functioned well in flight.

CHAPTER IV

SEARCH FOR GAMMA RAY SOURCES

4.1 Determination of the Gamma-Ray Arrival Direction

The arrival direction of the incident photon in the spark chamber frame of reference was deduced from the co-ordinates of the spark in each plane. For a double track event the median, which approximated to the bisector, was taken to represent the incident photon trajectory. To calculate the extrapolated arrival direction on the celestial sphere, successive transformations were performed upon the direction cosines of the track, or bisector, (CX, CY, CZ). The first transformation gave the inclination in geomagnetic co-ordinates, where the angle between the spark chamber x axis and the horizontal field vector was ψ degrees, calculated from the magnetometer readings. Thus:

$$\begin{pmatrix} CX_1 \\ CY_1 \\ CZ_1 \end{pmatrix} = \begin{pmatrix} \cos\psi & \sin\psi & 0 \\ -\sin\psi & \cos\psi & 0 \\ 0 & 0 & 1 \end{pmatrix} \begin{pmatrix} CX \\ CY \\ CZ \end{pmatrix}$$

Considering the geographic position of the detector the magnetic declination δ was computed according to the I.G.R.F. magnetic field model enabling the track inclination to be then transformed into the geographic frame

$$\begin{pmatrix} CX_2 \\ CY_2 \\ CZ_2 \end{pmatrix} = \begin{pmatrix} \cos\delta & \sin\delta & 0 \\ -\sin\delta & \cos\delta & 0 \\ 0 & 0 & 1 \end{pmatrix} \begin{pmatrix} CX_1 \\ CY_1 \\ CZ_1 \end{pmatrix}$$

δ = angle of declination

Transforming into siderial co-ordinates, the latitude and longitude of the detector was considered as well as the local time of occurrence of the event.

λ = Co-latitude of detector

and σ = angle from the true equinox

σ was calculated thus:

T_σ = Time in minutes from the true equinox

$$= \underbrace{T_z - 120}_{\text{Universal time of event}} + \underbrace{\frac{(N_0 \times 24 \times 9.8296)}{60}}_{\text{Time from true equinox}} \text{ min}$$

N_0 = number (and fraction) of days since the true equinox

$$\sigma = \frac{T_\sigma \times 15}{60} + \text{LONG. degrees}$$

LONG. = longitude of detector

The direction cosines of the track in Siderial co-ordinates were given by:

$$\begin{pmatrix} CX_3 \\ CY_3 \\ CZ_3 \end{pmatrix} = \begin{pmatrix} 1 & 0 & 0 \\ 0 & \cos\sigma & \sin\sigma \\ 0 & -\sin\sigma & \cos\sigma \end{pmatrix} \begin{pmatrix} \cos\lambda & 0 & -\sin\lambda \\ 0 & 1 & 0 \\ \sin\lambda & 0 & \cos\lambda \end{pmatrix} \begin{pmatrix} CX_2 \\ CY_2 \\ CZ_2 \end{pmatrix}$$

Transformation into the galactic system of co-ordinates was performed by a two fold rotation in which α_N and δ_N defined the position of the galactic North pole in the celestial sphere and a further rotation through γ deg. about x axis which pointed the new z axis towards $l^{II} = 0$, $b^{II} = 0$, the galactic centre. (Figure 4.1)

According to the I.A.U. system of Galactic Co-ordinates (1959)

$\alpha_N = 192.5^\circ$

$\delta_N = 27.4^\circ$

and $\gamma = 57.5^\circ$

$$\begin{pmatrix} CX_4 \\ CY_4 \\ CZ_4 \end{pmatrix} = \begin{pmatrix} 1 & 0 & 0 \\ 0 & \cos\gamma & \sin\gamma \\ 0 & -\sin\gamma & \cos\gamma \end{pmatrix} \begin{pmatrix} \sin\delta_N & 0 & \cos\delta_N \\ 0 & 1 & 0 \\ -\cos\delta_N & 0 & \sin\delta_N \end{pmatrix} \begin{pmatrix} 1 & 0 & 0 \\ 0 & \cos\alpha_N & \sin\alpha_N \\ 0 & -\sin\alpha_N & \cos\alpha_N \end{pmatrix} \begin{pmatrix} CX_3 \\ CY_3 \\ CZ_3 \end{pmatrix}$$

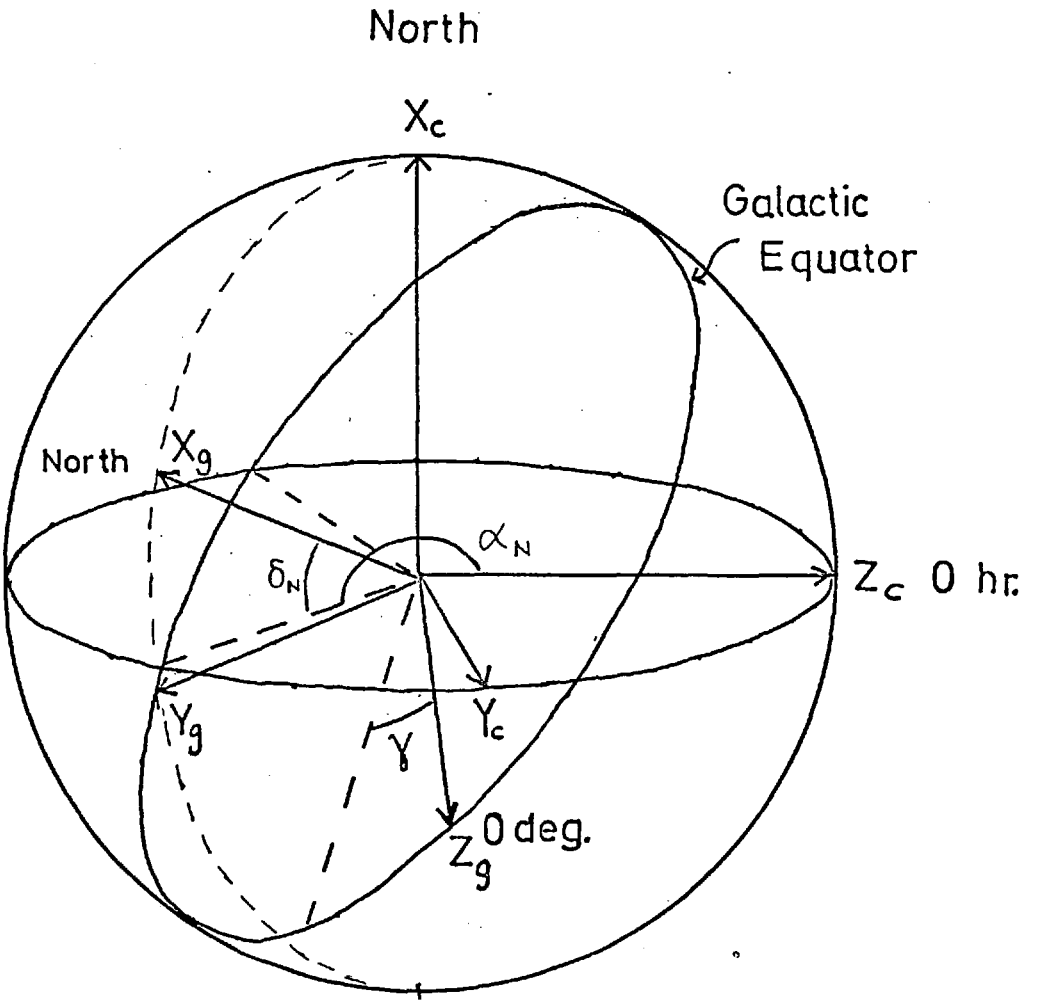


Figure 4.1 Projection of galactic co-ordinate system on the celestial sphere, showing transformation angles.

The galactic latitude and longitude (or right ascension or declination if in the Siderial frame) of the extrapolated arrival direction were computed from the direction cosines.

The area of sky which was surveyed during the flights was divided into an array of bins which were 2 deg. long parallel to the galactic or celestial equator and whose width varied such that the bins subtended the same solid angle as a 2 degree x 2 degree bin located at the equator.

Having computed the extrapolated directions of the incident photons, summary plots of these directions were created in the 2 x 2 degree bin array, and these plots were inspected for evidence of emission or clustering of events, above the constant atmospheric background contribution.

4.2 Angular Resolution of the Detector

The angular resolution, i.e., the likely error in the measurement of the gamma-ray direction, resulted from several factors and limited the minimum observable source dimensions and source strength. The errors arose from uncertainties in the orientation of the payload, the limited spatial resolution of the track in the spark chamber and scattering of the secondary electron and positron in the lead converter.

(a) Spark Chamber Spatial Resolution

From Section 2.4.1 it was seen that the angular resolution of a single track was $\pm 1^{\circ}$ and was $\pm 1.5^{\circ}$ for a resolved pair.

(b) Orientation Inaccuracy

The inaccuracies arising in measuring the orientation of the balloon gondola, already discussed in Section 3.5, amounted

to $\pm$ 1° in azimuth.

(c) Scattering in the Converter

The secondary electron and positron which emerged from the lead converter had, in general, inclinations different from that of the parent photon and from each other.

One effect, described in detail by Olsen (1963), concerned the transfer of momentum with a neighbouring nucleus during the pair production interaction, resulting in the electron and positron proceeding with an opening angle θ. On average, θ was related to the photon energy E_γ by:

$$\theta = \frac{1.6}{E_\gamma (\text{MeV})} \quad \text{radians}$$

(Claverie et al., 1971),

when an electron and positron shared the photon energy equally.

For a 200 MeV photon, θ was $\sim\frac{1}{2}$ deg., so the angular error in the bisector of $\frac{1}{4}$ deg. was small compared with the spark chamber and orientation inaccuracies ((a) and (b)).

Multiple Coulomb Scattering

Divergence of the trajectories of the electron and positron from the photon's incident direction arose from multiple Coulomb scattering in the lead traversed after materialization. This process was the dominant factor in the loss of angular resolution of the detector.

Bethe and Ashkin (1953) gave a formula which estimated the R.M.S. angle through which a particle of unit charge momentum p and velocity v, was scattered in a material of depth t gm cm^{-2} and mass number A and atomic number Z:

$$\langle\theta\rangle^{\frac{1}{2}} = \frac{t\ Z\ (Z+1)\ \log F}{Ap^2v^2}$$

where $F = (1.13 \times 10^4\ Z^{4/3}\ A^{-1}\ t)$

$= 19.5 \times 10^3 \times t$ for lead.

The R.M.S. scattering angle arises from multiple, small scatter, Coulomb interactions and does not include plural scattering (infrequent large scattering). The comparison of the predicted angles with those measured in practice is excellent (Snyder and Scott, 1949; Hanson et al., 1951) for angles $\lesssim \theta$ R.M.S.

The curves of Figure 4.2 a show how the estimated scattering angles for $\frac{1}{4}$ r.l. and $\frac{1}{2}$ r.l. of lead vary with energy, indicating that the degree of scattering of the electrons was greatly dependent upon the depth at which the gamma-ray interacted in the converter. By considering the probability of pair production at a particular depth in the lead, there was, for $\frac{1}{2}$ r.l., approximately an equal number of gamma-ray interactions in each equal depth interval. By evaluating the scattering angle distributions of 100 MeV electrons produced at these variable depths, the effective distribution of scattering angles was derived. The curve, which is designated 'real',is shown in Figure 4.2b In comparison with the $\frac{1}{4}$ r.l. scatterer it was seen that the peaks appeared at approximately the same angle, although the long tail in the 'real' curve reduced its relative amplitude, the curves being normalized. However, it was a reasonable approximation to assume that all electrons formed in the lead were scattered by $\frac{1}{4}$ radiation length.

If the energy of 200 MeV photon was shared equally by the electron and positron then the R.M.S. scattering angle for

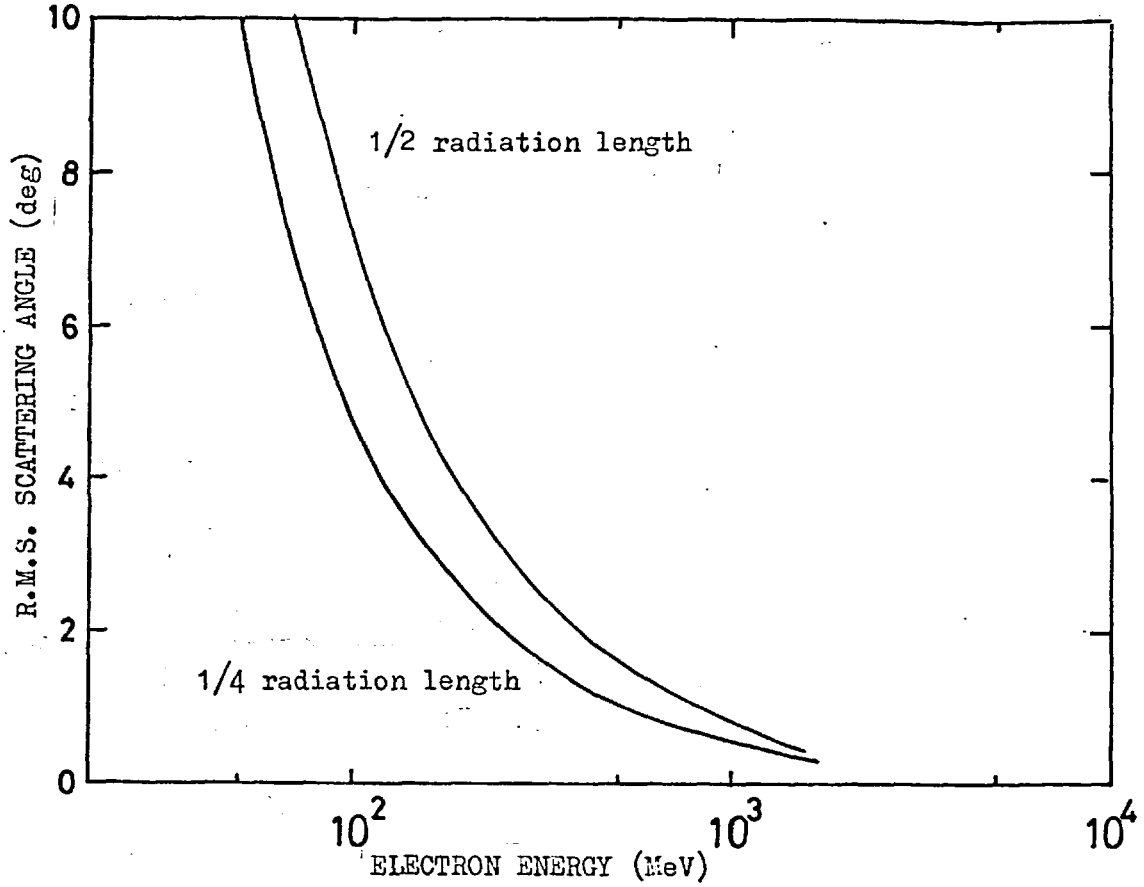


Figure 4.2a R.M.S. scattering angle for electrons in $\frac{1}{4}$ r.l. and $\frac{1}{2}$ r.l. of lead as a function of energy.

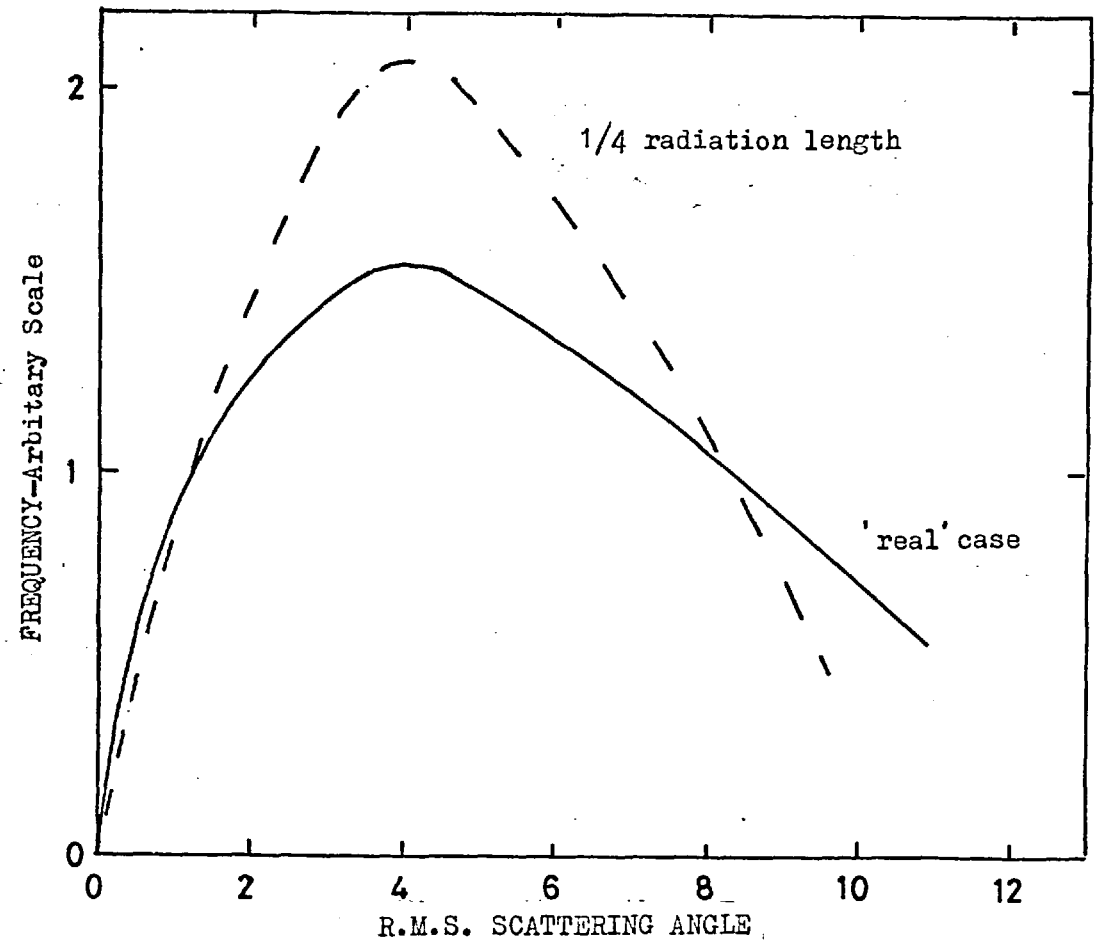


Figure 4.2b Distribution of scattering angles for 100 MeV electrons created $\frac{1}{2}$ way through converter and at all depths in the $\frac{1}{2}$ r.l. converter.

each was ~5°. The bisector of the prongs, if the pair was resolved by the spark chamber, defined the photon arrival direction and it was necessary to estimate the average angular inaccuracy arising from this assumption. In fact, the bisector for the 200 MeV case represented the photon arrival direction to within 3° in 50% of the cases, both prongs having scattered independently by ~5°.

This naive model was improved when account was taken of the partition of the photon energy between the electron and positron as given by Rossi and Greisen (1941). Their results presented in the form of normalized curves are illustrated in Figure 4.3 where $E\ \Phi_{pair}$ is plotted as a function of the fractional energy of one of the products,

E = photon energy (MeV)

E' = energy of electron or positron

Φ_{pair} = differential pair production probability per radiation length

and $v = \dfrac{E' + m_e c^2}{E}$ = fraction of photon energy

The average energies of the low and high energy members of the pair were deduced from the curves of Rossi and Geisen since

$$\bar{E}_{low} = \frac{\int_0^{E/2} \Phi_{pair}(E, E').E'.dE'}{\int_0^{E/2} \Phi_{pair}(E, E').dE'}$$

thus

$$\bar{v}_{low} = \frac{\int_0^{1/2} E\Phi_{pair}(v).v.dv}{\int_0^{1/2} \Phi_{pair}(v).dv}$$

The integration was carried out numerically for the curves of several energies and the indication was that on average one particle carried off only 25% of the photon's energy at 200 MeV, reducing to 20% at 5 GeV (Table 4.1).

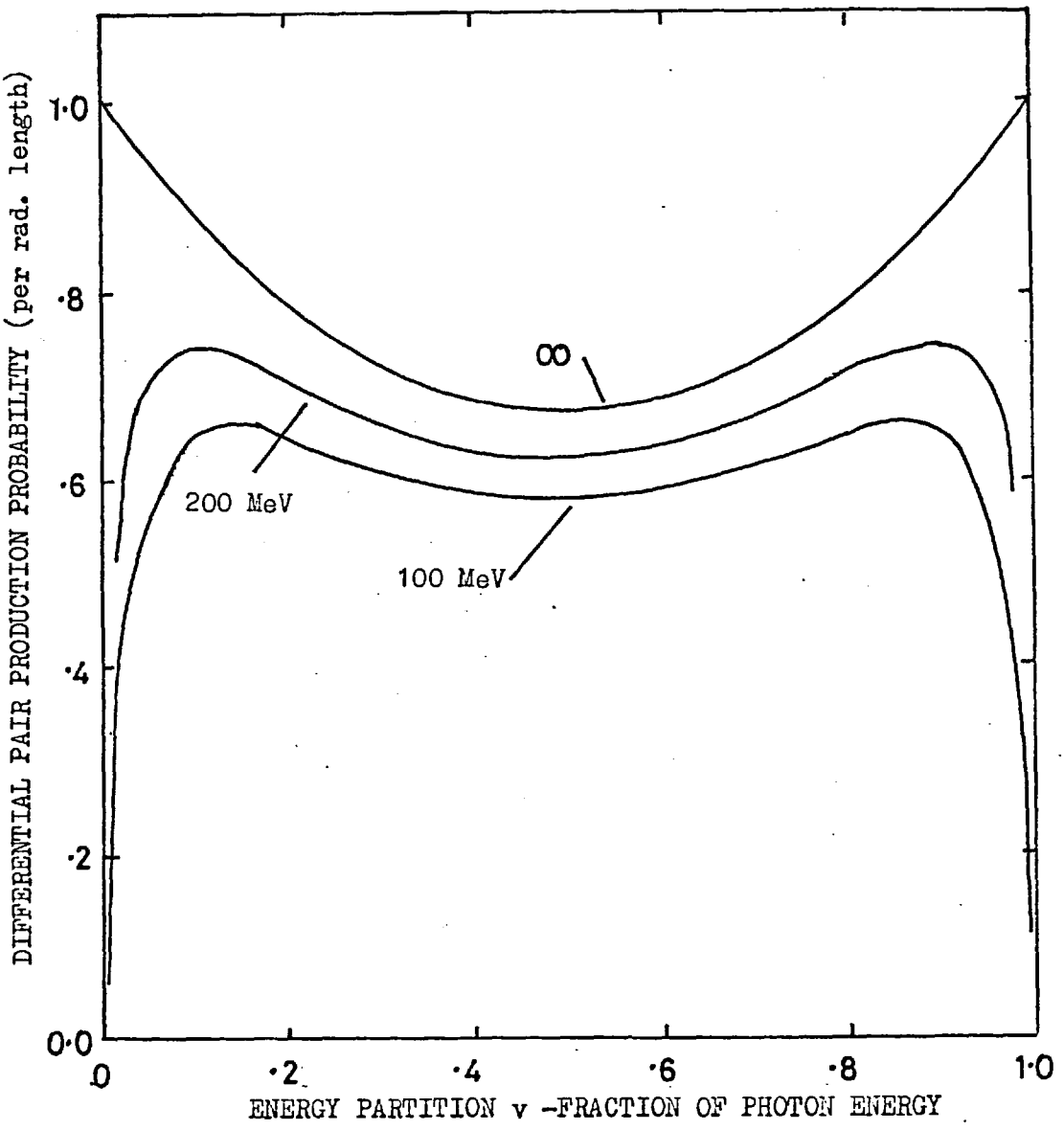


Figure 4.3 Differential probability of pair production per r.l. of lead for photons of various energies. Abscissa $v = (E' + m_e c^2) / E$, ordinate $= E\phi_{pair}(E,E')$ (after Rossi and Greisen, 1941).

Photon Energy	Average Energy of Low Energy Product	R.M.S. Scattering Angle for $\frac{1}{4}$ r.l. Pb		Estimated Error in Photon Direction measurement (50% prob.)
		Low Energy	High Energy	
200 MeV	50 MeV	10.0°	3.0°	6.0°
400 MeV	100 MeV	5.0°	2.0°	3.0°
500 MeV	125 MeV	4.0°	1.0°	2.5°
1 GeV	200 MeV	2.5°	0.75°	2.0°
5 GeV	1 GeV	0.5°	$< 0.5^{\circ}$	$< 1.0^{\circ}$

TABLE 4.1

This meant that the scattering of one electron was small compared with that of its lower energy partner (Figure 4.1a) to which the loss of angular information was mainly due.

In some cases the low energy electron would have been absorbed by the lead, or scattered to such a degree that it did not cross the spark chamber. The single track of the other electron in the spark chamber, however, would have undergone only a small amount of scattering and therefore represented the photon's incident direction with high precision. Also its energy would be $\sim 75\%$ of that of the photon, the loss of energy being comparable with the energy resolution of the detector. These single track events were included with unresolved pairs in the analysis.

The detector counted events in which the low energy, highly scattered electron alone entered the telescope geometry but it was unlikely that these events would be included in the

analysis. The higher energy electron was not detected by the Cerenkov counter, so the lower energy electron would have produced a small pulse height indicating an energy of less than 200 MeV. These events were discarded.

The acceptance cone of the detector was increased because of scattering but because the low energy single events were discriminated against by the Cerenkov counter, the increase in opening angle for gamma-rays was approximately equal to the R.M.S. scattering angle of the higher energy electrons.

Table 4.1 lists the estimated error in measuring the photon direction due to multiple Coulomb scattering. The overall resolution due to the combined effects of (a), (b) and (c) is plotted as a function of photon energy in Figure 4.4.

4.3 Detector Sensitivity to Point Sources

The minimum observable source strength was limited by the amount of time that the detector viewed the particular area of sky. The way in which the area presented to the source region varied as it crossed the field of view of the detector is illustrated in Figure 4.5, for an on-axis transit and 10 deg. and 20 deg. off-axis transits.

The approximate triangular profile meant that the maximum area-time factor, which gave the highest sensitivity, was simply $A \times T_{max}/2$, where A is the area of the detector and T_{max} the time taken for a point on the celestial sphere to cross the field of view. For a $\pm 38^{\circ}$ half opening angle $T_{max} \sim 5$ hours.

The calculation was less simple for off-axis transits, especially when motion of the detector was taken into account, and the exposures were evaluated numerically by computer. For

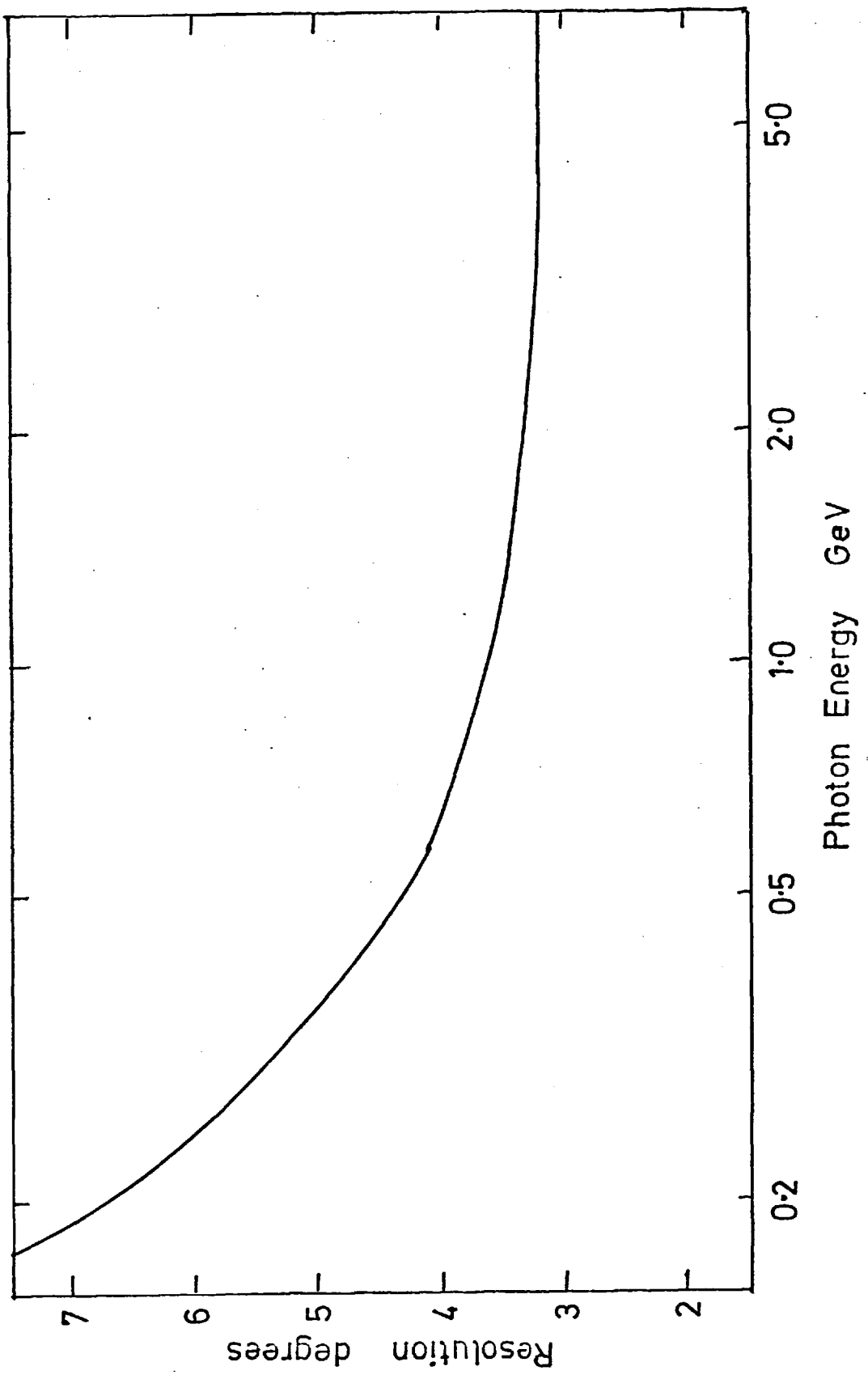


Figure 4.4 Angular resolution of the detector plotted as a function of gamma-ray energy.

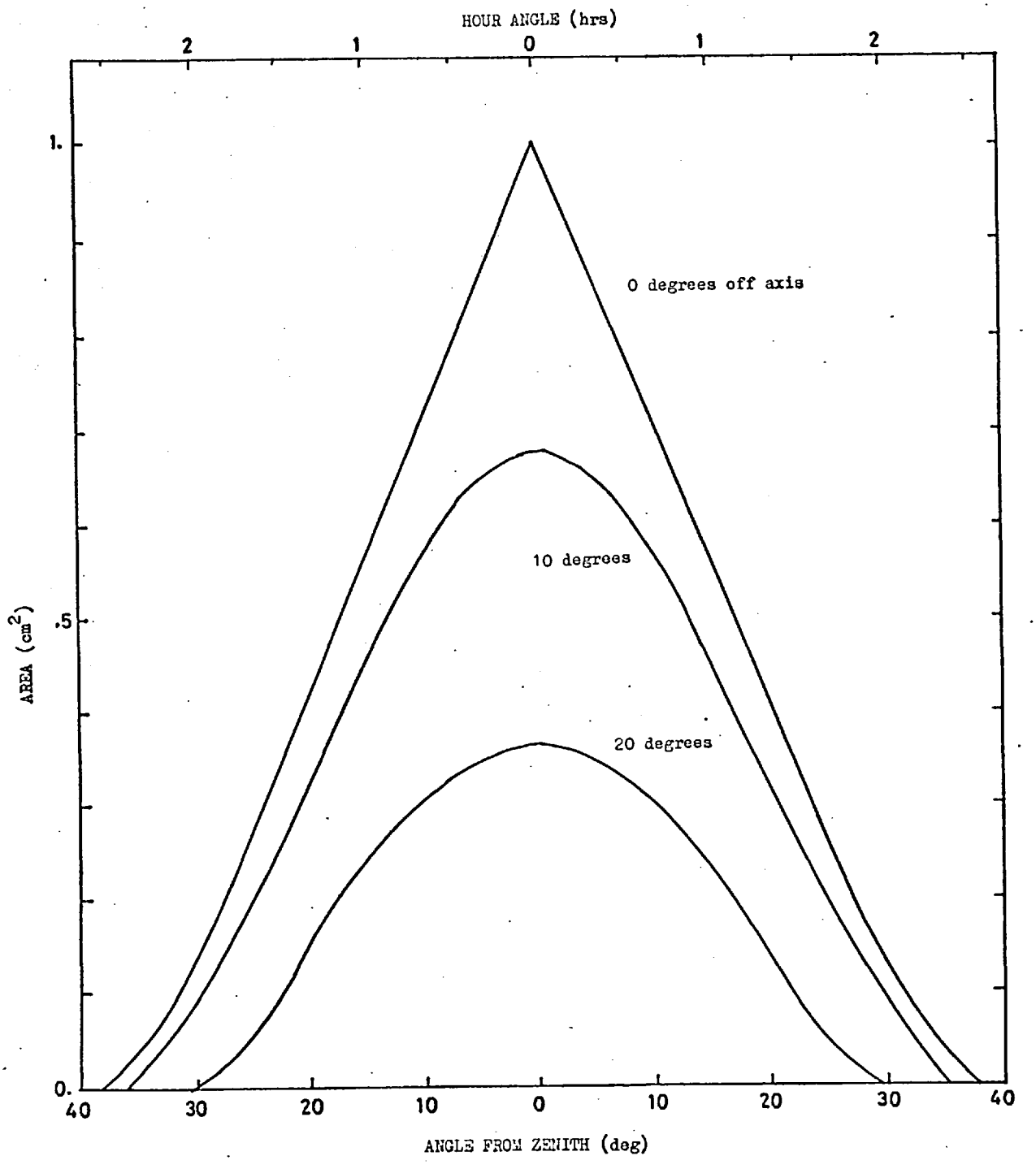


Figure 4.5 Detector area presented to a point source as it transits the Detector ($\pm$ 38^{o} half opening angle).

the general sky survey to be undertaken, the area-time factor for each $2^{\circ} \times 2^{\circ}$ bin in the sky map was calculated.

The vertical axis of the gamma-ray detector traced a line across the sky, described by the approximate equations of motion of the payloads shown in Table 4.2.

The vertical axis, or the pointing direction, of the detector was transformed into the celestial and galactic frame of reference (as described in Section 4.1) giving the flight trajectory across the celestial and galactic sphere.

Taking the mid-point as being representative of each bin the detector area presented to it was calculated for successive $2\frac{1}{2}$ minute intervals (dT) throughout the flight using the formula:

$$\Delta E\,(l'', b'') = L^2 \times \cos\theta \times dT \times \left[\frac{\pi \tan^2\alpha}{4} - \tan\theta\left(\frac{\tan\alpha}{4} - \frac{\tan^2\theta}{4}\right)^{\frac{1}{2}} - \frac{2\tan^2\alpha}{4} \arcsin\left(\tan\theta/\tan\alpha\right)\right] \text{cm}^2 \text{ min.}$$

where α = half opening angle of detector (deg.)

θ = angle between detector vertical axis and vector to l'', b'' (deg.)

L = depth of detector telescope (cm^2)

and For $\theta \leq \alpha$, $\Delta E > 0$

For $\theta > \alpha$, $\Delta E = 0$

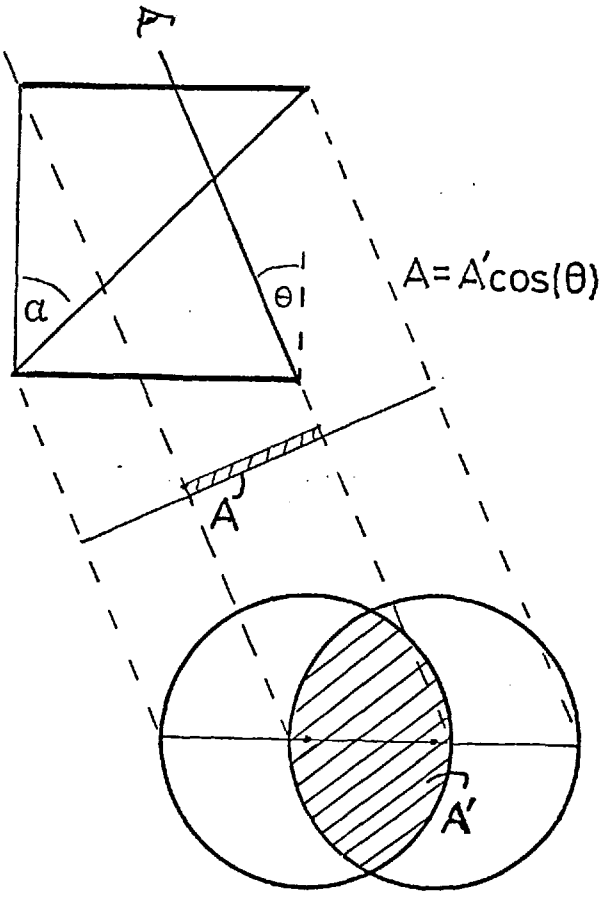
i.e. $\Delta E(l'', b'') = \Delta E(\theta) = A \times dt$

as illustrated by the following diagram.

Equations Describing Flight Trajectory	
Flight 1	
LAT (T) = 15.31 + T x 0.004	deg South
LONG (T) = 27.90 - T x 0.026	deg East T < 30 min
LONG (T) = 27.13 - T x 0.022	deg East T > 30 min
Flight 2	
LAT (T) = 15.17 - 0.004 x T	
LONG (T) = 27.65 - 0.015 x T	

T = Time after reaching ceiling in minutes

TABLE 4.2



In this manner the exposure for each 2^{o} x 2^{o} bin in the sky map was evaluated for the entire flight and this information was stored by the computer in the form of an array on magnetic tape. The results are best illustrated by the smoothed exposure contours in Figure 4.6 which indicate the region of the galaxy scanned during Flight 1.

The background counting rate, angular resolution and exposure limited the sensitivity of the gamma-ray detectors according to the formula :

$$I_m = S_m \left(\frac{\Phi}{\varepsilon} \cdot \frac{wf}{AT} \right)^{\frac{1}{2}} \qquad (cm^2\ sec)^{-1}$$

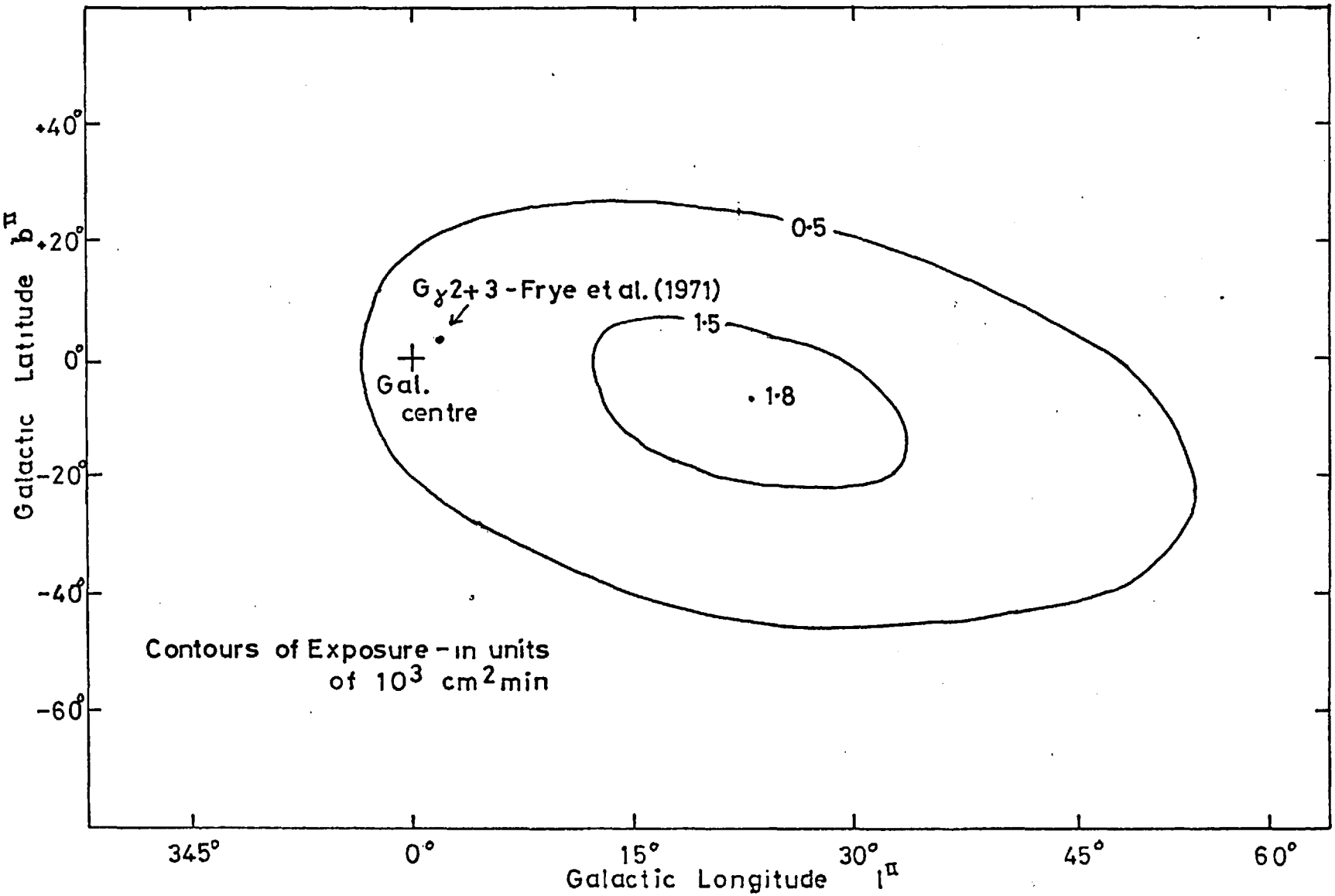


Figure 4.6 Region of galaxy scanned during Flight 1.

where the symbols are those already explained in Section 2.1.

S_m, the signal to noise ratio, should be at least 3 in order to be 99% confident that the observed excess is not due to fluctuations in the background intensity (assuming Gaussian statistics). The sensitivity of the detector, in the case of a complete transit of a point source across the detector axis was $\sim 9 \times 10^{-5}$ cm^{-2} sec^{-1} ($E_\gamma > 200$ MeV) where the measured background flux (Section 3.6.2) was 2×10^{-3}(cm^2 sec str)$^{-1}$ at 4.3 mb. Combining the results of two equally successful flights of identical detectors at a similar altitude would have improved this figure to 6×10^{-5} cm^{-2} sec^{-1}.

4.4 Point Sources

The sky map of arrival directions of gamma-rays was examined, in conjunction with the corresponding map detailing the exposure for each of the bins, for evidence of gamma-ray emission above the background flux.

The general performance of Flight 2 was inferior to that of Flight 1 and the detection sensitivity suffered correspondingly. In fact, because its average float altitude was 15 mb, the background flux was twice that of Flight 1 (with increased attenuation of the primary gamma-ray signal) and consequently the nominal sensitivity was a factor of two below that of detector 1. It was therefore decided to examine the results of Flight 1 and only include the results of the second flight to corroborate any evidence of emission observed.

Celestial plots of arrival directions were computed at energies greater than 0.2, 0.5, 1.0 and 2.0 GeV and the area of sky encompassed by the one third maximum exposure contour was

inspected for evidence of clustering of gamma-ray events. Adjacent bins in the sky plot were combined in order to make an angular sum approximately equal to the resolving power of the detector at the various energy levels but no significant evidence for point emission was found in the data of Flight 1.

Particular attention was paid to regions containing known hard X-ray sources and other objects of interest including the Sun and Galactic Centre (Sgr A). The number of counts in each angular bin encompassing the region of interest was summed and compared with the number expected from the background contribution, calculated from the flux in the rest of the sky.

n_b = number of bins under consideration

N_B = expected number of counts from the secondary background rate.

$\phi(>E)$ = integral flux of background gamma-rays $cm^{-2}sec^{-1}str^{-1}$

$(AT)_i$ = exposure to i th bin cm^2sec

$\overline{AT} = \sum_{i=1}^{i=n_b} (AT)_i / n_b$

= mean exposure for each bin cm^2sec

$$N_B = n_b \left(\frac{2}{57.3} \right)^2 \times \frac{\phi(>E)}{\overline{AT}} \text{ photons } (cm^2sec)^{-1}$$

Tables 4.3 and 4.4 indicate the counts expected and observed for several well known X-ray sources in the Galactic centre region and the reported gamma-ray source coincident with the X-ray source GX2+3 (Frye et al. 1971).

Since none of the measured fluxes exceeded the values expected from background by any significant margin, upper limits were set to the gamma-ray emission.

The upper bounds which do not include any data from Flight 2, have been calculated using the method of Hearn (1969),

which is particularly useful in evaluating upper limits of source counts when the background flux is small, as at the higher energies. Tables 4.3 and 4.4 give the 95% confidence flux upper limits which were estimated after making allowances for possible attenuation of the gamma-ray signal by the atmosphere and for the energy response of the detector, assuming a π^0 decay spectrum from the source.

4.5 Galactic Line Emission

4.5.1. Treatment of Data

The Galactic plane crossed the field of view of the detector in both flights so it was possible to inspect the data for evidence of gamma-ray emission from the Galactic disc. In Section 3.3.2 it was seen that for Flight 1 at ~19.00 hrs S.T. , the time at which the Galactic plane was overhead the detector, the raw gamma-ray trigger rate had exhibited a maximum. To check the reality of this signal further investigations were carried out as follows:

The sky map gave the distribution of the extrapolated gamma-ray arrival directions in $2^\circ \times 2^\circ$ bins in Galactic co-ordinates so bins running parallel to the Galactic equator were joined to form strips approximately 2° wide.

For the sky plot of >200 MeV gamma-rays the number of events in each strip was summed and, starting from the Galactic centre, the strips were combined to give a total strip width which was comparable with the angular resolution of the detector.

From the corresponding exposure map, which indicated the area of detector presented to each $2^\circ \times 2^\circ$ bin during the flight, the mean exposure to each strip was calculated.

Object	Energy GeV	Angular Bin Size (Cone Width) (approx)	Counts Observed	Counts Expected	95% Upper Limit Source Count	Mean Exposure to Bin cm^2 min	$F_{95} \times 10^{-5}$ cm^{-2} sec^{-1}
GX 17 + 2	0.2	7°	41	37	14	1.6	9.7
(SER XR2)	0.5	4°	8	9.0	7.0		4.7
	1.0	4°	6	4.6	7.5		5.2
	2.0	4°	3	0.8	7.0		4.7
SUN	0.2	7°	18	26	8.0	1.103	8.0
	0.5	4°	5	6	6		6.0

TABLE 4.3

Object	Energy GeV	Angular Bin Size (Cone width) (approx)	Counts Observed	Counts Expected	95% Upper Limit Source Count	Mean Exposure to Bin cm^2 min	$F_{95} \times 10^{-5}$ cm^{-2} sec^{-1}
SUN (contd)	1.0	4°	2	3	4.5	1.103	4.5
	2.0	4°	0	0.5	3.0		3.0
GX 13 + 1	0.2	7°	48	36	14	1.24	12.0
(SGR XR2)	0.5	4°	17	14	12		10.5
	1.0	4°	8	5.6	9.3		8.2
	2.0	4°	2	0.5	5.7		5.0

TABLE 4.3 (continued)

Object	Energy GeV	Angular Bin Size (Cone Width) (approx)	Counts Observed	Counts Expected	95% Upper Limit Source Count	Mean Exposure to Bin cm^2 min	$F_{95} \times 10^{-5}$ cm^{-2} sec^{-1}
OPH XR1	0.2	7°	34	34	14	1.24	12.4
	0.5	5°	5	8.8	5		4.5
	1.0	5°	1	4.5	3.5		3.1
	2.0	5°	0	0.72	3		2.7
Gγ 2 + 3	0.2	7°	29	27	13	1.15	12.5
(Frye et al. 1971)	0.5	4°	5	7	5.5		5.3

TABLE 4.4

Object	Energy GeV	Angular Bin Size (Cone Width) (approx)	Counts Observed	Counts Expected	95% Upper Limit Source Count	Mean Exposure to Bin cm^2 min	$F_{95} \times 10^{-5}$ cm^{-2} sec^{-1}
G X 2 + 3 (contd)	1.0	4^o	2	3	4.5	1.15	4.3
	2.0	4^o	0	0.5	3.0		2.9
GX 3 + 1	0.2	7^o	29	26	12	1.14	11.5
(SGR XR1)	0.5	4^o	6	6	6.7		6.4
	1.0	4^o	4	3	6.5		6.3
	2.0	4^o	1	0.5	4.3		4.1

TABLE 4.4 (continued)

If $(AT)_i$ cm^2 sec was the exposure for the i th bin, and there were n bins in the strip, then the average area-time factor for each strip was simply - $\sum_{i=1}^{i=n} (AT)_i/n$

The number of counts in each strip was the total from all the bins in the strip, so the average flux per bin

$$= \frac{N}{\sum_{i=1}^{i=n} (AT)_i} \times n \times \frac{1}{n}$$

$$= \frac{N}{\sum_{i=1}^{i=n} (AT)_i} \quad \text{cm}^{-2}\text{sec}^{-1}(2^\circ \times 2^\circ \text{ bin})^{-1}$$

The average flux per bin for each strip is plotted in Figure 4.7 where the bin widths at the middle of the plot are approximately equal to the angular resolution, but are wider at higher Galactic latitudes in order to include more counts and reduce the statistical error in the total. The dashed line indicates the mean count rate over the entire sky and since the strips at the Galactic equator exhibited a higher average counting rate than the average value, this was interpreted as possible evidence for line emission. By adding further 2° wide strips either side, the central strip was successively widened by $\pm 2^\circ$ in Galactic latitude. For each increase in the central strip width the number of counts in the rest of the sky was totalled and from the exposure to this region away from the disc, the average background counting rate was calculated. The number of events expected to be counted in the central strip, due to this background flux, was estimated and compared with the number observed.

For each strip width there was an excess number of counts, a maximum signal to noise ratio being obtained when the strip reached $\pm 9^\circ$. Here there was an excess of 33 counts above the 177 expected.

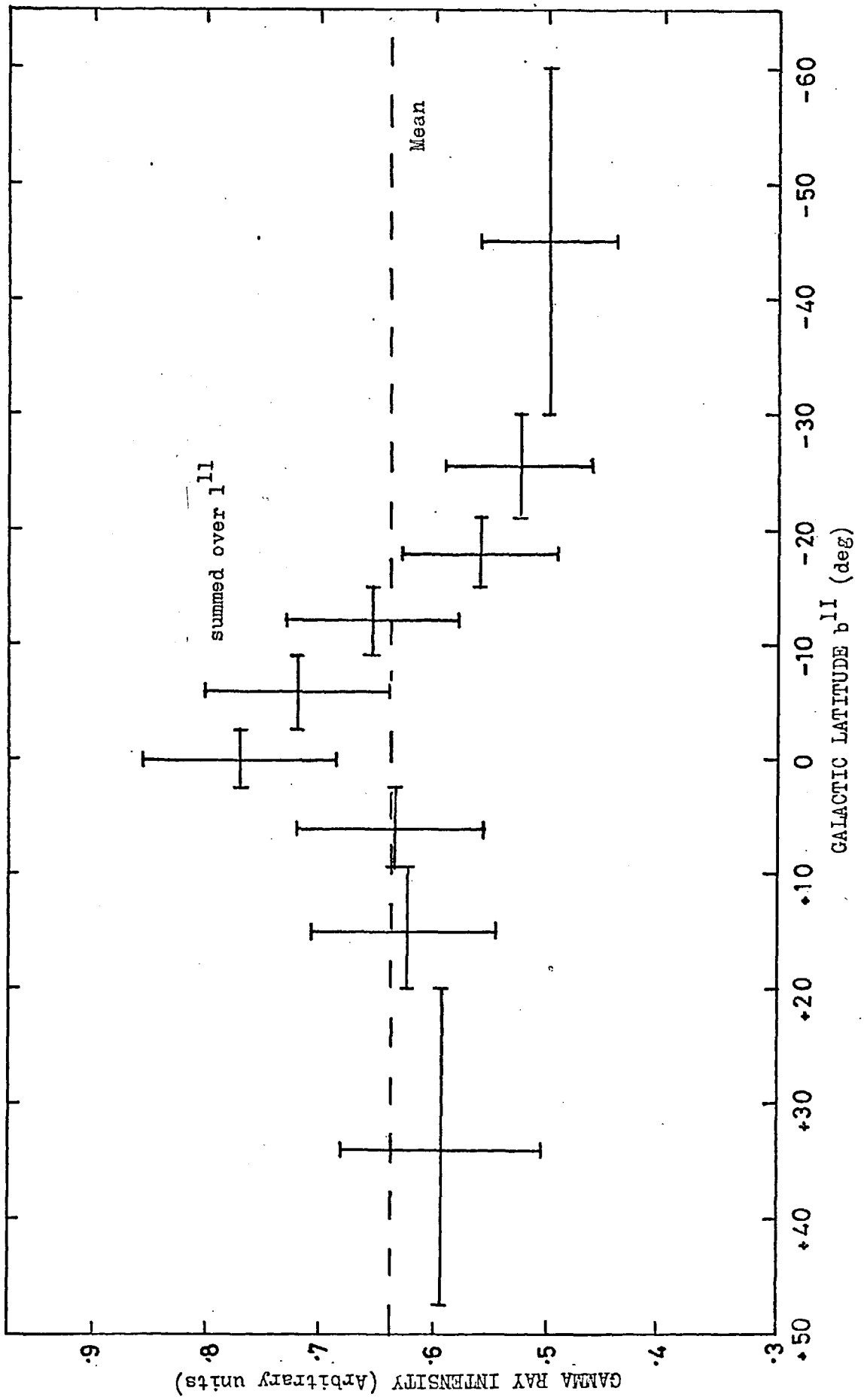


Figure 4.7 The average photon flux for strips summed in galactic longitude ($E_\gamma > 200$ MeV).

The same proceedure was carried out for >1 GeV energy photons, but the maximum excess was only one standard deviation above the expected number (for $\pm 9^{\circ}$).

In order to confirm the existence of the signal in the data and to check its magnitude, the analysis was carried out in another manner. The sky map was again divided into strips in Galactic longitude and the number of events >200 Mev in each $\sim 4^{\circ}$ wide strip plotted as a histogram (Figure 4.8).

A second histogram of the $\sum(A.T)_i$ for each strip was plotted on the same graph. The $\sum(A.T)_i$ axis was normalized so that the two histograms most closely resembled each other, disregarding the central strip which was, in this instance slightly wider ($\mp 10^{\circ}$) for ease of computation. The two histograms were normalized by an iterative process which minimized the residuals (as in a Chi square test) between the two 'curves'.

For each strip $\dfrac{N}{\sum(A.T)_i} = f \equiv$ flux cm^{-2} min^{-1} $(2^{\circ} \times 2^{\circ}\text{bin})^{-1}$

Thus if the curves for N and $\sum A.T$ were normalized $\dfrac{N}{f \times \sum(A.T)_i} \simeq 1$

So f, the normalization factor, measured the average background count rate.

Using this value for f the area-time values, $\sum (A.T)_i$, for the central strips were drawn in on the normalized axis. The number of counts again exceeded the expected background counts and a difference in the areas indicated an excess of 37 counts compared with the 33 counts from the $\pm 9^{\circ}$ disc, confirming the previous conclusions.

As a further check the sky maps were summed in strips of Galactic latitude, excluding the $\pm 10^{\circ}$ central region. The count rates for each strip were again normalized to the area-time factor for each strip and the normalization factor, which

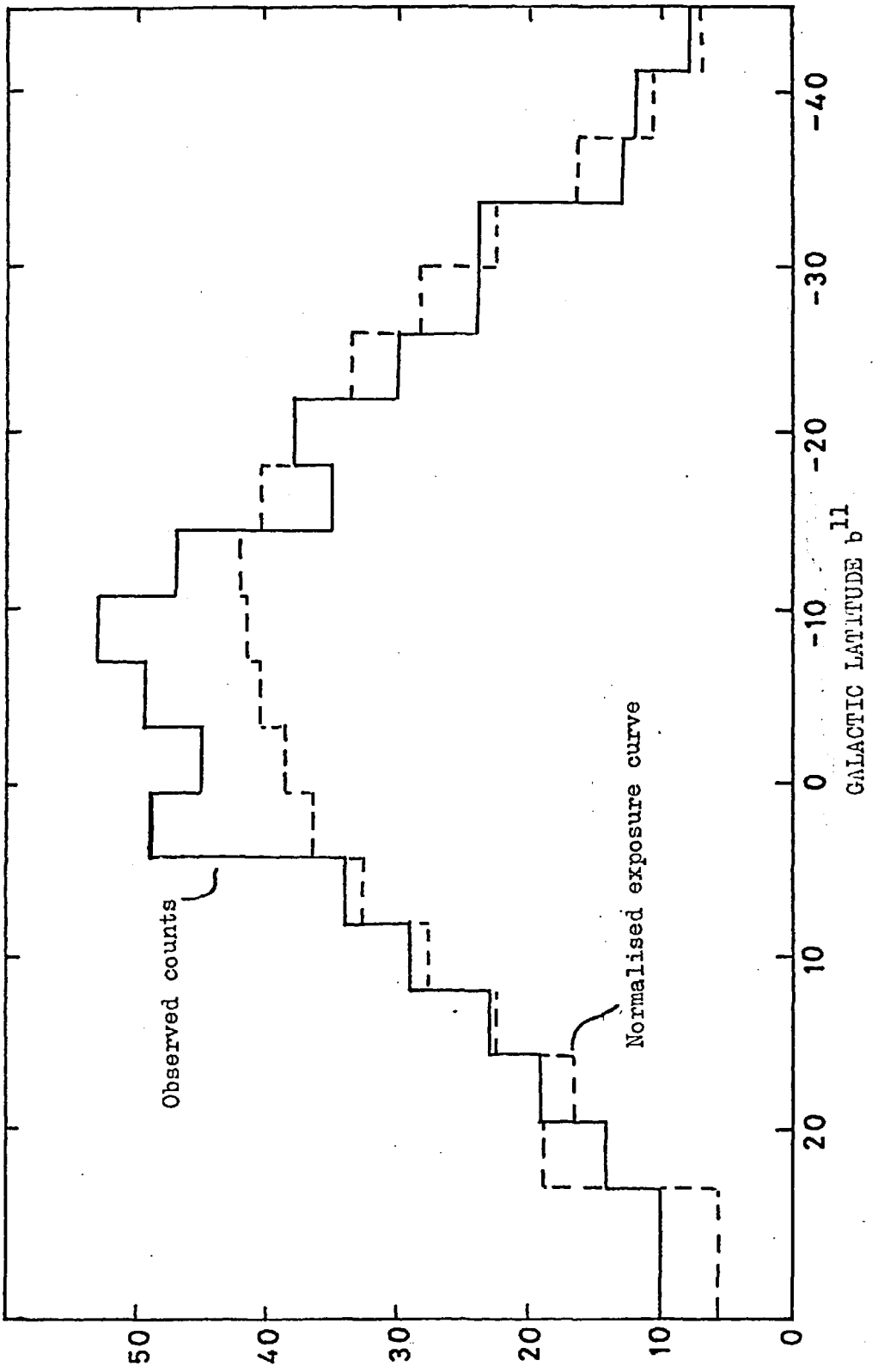


Figure 4.8 The observed number of counts for strips summed in galactic longitude and the number expected from background (depicted by the normalized exposure curve).

indicated the average background rate, agreed with that for the longitude scan (Figure 4.9a).

Finally the longitudinal distribution of events in the disc was compared with the exposure curve, normalized with the factor derived for events out of the disc. The difference in area corresponded to an excess of 37.5 events (Figure 4.9b) and was in agreement with the latitude calculation.

4.5.2 Galactic Line Source Intensity

The central strip in the galactic sky plot that exhibited the most significant excess in gamma-ray counts above background was $\pm 9^{\circ}$ wide. At 200 MeV, the angular resolution of the detector was $\pm 7^{\circ}$ so a narrow equatorial line source would appear at least $\pm 7^{\circ}$ wide. No clustering of the excess counts was observed that could be attributed to point emission within the limits of the detector sensitivity, so the excess was evaluated in terms of line emission.

The line source intensity was calculated as follows:

N = excess number of counts

n = number of bins in the central strip

$\frac{\sum_{i=1}^{i=n}(A.T)_i}{n}$ = average exposure to each bin (cm^2 sec)

Θ_s = half width of strip (degrees)

$\varepsilon(E_\gamma)$ = detection efficiency

$f(t,a)$ = correction for atmospheric absorption and dead time

$g(E_\gamma)$ = energy resolution correction factor

The photon intensity from the central strip is given by

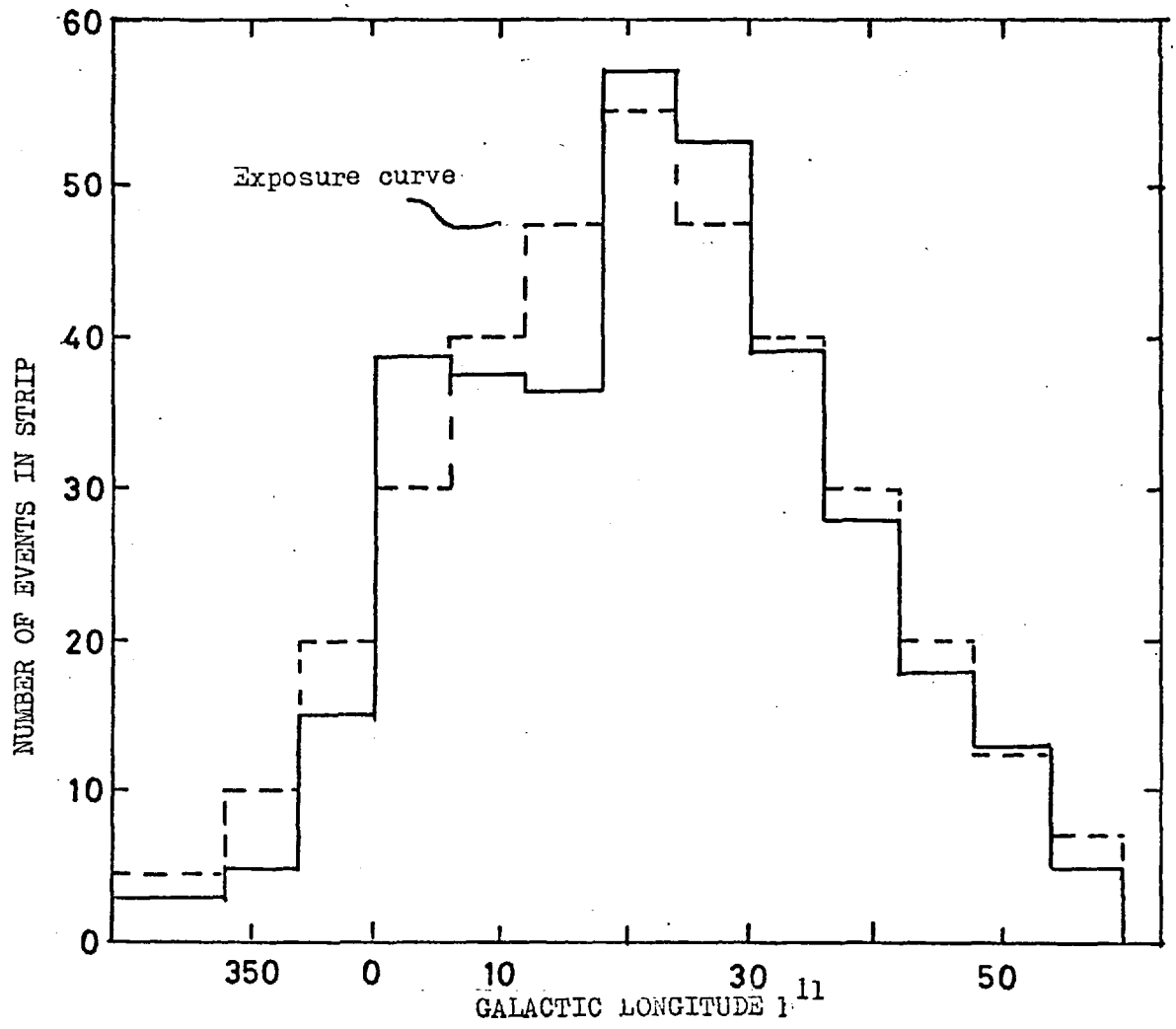


Figure 4.9a The expected and observed gamma-ray counts for strips summed in galactic latitude for the region $|b^{11}| > 10^{\circ}$ ($E_\gamma > 200$ MeV).

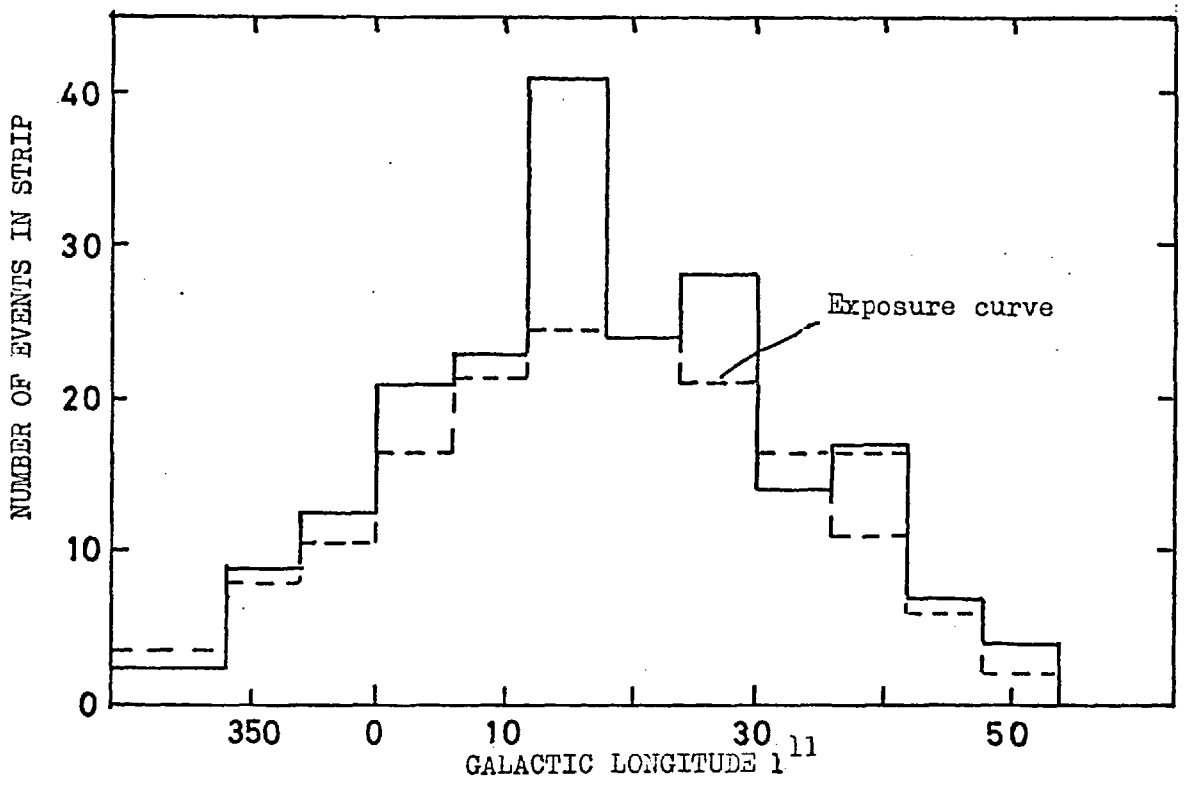


Figure 4.9b The observed count rate for strips in the disc $-10^{\circ} < b^{11} < 10^{\circ}$, compared with the number expected from the background rate seen in Figure 4.9a ($E_\gamma > 200$ MeV).

$$\Phi(E_\gamma) = \frac{N \times n}{\Sigma(A.T)_i \times \varepsilon(E_\gamma)} \times \left(\frac{2}{57.3}\right)^2 \times f(t,a) \times g(E)$$

photons $(cm^2 \text{ sec str})^{-1}$

and the line intensity:

$$\Phi(E_\gamma) = \Phi \times \frac{57.3}{2\theta_s}$$

photons $(cm^2 \text{sec rad})^{-1}$

At 200 MeV the excess of 33 counts yields a line source strength of $(2.8 \pm 1.4)_{\times 10^{-4}}$ photons $(cm^2 \text{ sec rad})^{-1}$. At 1 GeV and 2 GeV no significant excess was observed so upper limits to the line source emission have been calculated. However, as the angular resolution of the detector is $\pm 3.5^\circ$ at these energies a narrower strip was taken and the 95% upper limits indicated in Table 4.5 are for a central strip of width $\pm 5^\circ$.

4.5.3 Flight 2 Results

No comparable excess of gamma-rays was observed in the Galactic scans of Flight 2. This was not surprising since the background flux measured in Flight 2 was twice as intense as that observed during Flight 1. The average difference in altitude between the two flights was equivalent to about 11 gm cm^{-2} of air, for which the gamma-ray absorption length is 40 gm cm^{-2}. The primary signal at this lower altitude was attenuated to 75% of that at 4.3 gm cm^{-2} and in addition, the efficiency for detection of these gamma-rays was, in Flight 2, only 80% of that of Detector 1. This meant that only 55% of the line source gamma-rays counted in Flight 1 would have been detected by Detector 2. In terms of a flux measurement this would only amount to one standard deviation in the background counting rate of Flight 2.

Photon Energy	Counts observed	Counts expected	Line source flux $\times 10^{-4}$ photons/cm^{2}sec.rad.	Width of strip
$\geq$ 200 MeV	210 ± 14.5	177 ± 9	2.8 ± 1.4	$-9^\circ < b^{\prime\prime} < +9^\circ$
$\geq$ 1 GeV	30	25 ± 3	0.82*	$-5^\circ < b^{\prime\prime} < +5^\circ$
$\geq$ 2 GeV	10	8 ± 1.5	0.53*	$-5^\circ < b^{\prime\prime} < +5^\circ$

*95% confidence level upper limit

TABLE 4.5

Gamma-ray counts observed for a galactic line source

in the longitude interval $-20^\circ < l^{\prime\prime} < 50^\circ$

Since the intensity measured during the first flight was only two standard deviations above background and no signal was observed in Flight 2, the observations of Flight 2 were disregarded.

CHAPTER V

DISCUSSION

The observed enhancement in the gamma-ray intensity along the galactic equator is equivalent to a line source intensity of $2.8 \pm 1.4 \times 10^{-4}$ $cm^{2}sec^{-1}rad^{-1}$ for gamma-rays >200 MeV near the galactic centre. Although the statistical significance of the measurements is marginal (95% confidence at the two standard deviation level), considered in the light of the various independent observations carried out in this region of the galaxy, the line intensity interpretation is extremely interesting.

The memorable work of Clark et al. (1971) established that at 100 MeV, the galactic disc emitted gamma radiation at the rate of $\sim 4 \times 10^{-5}$ $cm^{-2}sec^{-1}rad^{-1}$ in the region outside $|l^{II}| < 30^{o}$. In the galactic centre, the intensity was $1.2 \times 10^{-4} cm^{-2}sec^{-1}rad^{-1}$. Subsequent balloon observations at various gamma-ray energy levels have concentrated on the central region. For instance, Fichtel et al. (1972) surveyed the galactic centre and observed a gamma-ray line flux at 100 MeV of 2×10^{-4} $cm^{-2}sec^{-1}rad^{-1}$ (at 4.3 σ above background), in agreement with the results of Clark. However, Frye et al. (1971) merely reported an upper limit of 5×10^{-5} $cm^{-2}sec^{-1}$ rad^{-1} for the region viewed by Fichtel et al.

Despite this contradiction, attempts have been made to account for the line emission observed by Fichtel et al., Clark et al. and Sood (1969a) and these findings are reconcilable with the observation reported here.

The line intensity from the disc in the region of the galaxy $30^{o} < l^{II} < 330^{o}$ can, according to Cavallo and Gould (1971), result from p-p interactions between cosmic-rays and the inter-

stellar hydrogen. The approximate spectral measurements available to Clark et al. indicated that the spectrum of the gamma radiation from the disc resembled that from the earth horizon, which is primarily attributed to π^0 decay. Cavallo and Gould, using new accelerator data on the p-p interaction, calculated a gamma-ray production spectrum which was essentially broader than that calculated previously by Stecker (1970), resulting in a higher value for the gamma-ray production rate S.

From Section 1.2.1.1

$$I_\gamma (> 100 \text{ MeV}) = \int n(r)dr \; S \; f(> 100 \text{ MeV}) \text{ cm}^{-2}\text{sec}^{-1}\text{str}^{-1}$$

So the line intensity measured by a detector of angular resolution $\pm\theta^\circ$ is given by integrating over the latitude interval between $\mp\theta$ (in radians)

$$I_{\gamma \text{ line}}(> 100 \text{ MeV}) = \int_{-\theta}^{\theta} \langle n.L \rangle \; S \; f \; (> 100 \text{ MeV}) db^{II} \quad \text{cm}^{-2}\text{sec}^{-1} \text{ rad}^{-1}$$

Figure 5.1 shows the average line of sight density of neutral hydrogen for 3 angular band widths along the galactic equator, so, substituting the values for S and f (> 100 MeV) from Table 1.1, the expected line intensity is about 4×10^{-5} $\text{cm}^{-2}\text{sec}^{-1}\text{rad}^{-1}$ for a detector of opening angle $\pm 15^\circ$ (OSO 3).

No further convincing corroborating evidence has been presented for the existence of the line intensity in the region away from the galactic centre. Niel et al. (1972) examined the distribution of the recorded gamma-ray events from the Cygnus region as a function of galactic latitude, and deduced that if the observed clustering of events, interpreted as point emission, was disregarded, then the apparent line intensity as seen by a $\pm 15^\circ$ resolution detector would agree with that observed by Clark et al. This same region was investigated by Browning et al. (1972)

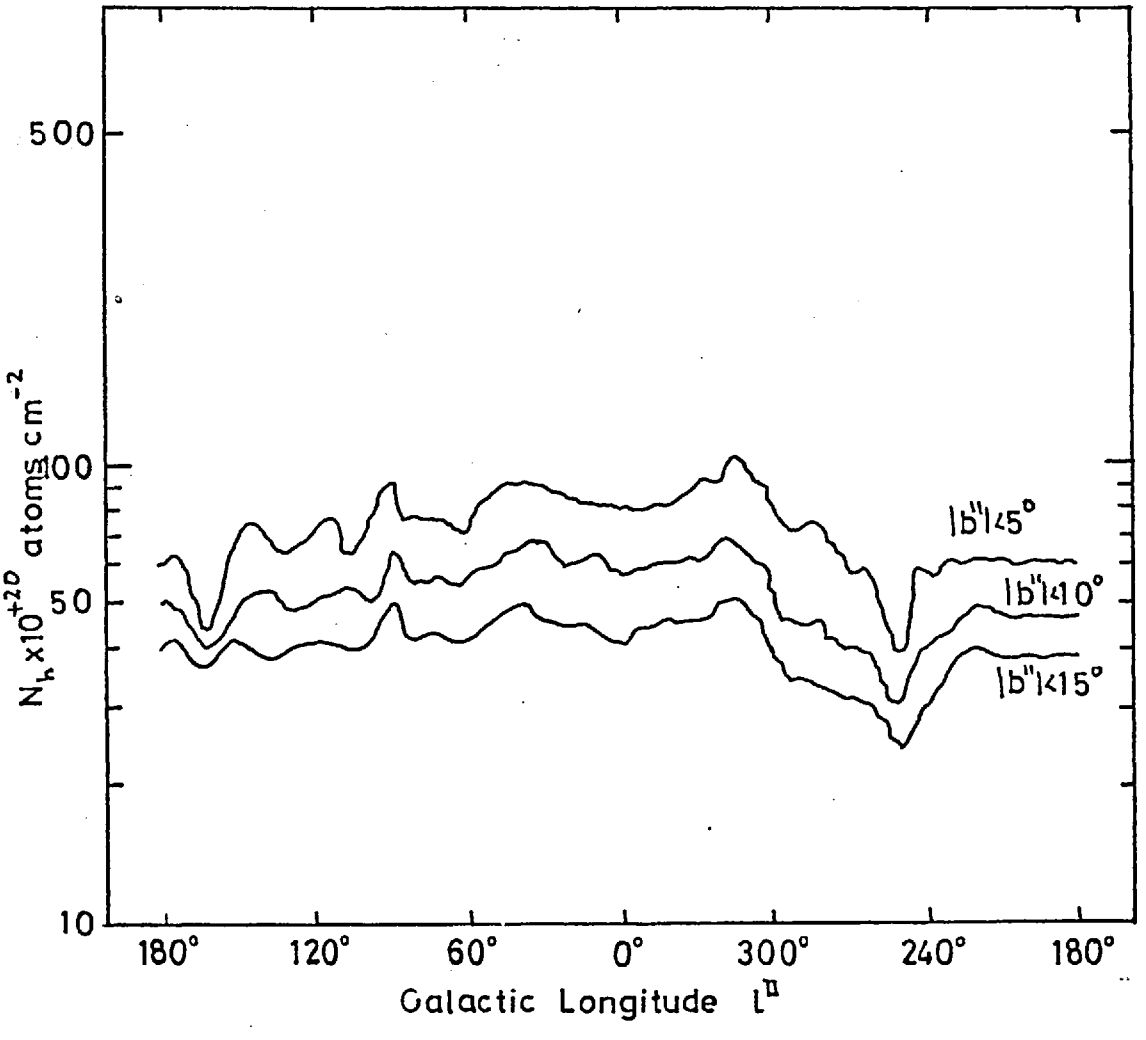


Figure 5.1 Line of sight density (<HL>) of neutral hydrogen in the galaxy, averaged over the latitude bands shown (after Clark, 1970).

at about the same time using a more sensitive balloon borne spark chamber detector. Although point emission was detected, the point sources reported by Niel et al. were not confirmed, neither was the line intensity of Clark et al. O'Mongain (1973) has pointed out that the point source identification claimed by both groups is suspect from statistical arguments.

In the galactic centre region, the gamma-ray emission has proved difficult to interpret. There is no obvious reason why the gamma-ray emissivity from this region should be greater than the rest of the disc if it results from p-p interactions between cosmic-rays and the neutral hydrogen observed from 21 cm radio emission. Figure 5.2a shows the distribution of neutral hydrogen in the galaxy, which may be compared with Figure 5.2b indicating the distribution of matter in the galaxy (in condensed form). Although there exists a bulge at the galactic centre in the distribution of stellar matter, no similar bulge is seen in the H I. Daltabuit and Meyer (1972) have reviewed the existing independent measurements of the H I and their findings agree with Figures 5.1 and 5.2a.

Alternative production mechanisms proposed to account for the gamma-ray emissivity have, in general, not stood the test of time. Ögelman's (1969) proposal that the flux arose from the integrated intensities of point sources has been discounted. Sources of sufficient intensity to account for the observed emission would have been resolvable by the gamma-ray detectors of Fichtel et al. and Frye et al. Although Frye et al. (1971) have tentatively identified 3 gamma-ray sources (3σ peaks in the combined sky plots of several balloon flights), the two which are within $\pm 15^{\circ}$ galactic latitude would, if unresolved, be too weak to account for the observed line intensity The source identifications have not been confirmed

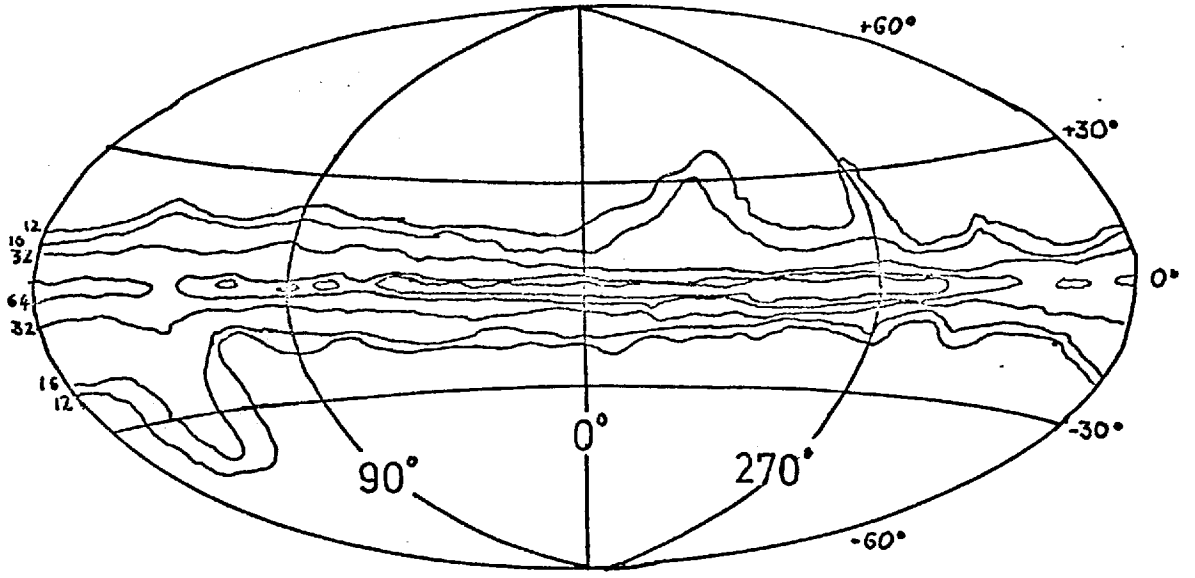


Figure 5.2a The distribution of neutral hydrogen in the galaxy. Contours of N_H x 10^{-20} cm^{-2}, N_H = 100 unlabelled (after Shklovski and Sheffer, 1971).

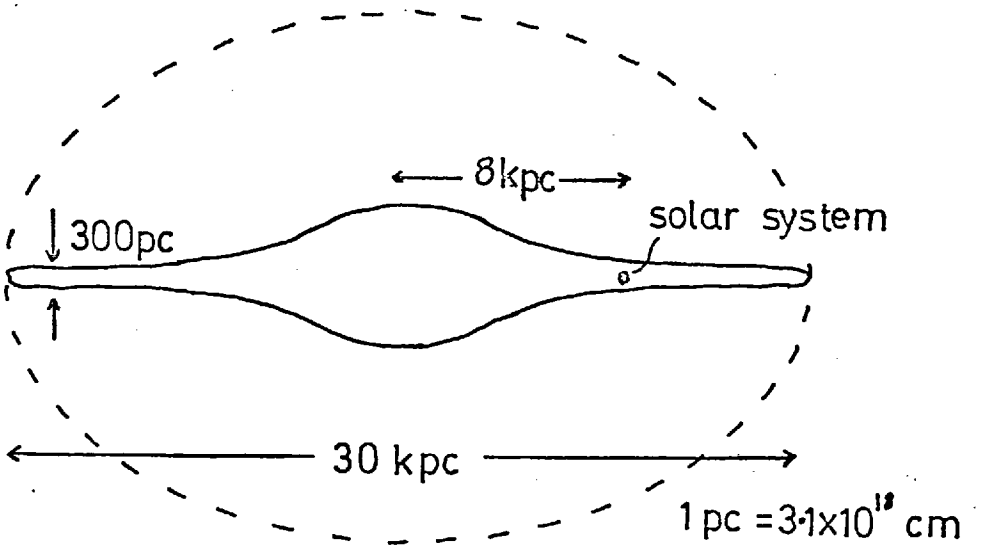


Figure 5.2b Schematic representation of our galaxy (dotted lines showing the extent of the proposed halo).

by independent groups, yet few detection systems flown to date have been able to match Frye's sensitivity.

Attempts were made to explain the observed intensity at the galactic centre with models proposing electromagnetic interactions between galactic electrons and the reported background photon intensity (black body temperature $8.3^{\circ}K$) observed by Shivanandan et al. (1968). Shen (1970) and O'Connell and Verma (1970) claimed that if the background radiation permeated the galaxy, the inverse Compton collisions with electrons would yield an anisotropy in the high energy galactic photon flux ranging from X-rays to gamma-ray energies. This hypothesis was supported by the observation of Cooke et al. (1969), who reported a line flux of 10 KeV X-rays in the galactic disc. The galactic emission was later investigated by the same group using detectors of better resolution and it was found that 90% of the observed anisotropy was attributable to X-ray point sources (Cooke and Pounds 1971). The present detection sensitivities limit the anisotropy of the X-ray diffuse background radiation to less than 10%. The anisotropy expected if the signal measured by Clark et al. resulted entirely from inverse Compton interactions would be ~30%, assuming no absorption.

The existence of the proposed $8.3^{\circ}K$ background intensity was put in doubt from various considerations. The energy density of the reported radiation points to a grave inbalance in the energy partition in the galaxy, since it represents 13 eV cm^{-3} compared with the starlight, $3^{\circ}K$ background, magnetic energy and cosmic-ray energy densities which are each less than or approximately equal to 1 eV cm^{-3}. Furthermore, serious problems are posed concerning its effect upon the lifetime of cosmic ray electrons (Harar et al., 1971) and high energy cosmic rays (Encrenaz and Partridge, 1969). It is

therefore likely that this radiation is a local effect.

Stecher and Stecker (1970) considered that a contribution to the gamma-ray flux may arise from inverse Compton interactions between cosmic-ray electrons and infra-red radiation concentrated in intense source regions, especially at the galactic centre. Helmken (1972) has examined the gamma-ray emission from the galactic centre, a region containing an extended infra-red source of the kind adopted in Stecher and Stecker's 2-component model. He observed a gamma-ray signal at the 2.6σ level of confidence which, Helmken claimed is consistent with Fichtel's line source mechanism, assuming a 2 component source model.

In Figure 5.3, the results of several workers have been plotted, together with the gamma-ray spectrum expected from π^0 decay and from inverse Compton interactions (in the second case the electron spectral exponent used is 2.6, which is that measured locally) ,normalised to 100 MeV.

The upper limit to the line intensity given by Share et al. (1972) at 10 MeV is crucial to the source mechanism argument. It is seen from Figure 5.3 that the π^0 decay spectrum is consistent with the upper limits of Share and lies within the 1σ error bar of the present result at 200 MeV. Furthermore, Fichtel et al. (1972) have compared the number of events in the 50-100 MeV interval with those >100 MeV and have concluded that the ratio is inconsistent with any other than the π^0 decay production mechanism.

The π^0 decay model does not preclude contributions from point sources, though these should necessarily produce gamma-rays by π^0 decay. Flaring of gamma-ray sources has been proposed by Frye et al. (1971) to explain why his results do not show evidence of the line emission which, incidentally, would also explain why

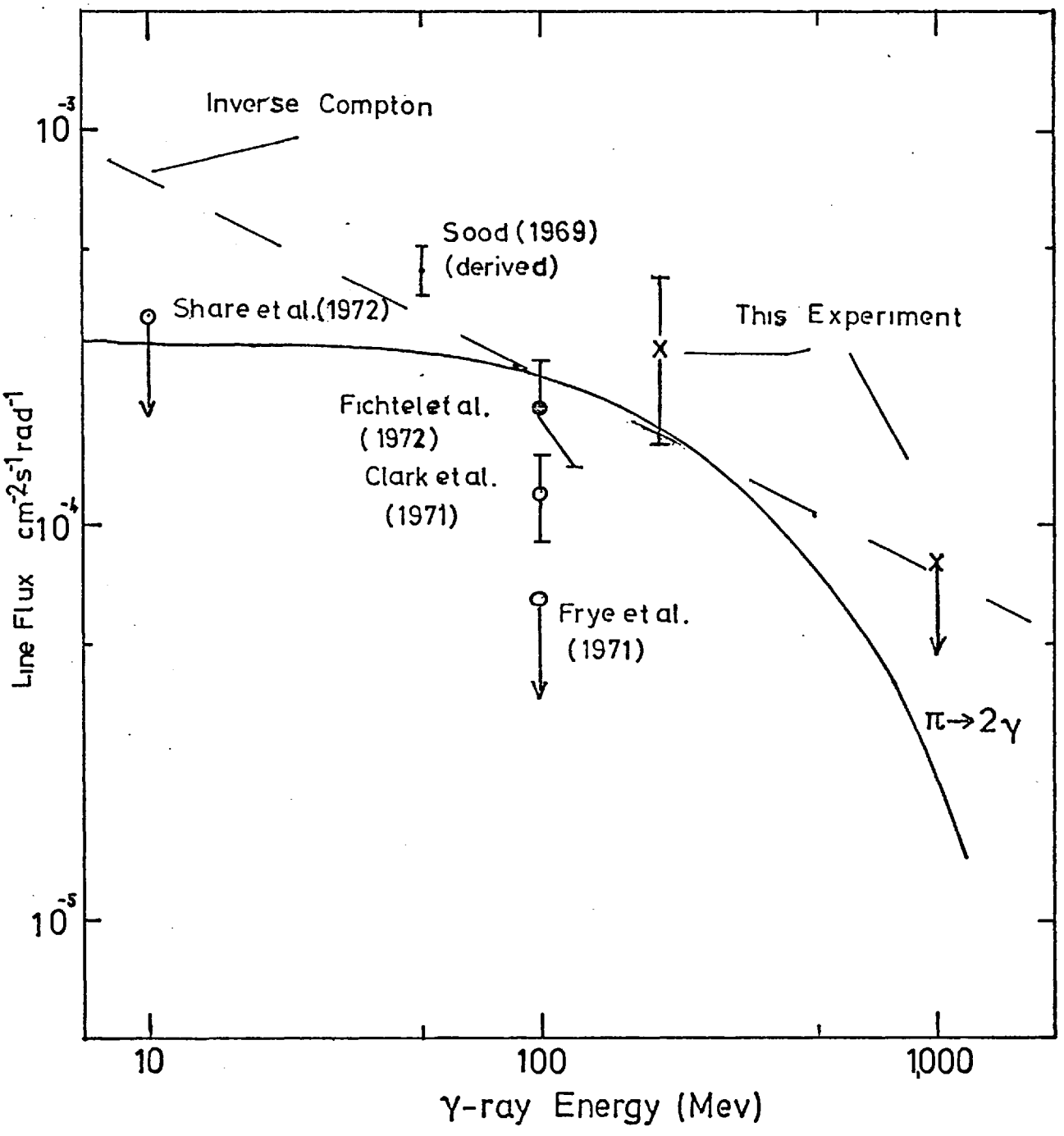


Figure 5.3 Recent measurements of the integral gamma-ray line intensity from the galactic centre region, and the pion decay, and inverse Compton spectrum.

no other workers have detected the reported sources. Frye pointed out that it is not uncommon to observe flaring of X-ray stars over periods ranging from minutes to days and has presented evidence (Frye et al., 1971a) that such gamma-ray flaring has been observed in a source designated Lib γ1. Volobuev et al. (1971) have reported gamma-ray flaring in the variable radio source 3C120, but since this has not been confirmed, it rather looks as though the result was spurious. (The calculated gamma-ray emissivity was $\sim 10^{47}$ ergs/sec —2 orders of magnitude greater than the average luminosity of a quasar.) Clark et al. have analysed their results for each half of the active period of the OSO 3 satellite experiment, which agreed to within 20%. Even so, the existence of time variations over shorter periods was not precluded.

If the calculated contribution to the gamma-ray line intensity from cosmic interactions with neutral hydrogen in the disc is subtracted from the average measured intensity at 100 MeV, there remains a flux of $\sim 1.5 \times 10^{-4}$ cm^{-2}sec^{-1}rad^{-1} to be accounted for. Levy and Goldsmith (1972) have produced a gamma-ray source function a factor of three more intense than that of Stecker (1970) and twice that of Cavallo and Gould (1971). They conclude that p-p reactions could produce the observed gamma-ray line flux with a target density of ~ 1 hydrogen atom cm^{-3}, the accepted value for neutral hydrogen in the disc, and a galactic cosmic ray intensity similar to the local value.

This production rate allows no contribution to the observed flux from other mechanisms, e.g., reactions involving unobserved gas, and the fluxes predicted in the region $30^{\circ} < l^{II} < 330^{\circ}$ put the observations of Clark et al. into question.

The findings of Levy and Goldsmith are heartily disputed

by Stecker (1972, 1973 and private communication). Stecker has calculated an upper limit to the gamma-ray production limit per hydrogen atom assuming the demodulated cosmic ray intensity of Comstock et al. (1972) and utilising new accelerator data of the p-p interaction for energies up to ~300 GeV. Although the spectral shape may be disputed, Stecker maintains that the total production rate cannot exceed $(1.5 \pm 0.23 \times 10^{-25})$ sec^{-1} per hydrogen atom. This is half Levy and Goldsmith's figure for 100 MeV gamma-rays and is consistent with the observed upper limit of 1.6×10^{-25} sec^{-1} set by Kraushaar et al. (1972). The results of Levy and Goldsmith should therefore be treated with some scepticism at this stage.

The galactic centre π^0 decay gamma-ray emission can be accounted for if either

(a) there are extensive regions of unobserved hydrogen in this part of the sky

(b) there is a gradient in the intensity of cosmic rays towards the galactic centre

or a combination of (a) and (b).

The 21 cm radio measurements of the H I distribution in the galaxy are not in dispute, but there exist at present no effective methods of detecting molecular hydrogen (other than from gamma-ray emission). Stecker (1969b) has considered in detail the possible existence of extensive regions of undetected hydrogen in the galaxy. Although there is an effective mechanism for its photodestruction in the interstellar radiation field, there remains the possibility that it may exist within dark clouds where the formation rate is larger than the destruction rate. This additional matter would not conflict with any requirements of galactic dynamics and would in fact help to explain the unaccountable distribution of stars

out of the disc which demands the stronger gravitational pull given by a larger amount of interstellar gas than observed.

The chemical composition of the cosmic ray flux implies that during their lifetime in the galaxy they traverse ~ 3.5 gm cm^{-2} of matter. Considered with the average gas density in the galaxy ($\sim 10^{-26}$ gm cm^{-3}) this figure indicates the lifetime of cosmic rays in the galaxy and the rate at which energy must be supplied to the cosmic rays to maintain the present flux. An increase in the interstellar hydrogen density by a factor of ~ 3 within a few hundred parsec of the galactic centre does not change these values substantially.

If the cosmic rays are of galactic origin then in particular regions of the galaxy, the cosmic ray flux may exhibit an isotropy. The recent results of Speller et al. (1972) place an upper limit to this anisotropy, if the net effect is a drift from the centre to the edge of the galaxy. Acceleration in Super Novae or Pulsars can satisfy the energy balance in the galaxy and are likely source candidates, but the present results do not preclude a gradient towards the galactic centre which would increase the intensity there by a factor of two. (Speller, private communication.)

It was unfortunate that the sensitivity of the present experiment was effectively reduced to only 25% of that hoped as a result of balloon failure and unanticipated high winds at altitude. However future aims are well defined, it being evident that balloon borne detectors must become more sensitive, e.g., by increasing the detection area and employing longer balloon flights at increased altitude. Investigation must continue at all gamma-

ray energies in order to provide the maximum spectral information from the observed radiation.

Although satellite experiments are inherently more sensitive than their balloon borne counterparts, their disadvantage is that experimental programmes are on a longer time scale and, generally are prohibitively expensive. By contrast, balloon detection techniques are easily adapted to follow up any theoretically predicted or observed phenomenon and are ideal for studying short time scale variations. Their rôle in the future of gamma-ray astronomy is therefore assured.

REFERENCES

Allkofer, O. C., 1969

'Spark Chambers' (Verlag Karl Thiemy Munchen).

Anand, K. C., Daniel, R. R., Stephens, S. A., 1968

Canadian J. Phys., 46, S484.

Barnaby, C. F., Barton, J. C., 1960

Proc. Phys. Soc., 76, 750.

Bethe, H. A., Ashkin, J., 1953

'Experimental Nuclear Physics', Vol. 1 (Publ. Wiley).

Beuermann, K. P., 1971

J. G. R., 76, 4291.

Boldt, E., 1969

'Lectures in High Energy Astrophysics', NASA Sp 199.

Bradamente, F., Sauli, F., 1967

Nucl. Inst. Meth., 56, 268.

Browning, R., Ramsden, D., Wright, P. J., 1972

Nature P. S., 235, 128.

Cavallò, G., Gould, R. J., 1971

Il Nuovo Cemento, 2B, 77.

Clark, G. W., 1971

'New Techniques in Space Astronomy', 3-13, (Publ. D. Reidel).

Clark, G. W., Garmire, G. P., Kraushaar, W. L., 1968

Ap. J., 153, L203.

Clark, G. W., Garmire, G. P., Kraushaar, W. L., 1970

'Non Solar X- and Gamma-Ray Astronomy', (Publ. L. Gratton).

Clark, G. W., Garmire, G. P., Kraushaar, W. L., 1971

Proc. 12th Int. Conf. Cosmic Rays, Hobart, OG.29.

Claverie, A., Niel, M., Vedrenne, G., 1971

Nucl. Inst. and Meth., 97, 161.

Comstock, G. M., Hsieh, K. C., Simpson, J. A., 1972

Ap. J. 173, 691.

Cooke, B. A., Griffiths, R. E., Pounds, K. A., 1969

Nature, 224, 134.

Cooke, B. A., Pounds, K. A., 1971

Nature P. S., 144, 229.

Crispin, A., Hayman, P. J., 1964

Proc. Phys. Soc., 83, 1051.

Daltabuit, E., Meyer, S., 1972

Astron. and Astrophys., 20, 415.

Encrenaz, P., Partidge, R. B., 1969

Geophysical Letters, 3, 161.

Eyles, C. J., Linney, A. D., Rochester, G. K., 1972

Plan. Space Sci., 20, 1915.

Fazio, G. G., 1967

Ann. Rev. of Astron. and Astrophys., 5, 481.

Fazio, G. G., 1970

Nature, 225, 905.

Fazio, G. G., Helmken, H. F., Cavrak, S. J., Hearn, D. R., 1968

Canadian J. Phys., 46, S427.

Felton, J. E., Morrison, P., 1963

Phys. Rev. Lett., 10, 453.

Felton, J. E., Morrison, P., 1966

Ap. J., 146, 686.

Fichtel, C. E., Kniffen, D. A., Ogelmann, H. B., 1969

Ap. J., 158, 193.

Fichtel, C. E., Hartman, R. C., Kniffen, D. A., Sommer, M., 1972

Ap. J., 171, 31.

Frye, G. M., Albats, P. A., Zych, A. D., Staib, J. A., Hopper, V. D., Rawlinson, W. R., Thomas, J. A., 1971
Nature, 231, 372.

Frye, G. M., Albats, P. A., Zych, A. D., Staib, J. A. Hopper, V. D., Rawlinson, W. R., Thomas, J. A., 1971 (a)
Proc. 12th Int. Conf. Cosmic Rays, Hobart.

Frye, G. M., Smith, J. A., 1966
Phys. Rev. Lett., 17, 733.

Frye, G. M., Staib, J. A., Zych, A. D., Hopper, V. D., Rawlinson, W. R., Thomas, J. A., 1969
Nature, 223, 1320.

Garmire, G. P., Kraushaar, W. L., 1965
Space Sci. Rev., 4, 123.

Ginzburg, V. L., 1972
Nature P. S., 239, 8.

Ginzburg, V. L., Syrovałskii, S. I., 1964
'The Origin of Cosmic Rays', (Publ. Pergamon).

Gould, R. J., 1965
Phys. Rev. Lett., 12, 511.

Gould, R. J., Burb idge, G. R., 1967
Handbuch der Physik, 46-2, 265.

Gould, R. J., Schréder, G., 1967 a
Phys. Rev., 155, 1404.

Gould, R. J., Schréder, G., 1967 b
Phys. Rev., 155, 1408.

Hadley, J., York, H., 1950
Phys. Rev., 80, 345.

Hanson, A. O., Lanzl, L. H., Lyman, E. M., Scott, M. B., 1951
Phys. Rev., 84, 634.

Helmken, H. F., 1972

Proc. IAU. Symp. No. 55, Madrid.

Hearn, D. R., 1969

Nucl. Inst. Meth., 70, 200.

Heristchi, D. J., 1967

Nucl. Inst. Meth., 47, 39.

Hutchinson, G. W., Pearce, A. J., Ramsden, D., Wills, R. D., 1970

Acta Phys. Hung., 29, suppl. 1, 87.

Janossy, L., 1948

'Cosmic Rays', (Publ. Clarendon Press).

Kniffen, D. A., 1971

'Cosmic Gamma-Rays', NASA Sp 249.

Kniffen, D. A., Fichtel, C. E., 1970

Ap. J., 161, L157.

Konig, P. J., Maree, J. P., Stoker, P. H., van der Walt, A. J., 1970

J.G.R., 75, 1172.

Kraushaar, W. L., Clark, G. W., Garmire, G. P., Voiken, R.,

Higbie, P., Leong, C., Thorsos, T., 1972

Ap. J., 177, 341.

Levy, D. J., Goldsmith, D. W., 1972

Ap. J., 177, 643.

Malin, S. R. C., 1969

Report to I.A.G.A., Madrid.

Marar, T. M. K., Freier, P. S., Waddington, C. J., 1971

J.G.R., 74, 1625.

Messel, H., Crawford, D. F., 1970

'Electron Photon Shower Distribution Function'

(Publ. Pergamon).

Morrison, P., 1958

Il Nuovo Cimento, 7, 858.

Niel, M., Vedrenne, G., Bouigue, R., 1972

Ap. J., 171, 529.

O'Connell, R. F., Verma, S. D., 1970

Acta Phys. Hung., 29, Suppl. 1, 255.

Ogelman, H., 1969

Nature, 221, 753.

Olsen, H., 1963

Phys. Rev., 131, 406.

O'Mongain, E., 1973

Nature, 241, 376.

Oort, J. H., Kerr, F. T., Westerhout, G., 1958

Monthly Notices R.A.S., 118, 379.

Ormes, J. F., Webber, W. R., 1966

Proc. Int. Conf. Cosmic Rays, London, 1, 349.

Perez-Mendez, V., Pfab, J. M., 1965

Nucl. Inst. Meth., 33, 141.

Perola, G. C., Scarsi, L., 1966

Il Nuovo Cimento, 46a, 718.

Peterson, L. E., Jacobson, A. S., Pelling, R. M., Schwartz, D. A., 1968

Canadian J. Phys., 46, S437.

Pollack, J. B., Fazio, G. G., 1963

Phys. Rev., 131, 2684.

Rossi, B., 1952

'High Energy Particles', (Publ. Prentice Hall).

Rossi, B., Greisen, K., 1941

Rev. Mod. Phys., 13, 223.

Sanderson, T. R., 1972

Nucl. Inst. Meth., 105, 371.

Share, G. A., Kinzer, H. L., Seeman, N., 1972

Proc. I.A.U. Symp., No.55, Madrid.

Shea, M. A., Smart, D. F., 1967

J.G.R., 72, 2021.

Shen, C. S., 1970

Acta Phys. Hung., 29, Suppl. 1, 267.

Shivanandan, K., Houck, J. P., Harwit, M. O., 1968

Phys. Rev. Lett., 21, 1460.

Shklovski, I. S., Sheffer, E. K., 1971

Nature, 231, 173.

Snyder, H. S., Scott, W. T., 1949

Phys. Rev., 76, 220.

Sood, R. K., 1969

PhD. Thesis, University of London .

Sood, R. K., 1969a

Nature, 222, 650.

Speller, R., Thambyahpillai, T., Elliot, H., 1972

Nature, 235, 25.

Stecher, T. P., Stecker, F. W., 1970

Nature, 226, 1234.

Stecker, F. W., 1969a

Astrophys. Sp. Sci., 3, 579.

Stecker, F. W., 1969b

Nature, 222, 865.

Stecker, F. W., 1970

Astrophys. Sp. Sci., 6,377.

Stecker, F. W., 1971

'Cosmic Gamma-Rays', NASA, SP - 249.

Stecker, F. W., 1972

G.S.F.C. preprint X - 641 - 72 - 462.

Stecker, F. W., 1973

NASA preprint, X - 641 - 73 - 40.

Valdez, J. P., Freier, P. S., Waddington, C. J., 1970

Acta Phys. Hung., 29, Suppl. 1, 79.

Volobuev, S. A., Galper, A. M., Kirillov-Ugryumov, V. G.,

Luchkov, B. I., Ozerov, Yu. V., 1971

J.E.T.P. Lett., 13, (1), 28.

Webber, W. R., 1967

Handbuch der Physik.,46/2, 181.

Weekes, T. C., Fazio, G. G., Helmken, H. F., O'Mongain, E.,

Rieke, G. H., 1972

Ap. J., 174, 165.

Zrelov, V. P., 1970

'Cerenkov Radiation in High Energy Physics',

(Publ. A.E.C. 7099).